APPLICATIONS OF SPIN GLASSES ACROSS DISCIPLINES: FROM COMPLEX SYSTEMS TO QUANTUM COMPUTING AND ALGORITHM DEVELOPMENT

A Dissertation

by

ZHENG ZHU

Submitted to the Office of Graduate and Professional Studies of
Texas A&M University
in partial fulfillment of the requirements for the degree of

DOCTOR OF PHILOSOPHY

Chair of Committee,	Helmut G. Katzgraber
Committee Members,	Stephen A. Fulling
	Wolfgang Bangerth
	Winfried Teizer
Head of Department,	George R. Welch

August 2015

Major Subject: Physics

ABSTRACT

The main subjects of this dissertation are spin glass applications in other disciplines and spin glass algorithms. Spin glasses are magnetic systems with disorder and frustration, and the essential physics of spin glasses lies not in the details of their microscopic interactions but rather in the competition between quenched ferromagnetic and antiferromagnetic interactions. Concepts that arose in the study of spin glasses have led to applications in areas as diverse as computer science, biology, and finance, as well as a variety of others.

In the first part of this dissertation I study the equilibrium and non-equilibrium properties of Boolean decision problems with competing interactions on scale-free networks in an external bias (a magnetic field). First, I perform finite-temperature Monte Carlo simulations in a field to test the robustness of the spin-glass phase and I show that the system has a spin-glass phase in a field, i.e., it exhibits a de Almeida–Thouless line. Then I study avalanche distributions when the system is driven by a field at zero temperature to test whether the system displays self-organized criticality. The numerical results suggest that avalanches (damage) can spread across the entire system with nonzero probability when the decay exponent of the interaction degree is less than or equal to 2, i.e., that Boolean decision problems on scale-free networks with competing interactions can be fragile when the system is not in thermal equilibrium.

In the second part of this dissertation I discuss the best-case performance of quantum annealers on native spin-glass benchmarks, i.e., how chaos can affect success probabilities. We perform classical parallel-tempering Monte Carlo simulations of the archetypal benchmark problem, an Ising spin glass, on the native chip topology.

Using realistic uncorrelated noise models for the D-Wave Two quantum annealer, I study the best-case resilience, or the probability that the ground-state configuration is not affected by random fields and random-bond fluctuations found on the chip. We compute the upper-bound success probabilities for different instance classes based on these simple error models, and I present strategies for developing robust and hard benchmark instances.

In the third part of this dissertation I present a cluster algorithm for Ising spin glasses that works in any space dimension and speeds up thermalization by several orders of magnitude at temperatures where thermalization is typically difficult. Our isoenergetic cluster moves are based on the Houdayer cluster algorithm for two-dimensional spin glasses and lead to a speedup over conventional state-of-the-art methods that increases with the system size. We illustrate the benefits (improved thermalization and achievement of more equiprobable sampling of ground states) of the isoenergetic cluster moves in two and three space dimensions, as well as in the nonplanar Chimera topology found in the D-Wave quantum annealing machine.

Finally, I study the thermodynamic properties of the two-dimensional Edwards-Anderson Ising spin-glass model on a square lattice using the tensor renormalization group method based on a higher-order singular-value decomposition. Our estimates of the partition function without a high precision data type lead to negative values at very low temperatures, thus illustrating that the method can not be applied to frustrated magnetic systems.

To my parents

ACKNOWLEDGEMENTS

First and foremost I would like to thank my advisor, Dr. Helmut G. Katzgraber. It has been an honor to be his first Ph.D. student at Texas A&M University. He has taught me how to effectively communicate with other scientists and how to be efficient. I appreciate all of the time, ideas, and funding that he contributed to make my Ph.D. experience productive and meaningful. His enthusiasm for his research, for teaching, and for making excellent presentations have been motivational for me, and his high standards regarding writing quality, presentation skills, and professionalism have helped me to become more than a scientist and to make this dissertation possible.

The members of the computational physics group at Texas A&M have contributed immensely to my personal and professional development. The group has been a source of friendships as well as good advice and collaboration. I am especially grateful for Andrew Ochoa's endless help with the English language and for his hospitality, which made office life more enjoyable and relaxed. It was Juan Carlos Andresen's inspiring idea that allowed me to participate in the discovery of interesting science for the first time in my life. Ruben Andrist's excellent programming skills set a strong example, showing me that I should study programming languages and become an efficient programmer. Visiting scholar Stefan Schnabel and postdoctoral researcher Oliver Melchert's low-profile philosophy of life as a physicist earned my admiration.

It was a pleasure to meet the great professors, staff, and graduate students at Texas A&M. Thanks to Dr. Stephen A. Fulling, Dr. Wolfgang Bangerth, and Dr. Winfried Teizer for serving as my committee members. Their time and effort were important for my Ph.D. research, not only in reviewing my dissertation, but also

by providing guidance and support for this work. I would like to thank Dr. Siu Chin and Chen Sun for their helpful discussions and suggestions concerning tensor network research. I would also like to thank graduate advisor Dr. Joseph Ross, Jill Lyster, Sandi Smith, and Sherree Kessler for their help with my course and degree plans.

Finally, I am truly and deeply indebted to my wonderful parents for their love, support, and encouragement throughout my entire life, and I am also very grateful to my friends Qi Zhang and Jinghui Wang.

TABLE OF CONTENTS

Page

ABSTRACT ii

DEDICATION iv

ACKNOWLEDGEMENTS v

TABLE OF CONTENTS vii

LIST OF FIGURES x

LIST OF TABLES xix

1. PHASE TRANSITIONS, CRITICAL PHENOMENA, SPIN GLASSES . . 1

    1.1 Phase transitions 1
    1.2 Critical phenomena 5
    1.3 Spin glass 9
        1.3.1 Phase transitions in spin glasses 10
        1.3.2 Long-range and short-range spin glass model 13
        1.3.3 Applications of spin glasses 15

2. NUMERICAL METHODS FOR SPIN GLASSES 16

    2.1 Metropolis algorithm 17
    2.2 Parallel tempering 19
    2.3 Houdayer cluster algorithm 20
    2.4 Test for equilibration 22
    2.5 Finite size scaling for spin glasses 23
    2.6 Optimization algorithms 26

3. BOOLEAN DECISION PROBLEMS WITH COMPETING INTERACTIONS ON SCALE-FREE NETWORKS: EQUILIBRIUM AND NONEQUILIBRIUM BEHAVIOR IN AN EXTERNAL BIAS 30

    3.1 Model 32
    3.2 Equilibrium properties in a field 33
        3.2.1 Observables 34

3.2.2 Equilibration scheme and simulation parameters 36
3.2.3 Numerical results for $\lambda = 4.50$ 39
3.2.4 Numerical results for $\lambda = 3.75$ 40
3.3 Nonequilibrium properties in a field 45
3.3.1 Numerical details and measured observables 46
3.3.2 Numerical results for Gaussian disorder 48
3.3.3 Numerical results for bimodal disorder 51
3.4 Summary and conclusions 54

4. BEST-CASE PERFORMANCE OF QUANTUM ANNEALERS ON NATIVE SPIN-GLASS BENCHMARKS: HOW CHAOS CAN AFFECT SUCCESS PROBABILITIES 57

4.1 Model, observables and algorithm 60
4.1.1 Model 60
4.1.2 Instance classes and observables 62
4.1.3 Algorithm details 64
4.2 Results 66
4.2.1 Yield of non-degenerate ground states 66
4.2.2 Resilience to noise 67
4.2.3 Effects of the number of first excited states 69
4.3 Conclusions 71

5. EFFICIENT CLUSTER ALGORITHM FOR SPIN GLASSES IN ANY SPACE DIMENSION 74

5.1 Benchmark model and observables 76
5.1.1 Reminder: Houdayer cluster algorithm 77
5.1.2 Isoenergetic cluster algorithm 79
5.2 Benchmarking results 83
5.3 Summary 87

6. EFFICIENT SAMPLING OF GROUND STATE CONFIGURATIONS FOR QUASI TWO-DIMENSIONAL ISING SPIN GLASSES 89

6.1 Model, algorithm and observables 90
6.2 Numerical results 92
6.3 Conclusions 97

7. LIMITATIONS OF APPLYING TENSOR RENORMALIZATION GROUP METHODS TO GLASSY SYSTEMS 99

7.1 Model 100
7.2 Algorithm 101

7.3 Numerical results 102
7.3.1 Exact method 102
7.3.2 HOTRG 104
7.4 Conclusions 107

8. SUMMARY AND OUTLOOK 108

REFERENCES 112

APPENDIX A. ANALYTICAL FORM OF THE DE ALMEIDA-THOULESS FOR $H_R \to 0$ 133

LIST OF FIGURES

FIGURE Page

1.1 Sketch of phase diagram for water molecules, the blue curve represents the transition between liquid (water) and solid (ice) states, the red curve represents the transition between gas (vapor) and liquid (water) states, the purple curve represents the transition between solid (ice) and gas (vapor) states. 3

1.2 Magnetization as a function of temperature for the 2D Ising model. At zero temperature, the state stays completely ordered. As we increase temperature, the magnetization starts to drop rapidly until the phase transition occurs. Above the critical temperature $T_c = 2.269$, the absolute magnetisation is nearly zero. 3

1.3 Disorder and frustration in a spin glass. Bonds marked "+" correspond to ferromagnetic couplings, "-" corresponds to an antiferromagnetic coupling. For a ferromagnet the energy is minimized by aligning all spins, in the case of spin glass, no spin configuration can simultaneously satisfy all couplings. 10

1.4 Sketch of phase diagram for three-dimensional Ising spin glass with bimodal disorder. The blue curve represents the transition between ferromagnetic (FM) and paramagnetic states (PM), the purple curve represents the transition between spin glass (SG) and ferromagnetic states (FM), the red curve represents the transition between spin glass (SG) and paramagnetic states (PM). T and p are temperature and fraction of antiferromagnetic bonds, respectively. 11

1.5 Sketch of Almeida–Thouless (AT) line for the SK model. The AT line separates a spin glass phase with divergent relaxation times and "replica symmetry breaking" from a paramagnetic "replica symmetric" phase with finite relaxation times. 15

2.1 Sketch of a rough energy landscape of spin glass. A Monte Carlo move is unlikely if the height of the energy barrier ΔE is large, especially at low temperatures. In this case, a simple Monte Carlo simulation will stall and the system will be stuck in the metastable state. 18

2.2 This figure shows energy per spin e as a function of Monte Carlo time (measured in lattice sweeps) $t = 2^b$ with (blue dots) and without (red dots) parallel tempering (system size $N = 64$, temperature $T = 0.21$) for a 2D square lattice. The system is in equilibrium when e becomes approximately flat and fluctuates around a mean value. The data show that without parallel tempering (PT), the system does not reach equilibrium even after 2^{20} MCS. In contrast, the system thermalizes much faster with parallel tempering and reaches equilibrium after only a few thousand Monte Carlo sweeps. 20

2.3 This figure shows energy per spin e as a function of Monte Carlo time (measured in lattice sweeps) $t = 2^b$ with (blue dots) and without (red dots) Houdayer cluster moves (system size $N = 64$, temperature $T = 0.02$) for a 2D square lattice. The system is in equilibrium when e becomes approximately flat and fluctuates around a mean value. The data show that without Houdayer cluster moves (HC), the system does not reach equilibrium even after 2^{20} MCS. However, it thermalizes much faster with Houdayer cluster moves and reaches equilibrium after only a few thousand Monte Carlo sweeps. Note temperatures for the simulations here are extremely low (about 1/10 of temperatures in figure 2.2), the simple Monte Carlo method will be useless. 22

2.4 Equilibration test for a 2D square lattice with $N = 64$ spins at $T = 0.212$. Once the data for the energy e and the energy $e(q_l)$ computed from link overlap q_l agree, the system is in thermal equilibrium (shaded area). 24

2.5 Sketch of Binder ratio $g(T)$ for the Sherrington-Kirkpatrick model with different system sizes N as a function of temperature T. The data cross at a point (shaded area) and we obtain the critical temperature T_c. 25

2.6 Sketch of finite-size scaling analysis of Binder ratio $g(T)$ for the Sherrington-Kirkpatrick model with different system sizes N as a function of $N^{1/\nu}(T - T_c)$. Close to the transition the data fall onto a universal curve, showing that ν is the correct value of the critical exponent. . 26

2.7 This figure [65] illustrates the relationships among the three categories: P, NP, and NP-complete. The existence of problems within NP but outside both P and NP-complete, under assumption P $\neq$ NP, was established by Ladner's theorem [66]. For spin glasses, non-planar model and the planar model with an external field are NP-complete, planar model is P, it is unclear whether there are spin glass problems that are in the complexity class NP but are neither in the class P nor NP-complete. 29

3.1 Equilibration test for $N = 8192$ spins at $T = 1.500$ (lowest temperature simulated) and $\lambda = 3.75$. Once the data for the energy U and the energy computed from q_4 $[U(q_4)]$ agree, the system is in thermal equilibrium (shaded area). At this point data for q^2 are also independent of Monte Carlo time. Note that the data for q^2 are shifted by a constant factor of 1.1 for better comparison. Error bars are smaller than the symbols. 37

3.2 Extrapolation to the thermodynamic limit for the critical temperature T_c for $\lambda = 4.50$ and $H_r = 0.1$. We determine the crossing points of critical temperatures of the susceptibility expression for pairs of system sizes N and $2N$. Using Eq. (3.14) with $\omega = 1$ we extrapolate the data to the thermodynamic limit. This allows us to take into account corrections to scaling in an unbiased way. 41

3.3 Field H_r versus temperature T phase diagram for an Ising spin glass on a scale-free graph with $\lambda = 4.50$. The data points separate a paramagnetic (PM) from a spin-glass (SG) state. The shaded area is intended as a guide to the eye. The dotted (blue) line is a calculation of the AT line in the $H_r \to 0$ limit. 42

3.4 Finite-size scaling analysis of $\chi/N^{2-\eta}$ as a function of $N^{1/\nu}(\beta - \beta_c)$ for an Ising spin glass on a scale-free network with Gaussian disorder and $\lambda = 3.75$. The data at zero field (top panel) scale very well. The bottom panel shows representative data for $H_r = 0.1$ scaled according to Eq. (3.7). Error bars are smaller than the symbols. 44

3.5 Field H_r versus temperature T phase diagram for an Ising spin glass on a scale-free graph with $\lambda = 3.75$. The data points separate a paramagnetic (PM) from a spin-glass (SG) state. The shaded area is intended as a guide to the eye. The dotted (blue) line is a calculation of the AT line in the $H_r \to 0$ limit. Note that estimates for the critical temperature T_c from a finite-size scaling analysis (FSS) according to Eq. (3.7) with T_c, η, and ν as free parameters agree within error bars with estimates at finite fields where $\eta = 19/11$ and $\nu = 11/3$ are used as fixed parameters (labeled with "Fixed" in the plot). 45

3.6 Top: Avalanche distribution $D(n)$ for the Edwards-Anderson spin-glass model with Gaussian disorder on scale-free networks with $\lambda = 4.50$ recorded across the whole hysteresis loop. The data show no system size dependence. The vertical (black) line marks the extrapolated value of n^*. Clearly, no signs of SOC are visible in the data. Bottom: Magnetization $M = (1/N)\sum_i s_i$ versus field H hysteresis loop for $\lambda = 4.50$ and 48000 spins. The data are for one single sample and meant as an illustration for the typical behavior of the system in a field. The inset shows a zoom into the boxed region. The discrete steps due to magnetization jumps in the hysteresis loop are clearly visible. 49

3.7 Top: Avalanche distribution $D(n)$ for the Edwards-Anderson spin-glass model with Gaussian disorder on scale-free networks with $\lambda = 1.5$ recorded across the whole hysteresis loop. For $\lambda = 1.5 < 2.0$ the number of neighbors diverges. The data show a clear system-size dependence with the distributions becoming increasingly power-law-like for increasing system size N. As shown in Fig. 3.8, the extrapolated cutoff value is $n^* = \infty$, i.e., the system exhibits true SOC behavior. Bottom: Magnetization $M = (1/N)\sum_i s_i$ versus field H hysteresis loop for $\lambda = 1.50$ and 48000 spins. The data are for one single sample and meant as an illustration for the typical behavior of the system in a field. The inset shows a zoom into the boxed region. The discrete steps due to magnetization jumps in the hysteresis loop are clearly visible. Qualitatively, the data seem to show larger rearrangements as for $\lambda = 4.50$ (Fig. 3.6). 50

3.8 Characteristic avalanche size n^* extrapolated to the thermodynamic limit for different values of λ and Gaussian disorder. Plotted are $1/n^*$ versus λ. Only when $1/n^* = 0$ (here within error bars) we can expect the system to show SOC behavior. This is only the case for $\lambda \leq 2$, i.e., in the regime where the number of neighbors diverges. 51

3.9 Avalanche distribution $D(n)$ for the Edwards-Anderson spin-glass model with bimodal disorder on scale-free networks with $\lambda = 3.5$ recorded across the whole hysteresis loop. Top panel: Data for $p = 0.63 < p_c$. Here the system displays subcritical behavior, i.e., the characteristic avalanche size n^* is finite. Center panel: For $p = 0.66 \approx p_c$ the system is in the critical regime where the distributions are well described by power laws. Bottom panel: For $p = 0.70 > p_c$ the system is in the supercritical regime. A jump in the hysteresis loop occurs, i.e., very large rearrangements are very probable, as can be seen in the bump that develops in the distributions $D(n)$ for large n. 52

3.10 Fraction of ferromagnetic bonds p versus λ phase diagram for the Edwards-Anderson spin-glass model on scale free networks with bimodal interactions between the spins. For $\lambda > 2$ a critical line $p_c(\lambda)$ separates the subcritical regime where avalanches are small, from the supercritical regime where system-spanning avalanches are very common. Along the critical line $p_c(\lambda)$ (triangles, solid line) avalanche sizes are distributed according to power laws. For $\lambda \leq 2$ the number of neighbors diverges. In this regime for $p = 0.5$ the system displays avalanches that are power laws, i.e., true SOC. The dotted line represents the spin-glass–to–ferromagnetic phase boundary from Fig. 2 in Ref. [2]. 55

4.1 Adjacency matrix of the D-Wave Two chip with 8×8 $K_{4,4}$ cells and 512 qubits (circles) connected by couplers (lines). 61

4.2 Resilience ($\mathcal{R}$) of different instance classes (see text) for a $N = 512$ qubit system on the Chimera graph as a function of Gaussian random field strength (h). Instance classes are less resilient to noise with increasing field strength and decreasing classical energy gap. The shaded line represents the current field noise strength of approximately 5% in the D-Wave Two system. 68

4.3 Resilience ($\mathcal{R}$) of different instance classes (see text) for a $N = 512$ qubit system on the Chimera graph as a function Gaussian random bond fluctuation strength (ΔJ). Instance classes are less resilient to noise with increasing bond fluctuation strength and a decreasing classical energy gap. The shaded line represents the current bond noise strength in the D-Wave Two system, i.e., $\sim 3.5\%$. Note that bond noise has a stronger effect than field noise (Fig.4.2) on the device. 69

4.4 Resilience $\mathcal{R}$ of the $U_{5,6,7}$ instance class as a function of the bond fluctuation strength (ΔJ) for different system sizes N on the Chimera topology. The resilience clearly decreases for increasing noise and system size. The shaded vertical line represents the current bond-noise strength in the D-Wave Two system, approximately 3.5%. . . . 70

4.5 Resilience $\mathcal{R}$ as a function of the number of first excited states N_1 for $N = 512$ spins on the Chimera lattice. The data are for the $U_{5,6,7}$ instance class. The color bar shows approximately how often a given number of first excited states occurs for the 900 instances studied. In this case, between four and eight first excited states are most common. 71

5.1 Fraction of spins p of potential cluster members as a function of temperature T for different system sizes N in two space dimensions (2D). The horizontal line represents the percolation threshold of a two-dimensional square lattice, i.e., $p_c \approx 0.592$ [156]. Because $p \to 0.5$ for $T \to \infty$, for all T clusters do not percolate, which is why the HCA is efficient in two-dimensional planar geometries. Error bars are computed via a jackknife analysis over configurations and are smaller than the symbols. 80

5.2 Fraction of spins p as a function of temperature T for different system sizes N on the Chimera topology. The horizontal line represents the percolation threshold of the nonplanar Chimera topology, namely $p_c \approx 0.387$ computed here using the approach developed in Ref.[157]. For $T \gtrsim J = 1$ clusters percolate and cluster updates provide no gain. Error bars are computed via a jackknife analysis over configurations and are smaller than the symbols. 81

5.3 Fraction of spins p as a function of temperature T for different system sizes N in three space dimensions (3D). The horizontal line represents the percolation threshold of the three-dimensional cubic lattice ($p_c \approx 0.311$ [158]). For $T \gtrsim J = 1$ clusters percolate. Error bars are computed via a jackknife analysis over configurations and are smaller than the symbols. 82

5.4 Δ [Eq. (5.4)] as a function of simulation time $t = 2^b$ measured in Monte Carlo sweeps in two space dimensions (2D) for $N = 1024$ and $T = 0.212$. Simulations using vanilla PT thermalize at at least 2^{25} Monte Carlo sweeps, whereas with the addition of ICMs thermalization is reduced to approximately 2^{16} Monte Carlo sweeps. This means approximately two orders of magnitude improvement. Error bars are computed via a jackknife analysis over configurations. 84

5.5 Δ as a function of simulation time $t = 2^b$ measured in Monte Carlo sweeps for an Ising spin glass on Chimera with $N = 1152$ spins at $T = 0.212$. Simulations using PT thermalize at approximately 2^{25} Monte Carlo sweeps, whereas the addition of ICMs reduces thermalization to 2^{18} Monte Carlo sweeps. Again, approximately two orders of magnitude speedup. Error bars are computed via a jackknife analysis over configurations. 85

5.6 Δ as a function of simulation time $t = 2^b$ measured in Monte Carlo sweeps in three space dimensions (3D) for $N = 1728$ and $T = 0.42 \sim 0.43T_c$. Using standard PT, the system thermalizes approximately after 2^{23} Monte Carlo sweeps. This time is reduced to $\sim 2^{20}$ Monte Carlo sweeps when ICMs are added. Error bars are computed via a jackknife analysis over configurations. 86

5.7 Ratio between the *approximate* average thermalization time of PT and PT+ICM for different topologies at the lowest simulation temperature (see Tab. 5.1) as a function of system size N. In all cases the speedup increases with increasing system size. Note that thermalization times have been determined by eye. 87

6.1 Scatter plot of quantities $Q_{\text{num}}\sqrt{n}$ as a function of the ground state degeneracy $G-1$ for different spin glass samples with different system sizes N on a Chimera graph. The data points for ICA (blue color) are closer to the theoretical limit than those for the PT (red color), and this improvement gets better as the system size increases. 93

6.2 Median ratio $Q_{\text{num}}/Q_{\text{th}}$ over different spin glass samples as a function of the system size N on a Chimera graph. The data points show that ICA (blue color) is better than PT (red color) for all system sizes, and the general trend for both algorithms is that the ratio goes up as the system size increases, then it peaks at a certain point, and beyond a certain system size the ratio goes down as the system size continues to increase. Note there is no critical point and phase transition here. 94

6.3 Two examples of ground state configurations with different Hamming distances on a Chimera graph for system size $N = 512$. The Hamming distance denotes the difference between two binary strings (ground state configurations). Each dot in the figure represents a ground state, black lines are 1-bit differences, red lines are 2-bit differences, and anything that is a light color or blue is an even greater difference. In the example on the left, all ground state configurations are related by 1-bit differences, while the example on the right shows that Hamming distances between certain ground state configurations can be large—which means that it will take longer for the system to move from one ground state to another and this will cause larger fluctuations in the ground state frequency. 95

6.4 Scatter plot of quantities $Q_{\text{num}}\sqrt{n}$ as a function of the ground state degeneracy $G-1$ for different spin glass samples with different system sizes N on a 2D lattice. The data points for ICA (blue color) are closer to the theoretical limit than those for the PT (red color), and this improvement gets better as the system size increases. 96

6.5 Median ratio $Q_{\text{num}}/Q_{\text{th}}$ over different spin glass samples as a function of the system size N on a 2D lattice. The data points show that ICA (blue color) is better than PT (red color) for all system sizes, and the general trend for both algorithms is that the ratio goes up as the system size increases, then it peaks at a certain point, and beyond a certain system size the ratio goes down as the system size continues to increase. Note there is no critical point and phase transition here. 97

7.1 Failure rate P_f of the partition function for 2D Edwards-Anderson spin glass as a function of the temperature T. 960 samples with $L = 4$ and $p = 0.5$ were generated to calculate the failure rate and error bars. 102

7.2 Failure rate P_f of the partition function for 2D Edwards-Anderson spin glass as a function of the number of bits B. 960 samples with $L = 4$ and $p = 0.5$ at $T = 0.05$ were generated to calculate the failure rate and error bars. 104

7.3 Example plot for 256 tensor components of 2D Edwards-Anderson spin glass with $p = 0.5$, $L = 4$, and $T = 0.05$ and components of the ferromagnetic Ising model with $L = 4$ and $T = 0.05$. T_f is the tensor element value and I_f is the tensor element index of the final contracted tensor. 105

7.4 Failure rate P_f of the partition function for 2D Edwards-Anderson spin glass with HOTRG as a function of the temperature T and number of bits B. 480 samples with $L = 4, 8, 16$ and $p = 0.5$ were generated to calculate the failure rate and error bars. 106

LIST OF TABLES

TABLE Page

1.1 Different orders of phase transitions. First-order phase transitions are those that involve a latent heat. Second-order phase transitions are also called continuous phase transitions and characterized by a divergent susceptibility, an infinite correlation length, and a power-law decay of correlations near criticality. 5

3.1 Parameters of the simulation: For each exponent λ and system size N, we compute $N_{\rm sa}$ disorder or network instances. $N_{\rm sw} = 2^b$ is the total number of Monte Carlo sweeps for each of the $4N_T$ replicas for a single instance, $T_{\rm min}$ [$T_{\rm max}$] is the lowest [highest] temperature simulated, and N_T is the number of temperatures used in the parallel tempering method for each system size N. 38

3.2 Critical parameters T_c, ν, and η for a spin glass with Gaussian random bonds defined on a scale-free graph. The data for $\lambda = 4.50$ have been determined using the mean-field finite-size scaling expression in Eq. (3.9). In this case one can, in principle, define $\eta = 5/3$ and $\nu = 3$, although these should be viewed as parameters placed in Eq. (3.7) to obtain Eq. (3.9). For $\lambda = 3.75$ we determine the critical parameters using Eq. (3.7). The starred estimates of T_c for $H_r > 0$ have been determined by using the zero-field estimates of $\eta = 19/11$ and $\nu = 11/3$ as fixed. Both T_c and $T_c^\star$ agree within error bars, except statistical fluctuations are smaller for $T_c^\star$ because there are fewer fitting parameters. 43

3.3 Simulation parameters in the nonequilibrium study with both Gaussian and bimodal-distributed random bonds: For each exponent λ we study systems of $N = 500 \times 2^m$ spins with $m \in \{1, \ldots, m_{\rm max}\}$. For Gaussian disorder, when $\lambda < 4$, we also simulate systems with 48 000 spins ($m = 6$ corresponds to 32 000 spins). All distributions are computed using $N_{\rm sa}$ disorder realizations. 47

4.1 Simulation parameters: For each instance class and system size N, we compute N_{sa} instances. $N_{\mathrm{sw}} = 2^b$ is the total number of Monte Carlo sweeps for each of the $4N_T$ replicas for a single instance, T_{min} [T_{max}] is the lowest [highest] temperature simulated, and N_T is the number of temperatures used in the parallel tempering method. For the lowest N_{icm} temperatures isoenergetic cluster moves are applied. 66

5.1 Parameters of the simulation in two space dimensions (2D), three space dimensions (3D), and on the Chimera (Ch) topology. For each topology simulated and system sizes N, we compute N_{sa} disorder instances and measure over 2^b Monte Carlo sweeps (and isoenergetic cluster moves) for each of the $2N_T$ replicas. T_{min} [T_{max}] is the lowest [highest] temperature simulated, and N_T is the total number of temperatures used in the parallel tempering Monte Carlo method. Isoenergetic cluster moves only occur for the lowest N_{c} temperatures simulated (determined from figs. 5.1 to 5.3). 84

6.1 Parameters of the simulation: For each instance class and system size N, we compute N_{sa} instances. $N_{\mathrm{sw}} = 2^b$ is the total number of Monte Carlo sweeps for each of the $4N_T$ replicas for a single instance, T_{min} [T_{max}] is the lowest [highest] temperature simulated, and N_T and N_{hc} are the number of temperatures used in the parallel tempering method and in the isoenergetic cluster algorithm, respectively. 92

1. PHASE TRANSITIONS, CRITICAL PHENOMENA, SPIN GLASSES

The analysis of phase transitions and the associated microscopic structures is a well-developed scientific approach in physics. Mathematical and conceptual tools developed from spin glass phase transition have found their way into a variety of applications, including satisfiability problem [1], probability of finding an unsatisfiable instance shows a sharp threshold behavior at some critical ratio between the number of clauses and variables; the robustness of scale free network to local perturbation [2]; the finite-temperature phase space of quantum annealer [3]; percolation theory [4]; etc. In this chapter we provide an overview of phase transition, critical phenomena and spin glass physics.

1.1 Phase transitions

A *phase transition* is the transformation of a thermodynamic system from one phase to another. A phase is a state of matter in which the macroscopic physical properties of the substance are uniform on the macroscopic scale and usually characterized by a thermodynamic function, which is a function of macroscopic parameters such as temperature, pressure, etc. During a phase transition of a thermodynamic system, certain properties of the system change as a result of a change in some macroscopic parameters. For example, a liquid may become gas when heated to the boiling point, resulting in an abrupt change in volume, and a two-dimensional (2D) Ising model [5] may suddenly lose its spontaneous magnetization as its temperature exceeds the critical temperature. These properties of the system are actually measures of the degree of order across boundaries in the phase transition and are usually called *order parameters*. From a theoretical point of view, order parameters arise from symmetry breaking; for example, in the case of the 2D Ising model, the

magnetization M is spontaneously broken when the system is cooled to below the Curie temperature.

A phase diagram is a graphical representation of the physical states of matter under different conditions indicated by the macroscopic parameters. A typical phase diagram has macroscopic parameters on the x- and y-axes and several specific features, including phase boundaries, a critical point, and a triple point. A phase boundary separates different phases. A change in parameters across a phase boundary, such as a change in temperature, causes a sudden change in the phase of the substance. A phase boundary sometimes disappears at a critical point, where the two phases become indistinguishable and the substance shows anomalous behavior.

Figure 1.1 below shows a phase diagram for water molecules. Every point in this diagram represents a possible combination of temperature and pressure for the system. The diagram is divided into three areas, which represent the solid, liquid, and gas states of the water molecules.

Figure 1.2 shows a phase diagram for the 2D Ising model using Onsager's formula for spontaneous magnetization. There is a phase transition at the critical temperature $T_c = 2.269J/k$: the system stays mostly ordered below the critical temperature and the average magnetization M is one, while the system becomes completely unordered above T_c and the average magnetization M is zero.

In the conventional classification [6], phase transitions are divided into two broad categories by the degree of singularity in the physical quantities (see table 1.1). When the first-order derivative of the free energy (usually either Helmholtz free energy F or Gibbs free energy G) shows a discontinuity, the transition is first-order and typically involves latent heat. The transition is called *continuous* if the second- or a higher-order derivative of the free energy shows a discontinuity or divergence. Continuous phase transitions are usually characterized by a divergent susceptibility, an infinite

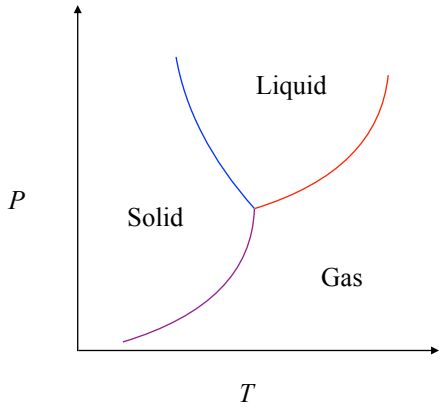

Figure 1.1: Sketch of phase diagram for water molecules, the blue curve represents the transition between liquid (water) and solid (ice) states, the red curve represents the transition between gas (vapor) and liquid (water) states, the purple curve represents the transition between solid (ice) and gas (vapor) states.

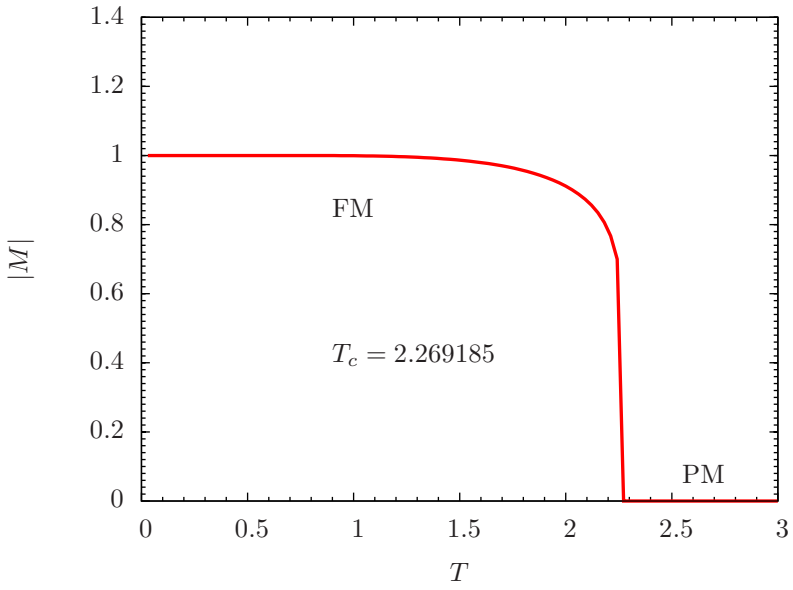

Figure 1.2: Magnetization as a function of temperature for the 2D Ising model. At zero temperature, the state stays completely ordered. As we increase temperature, the magnetization starts to drop rapidly until the phase transition occurs. Above the critical temperature $T_c = 2.269$, the absolute magnetisation is nearly zero.

correlation length, and a power-law decay of correlations near criticality. Examples of first-order phase transitions are the melting of ice and the boiling of water. The ice–water or water–vapor transition releases latent heat, which means that entropy

$$S = -\frac{\partial F}{\partial T} \tag{1.1}$$

is discontinuous. Alternatively, we can say that volume

$$V = \frac{\partial G}{\partial P} \tag{1.2}$$

is discontinuous. An example of a second-order phase transition is in the 2D Ising model, where the specific heat

$$C_v = T(\frac{\partial S}{\partial T})_v = -T(\frac{\partial^2 F}{\partial T^2})_v \tag{1.3}$$

and magnetic susceptibility

$$\chi = \frac{\partial m}{\partial H} = -\frac{\partial^2 F}{\partial H^2} \tag{1.4}$$

are divergent at the critical temperature.

In some limited cases, we can derive exact solutions for the phase transitions of a thermodynamic system—for instance, in the case of 1D and 2D Ising models [7, 5]. But in general, we have to resort to approximate methods to understand phase transitions. Mean field theory was introduced by Landau [8, 9] in an attempt to formulate a general theory of continuous phase transitions. Essentially, mean field theory neglects spin fluctuations around the mean and treats spins as behaving statistically independently. In the simplest version, when Weiss mean field theory predicts the existence of a phase transition for the 1D Ising model, it fails even

qualitatively. However, in higher dimensions, spin is coupled with more and more neighbors, whose fluctuations around the mean magnetization will increasingly tend to cancel one another. Thus, mean field theory gives the correct results for an Ising model with a high enough space dimension ($D = 4$ is the upper critical dimension).

Table 1.1: Different orders of phase transitions. First-order phase transitions are those that involve a latent heat. Second-order phase transitions are also called continuous phase transitions and characterized by a divergent susceptibility, an infinite correlation length, and a power-law decay of correlations near criticality.

	Differential of free energy G	Corresponding experimental quantities
First	S, V	S, V
Second	$(\frac{\partial S}{\partial T})_p, (\frac{\partial V}{\partial T})_p, (\frac{\partial S}{\partial p})_T, (\frac{\partial V}{\partial p})_T$	C_p, β, κ
Third	$(\frac{\partial^2 S}{\partial T^2})_p, (\frac{\partial^2 V}{\partial T^2})_p, \frac{\partial^2 S}{\partial T \partial p}$ $(\frac{\partial^2 S}{\partial p^2})_T, (\frac{\partial^2 V}{\partial p^2})_T, \frac{\partial^2 V}{\partial T \partial p}$	$(\frac{\partial C_p}{\partial T})_p, (\frac{\partial \beta}{\partial T})_p, (\frac{\partial \kappa}{\partial T})_p$ $(\frac{\partial C_p}{\partial p})_T, (\frac{\partial \beta}{\partial p})_T, (\frac{\partial \kappa}{\partial p})_T$

1.2 Critical phenomena

Critical phenomena [10] often refers to continuous phase transitions; it is the collective name associated with the physics of critical points. The critical behavior is usually different from the mean-field approximation that is valid away from the phase transition. This is because the mean-field approximation neglects correlations, which become increasingly important as the system approaches the critical point where the correlation length diverges. The three pillars of modern critical phenomena theory are scaling, universality, and renormalization [10].

The scaling hypothesis [11, 12] has two categories of predictions, both of which have been remarkably well verified by experimental data for diverse systems. The first category is a set of relations, called *scaling relations*, that serve to relate the various critical-point exponents, which describe the behavior of physical quantities

near continuous phase transitions. For example, the critical exponents of phase transitions in the Ising model, α, β, γ, and ν, describe the behavior of the specific heat C_v, the magnetization M, the susceptibility χ, and the correlation length ξ, respectively:

$$C_v \sim t^{-\alpha}, \tag{1.5}$$

$$M \sim t^{-\beta}, \tag{1.6}$$

$$\chi \sim t^{-\gamma}, \tag{1.7}$$

$$\xi \sim t^{-\nu}, \tag{1.8}$$

where t is reduced temperature $t = (T - T_c)/T_c$. These Ising critical exponents obey the scaling relations

$$\alpha + 2\beta + \gamma = 2, \quad \nu d = 2 - \alpha. \tag{1.9}$$

These equations imply that there are only two independent exponents. The second scaling hypothesis category is data collapse, which can also be explained using the Ising model. The ratio

$$\xi/L = t^{-\nu} L^{-1} \tag{1.10}$$

should control the behavior of finite-size data close to T_c. Assume that $\chi(t)$ has the finite-size scaling form

$$\chi(t) \sim L^{\sigma} f(\xi/L) = L^{\sigma} f(t^{-\nu} L^{-1}) = L^{\sigma} g(tL^{1/\nu}) \tag{1.11}$$

for small t, then the infinite L scaling form should be

$$\chi(t) = L^{-\gamma}. \tag{1.12}$$

To reproduce this, the scaling function $g(x)$ must have the limit $g(x) \sim x^b$ as $x \to \infty$. We can determine the exponents as follows:

$$\chi(t) \sim L^\sigma g(tL^{1/\nu}) = L^\sigma (tL^{1/\nu})^b = t^b L^{\sigma + b/\nu}, \tag{1.13}$$

so $b = -\gamma, \sigma = \gamma/\nu$, and

$$\chi(t) \sim L^{\gamma/\nu} \tilde{C}(tL^{1/\nu}). \tag{1.14}$$

Similarly, for the magnetization:

$$M(t) \sim L^{\beta/\nu} \tilde{M}(tL^{1/\nu}). \tag{1.15}$$

Here $\tilde{C}$ and $\tilde{M}$ are unknown scaling functions. Both scaling forms show that when $T = T_c$, the data for $\chi(t)/L^{\gamma/\nu}$ and $M(t)/L^{\beta/\nu}$ simulated for different system sizes L should cross in the large-L limit at $T = T_c$.

The concept of a universality class is the centerpiece of the modern theory of critical phenomena. Two systems with the same critical exponent values and scaling functions are said to belong to the same universality class. Data collapse onto a scaling function supports the scaling hypotheses, while the fact that the scaling function is the same for different materials is truly remarkable. For example, the critical exponents of the 3D Ising model phase transitions are the same as those at the liquid–gas critical point, and they share the same Ising model universality class with $\alpha = 0.110(1), \beta = 0.3265(3), \gamma = 1.2372(5)$, and $\nu = 0.6301(4)$. Universality is a prediction of renormalization group theory, which states that the thermodynamic properties of a system near a critical point depend only on dimensionality and symmetry and are insensitive to the underlying microscopic properties of the system.

The idea of a renormalization group (RG) stems from Wilson's [13] essential

idea that the critical point can be mapped onto a fixed point of a suitably chosen transformation on the system's Hamiltonian. Here is an example of how to develop a real-space RG for the 1D Ising model. The energy E of the 1D Ising model is

$$\mathcal{H} = -J \sum_i s_i s_{i+1} \tag{1.16}$$

and the partition function is

$$\mathcal{Z} = \sum_{\{s_i\}} e^{-\mathcal{H}/k} = \sum_{\{s_i\}} \prod_i e^{K s_i s_{i+1}}, \tag{1.17}$$

where $K = J/kT$. One way to reduce the number of degrees of freedom is to describe the system in terms of two-spin cells, where the partition function is written as

$$\mathcal{Z} = \mathrm{Tr}(T^N) = \mathrm{Tr}(T^2)^{N/2} = \mathrm{Tr}(T')^{N/2} \tag{1.18}$$

with

$$T' = \begin{pmatrix} e^{2K} + e^{-2K} & 2 \\ 2 & e^{2K} + e^{-2K} \end{pmatrix}. \tag{1.19}$$

If we require T' to have the same form as T, then

$$T' = C \begin{pmatrix} e^{K'} & e^{-K'} \\ e^{-K'} & e^{K'} \end{pmatrix}. \tag{1.20}$$

The solution to this matrix equation is recurrence relations

$$K' = \frac{1}{2} \ln[\cosh(2K)] \tag{1.21}$$

and

$$C^4 = 4(e^{4K} + e^{-4K} + 2). \tag{1.22}$$

Suppose we have some initial value of the coupling constant K_0 such that $0 < K_0 < 1$. Then iteration of the recurrence relation produces a succession of values that approach $K = 0$. Accordingly, the point corresponding to $K = 0$ is called a *stable fixed point* of the recurrence relations, or a *critical point* of the 1D Ising model phase transition. This renormalization group description provides a foundation for understanding the scaling and universality, a calculation tool that permits us to obtain numerical estimates for the various critical exponents.

1.3 Spin glass

Spin glasses [14] are magnetic systems with disorder and frustration. The bonds in a spin glass are a mixture of roughly equal numbers of ferromagnetic bonds and antiferromagnetic bonds, and the essential physics of spin glasses lies not in the details of the microscopic interactions but rather in the competition between quenched ferromagnetic and antiferromagnetic interactions shown in Figure 1.3. The Hamiltonian $\mathcal{H}$ for a spin glass can be described as follows:

$$\mathcal{H} = -\sum_{i,j} J_{ij} S_i S_j + \sum_i h_i S_i, \tag{1.23}$$

where J_{ij} denotes the interactions between spins and S_i denotes the values of the spin components. If S_i has a single component, it's called an *Ising* spin glass. If S_i has two or three components, it is called an XY or a *Heisenberg* spin glass, respectively. A characteristic feature of spin glasses is that their dynamics are very slow at low temperatures, due to the development of a complicated "energy landscape" with many valleys separated by barriers.

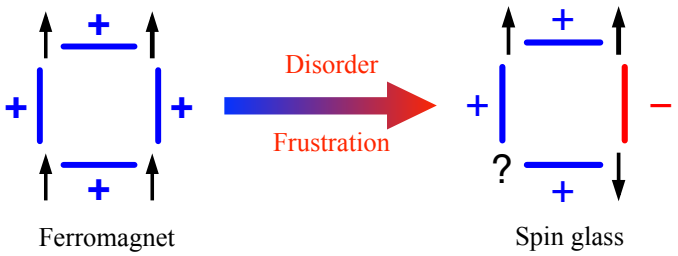

Figure 1.3: Disorder and frustration in a spin glass. Bonds marked "+" correspond to ferromagnetic couplings, "-" corresponds to an antiferromagnetic coupling. For a ferromagnet the energy is minimized by aligning all spins, in the case of spin glass, no spin configuration can simultaneously satisfy all couplings.

1.3.1 Phase transitions in spin glasses

Unlike a ferromagnet, where thermal fluctuations completely eliminate spontaneous magnetization above the critical temperature, spin glasses intrinsically do not have a visible spatial order. The spins in a spin glass are frozen with random orientations at low temperatures, and a spin overlap comparing two copies of a system with the same disorder rather than magnetization plays the role of the order parameter. We compute the spin overlap via two independent replicas at the same temperature as

$$q_{\alpha\beta} = \frac{1}{N} \sum_i S_i^\alpha S_i^\beta. \tag{1.24}$$

Above a spin glass's critical temperature T_c, the spins fluctuate widely and the overlap parameter tends to be zero. Below the critical temperature T_c, the spins are frozen with random orientations and the overlap parameter is one (or minus one). Spin glasses exhibit continuous phase transitions, and the specific heat C_v has a broad, smooth, and rounded maximum. However, the non-linear susceptibility χ_{nl} diverges at the critical temperature T_c. χ_{nl} can be measured experimentally and is

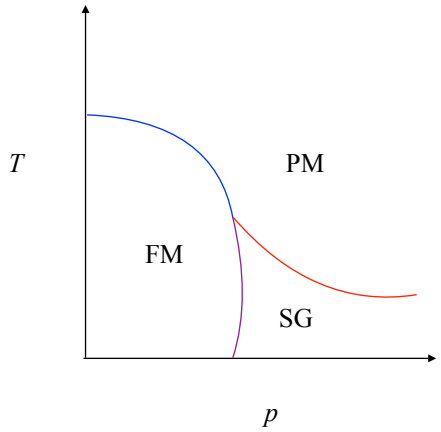

Figure 1.4: Sketch of phase diagram for three-dimensional Ising spin glass with bimodal disorder. The blue curve represents the transition between ferromagnetic (FM) and paramagnetic states (PM), the purple curve represents the transition between spin glass (SG) and ferromagnetic states (FM), the red curve represents the transition between spin glass (SG) and paramagnetic states (PM). T and p are temperature and fraction of antiferromagnetic bonds, respectively.

defined by the coefficient of h^3 in the expansion of the magnetization m:

$$m = \chi h - \chi_{\rm nl} h^3. \tag{1.25}$$

The non-linear susceptibility χ_{nl} is essentially the same as the spin glass susceptibility $\chi_{\rm SG}$:

$$\chi_{\rm SG} = \frac{1}{N} \sum_{i,j} [\langle S_i S_j \rangle^2]_{\rm av}. \tag{1.26}$$

where $[\cdots]_{\rm av}$ denotes an average over the quenched disorders. For the Edwards-Anderson model, it can be shown that

$$T^3 \chi_{\rm nl} = \chi_{\rm SG} - 2/3. \tag{1.27}$$

Another divergent quantity at T_c is the spin glass correlation length ξ, which can be

computed from the spin glass correlation function due to Ornstein-Zernicke approximation

$$[\chi_{\mathrm{SG}}(0)/\chi_{\mathrm{SG}}(k)]^{-1} \approx 1 + \xi^2 k^2, \tag{1.28}$$

where $\chi_{\mathrm{SG}}(k)$ is the vector-dependent spin glass susceptibility

$$\chi_{\mathrm{SG}}(k) = \frac{1}{N} \sum_{i,j} [\langle S_i S_j \rangle^2]_{\mathrm{av}} e^{ik\cdot(R_i - R_j)} \tag{1.29}$$

and R is position vector. On a finite lattice the momentum is discretized and one arrives at the expression

$$\xi = \frac{1}{2\sin(k_{\mathrm{min}}/2)} \left(\frac{\chi_{\mathrm{SG}}(0)}{\chi_{\mathrm{SG}}(k_{\mathrm{min}})} - 1 \right)^{1/2} \tag{1.30}$$

with

$$k_{\mathrm{min}} = \frac{2\pi}{L}(1, 0, 0). \tag{1.31}$$

The phase diagram of the 3D lattice $\pm J$ Ising spin glass model is sketched in figure 1.4. p is the fraction of antiferromagnetic bonds, we only consider $p \leq 1/2$ because of the symmetry $p \to 1 - p$. While the high-temperature phase is always paramagnetic (PM), at low temperatures there is a ferromagnetic (FM) phase for small frustration, and a spin glass phase (SG) with vanishing magnetization for sufficiently large frustration.

The critical exponents of phase transitions in spin glasses, α, β, γ, and ν, describe the behavior of the specific heat C_v, overlap parameter q, susceptibility χ_{SG}, and correlation length ξ_L, respectively:

$$C_v \sim t^{-\alpha}, \tag{1.32}$$

$$q \sim t^{-\beta}, \tag{1.33}$$

$$\chi_{\mathrm{SG}} \sim t^{-\gamma}, \tag{1.34}$$

$$\xi \sim t^{-\nu}. \tag{1.35}$$

This allows us to study critical properties and universality class in spin glasses via scaling relations.

1.3.2 Long-range and short-range spin glass model

For the Sherrington-Kirkpatrick (SK) model [15], a system of N Ising spins with zero external fields and the range of each interaction can be infinite (every spin interacts with every other one). the Hamiltonian is described as follows:

$$\mathcal{H} = -\frac{1}{\sqrt{N}} \sum_{i,j} J_{ij} S_i S_j. \tag{1.36}$$

The couplings J_{ij} are chosen from a Gaussian distribution with mean zero and variance one; the $\frac{1}{\sqrt{N}}$ rescaling ensures a non-divergent thermodynamic limit for free energy per spin as well as other thermodynamic quantities. The equilibrium solution of the model was found by Giorgio Parisi with the replica method, and subsequent work on the interpretation of the Parisi solution revealed the complex nature of a glassy low temperature phase characterized by ergodicity breaking, ultrametricity, and non-self-averageness [16, 17, 18, 19]. The SK model has a line of transitions, known as the Almeida–Thouless (AT) line (shown in Figure 1.5), in a magnetic field. The AT line separates a spin glass phase with divergent relaxation times and "replica symmetry breaking" from a paramagnetic "replica symmetric" phase with finite relaxation times. Therefore, the SK model has a finite-temperature spin-glass phase transition in a field.

In the Edwards-Anderson model [20], spins are arranged on a D-dimensional lattice with only nearest neighbor interactions and periodic boundary conditions in all directions. Its Hamiltonian is

$$\mathcal{H} = -\sum_{i,j} J_{ij} S_i S_j, \tag{1.37}$$

where i, j indicates a sum over nearest neighbors. The coupling constants J_{ij} are independent random variables drawn from a given distribution with mean zero and variance one. In the original version proposed by Edwards and Anderson, the spin was assumed to be the Heisenberg one with three spin components. However, Ising spin glasses have been widely used in numerous simulations because of their simplicity. Much of what we know about the Edwards-Anderson model comes from numerical simulations, and there has been a general consensus that for Ising systems with $D \geq 2.5$ [21], a spin glass transition occurs in zero field. The upper critical dimension of the Ising spin glass, above which mean field results should apply, is expected to be six [22]. Phase transitions in the magnetic field for the Edwards-Anderson model are controversial, and two main scenarios have been proposed for resolving this issue. In the "droplet picture" [23, 24, 25], there is no AT line in any finite-dimensional spin glass. By contrast, the "replica symmetry breaking" picture [26, 27] predicts that the behavior of short-range Ising spin glasses is similar to that of the infinite-range SK model with an AT line. Many problems can be mapped onto short-range systems. As such, whether having a field term could destroy the spin glass state has far-reaching impact [28]. Most of recent numerical studies point to the absence of an equilibrium transition under finite fields [28, 29], however, there is still no consensus on this issue because there seem to be quite large corrections to finite-size scaling. Therefore, better models such as one-dimensional spin-glass model

with power-law interactions and spin glasses on scale free networks can be used to probe short-range models by tuning the exponent of the power-law interactions or the exponent that describes the decay of the interaction degree in the scale-free graph [30, 31].

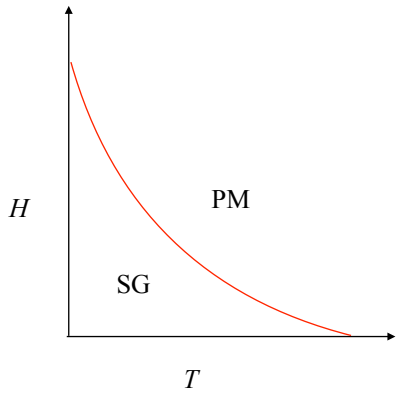

Figure 1.5: Sketch of Almeida–Thouless (AT) line for the SK model. The AT line separates a spin glass phase with divergent relaxation times and "replica symmetry breaking" from a paramagnetic "replica symmetric" phase with finite relaxation times.

1.3.3 Applications of spin glasses

The study of spin glasses has led to a variety of applications to problems in neural networks [32], graph theory [33, 2], protein folding [34], self-organized criticality [35], combinatorial optimization [36], quantum information theory [37, 38, 3], economics [39], and many other areas. In this thesis, I attempt to illustrate how the spin glass model can establish fruitful links and contribute new insights to a wide range of interdisciplinary applications.

2. NUMERICAL METHODS FOR SPIN GLASSES

For a spin glass system in equilibrium with a heat bath, the probability P_s of being in a given state s depends only on the energy E_s:

$$P_s = \frac{1}{Z} e^{-E_s/kT}. \tag{2.1}$$

where k is Boltzmann constant, T is the temperature and Z is the partition function of the system. To sample the average of an observable $\langle O \rangle$ in the system, we sum over all possible configurations analytically:

$$\langle O \rangle = \frac{1}{Z} \sum_s O_s e^{-E_s/kT}. \tag{2.2}$$

For a system with N spins, there are a total of 2^N possible configurations. Even a small lattice with $N = 100$ is impossible to study using "brute force", especially systems with strong interactions between spins. We have no choice but to seek an approximation if we want to correctly estimate the observables without exploring the entire configuration space. Unlike the case of ferromagnets, which display spatial symmetries that greatly simplify their physical and mathematical analyses, the absence of symmetries in spin glasses enormously complicates the analysis of their behavior. Mean field theory has almost always served as an invaluable guide to the low-temperature behavior of statistical mechanical systems. However, in the Edwards-Anderson model, there are finite corrections to the mean field (especially large in one or two dimensions). Because of this failure of mean field theory to provide a correct description of the low-temperature phase in any finite dimensional spin glass [14, 40, 41], it is necessary to develop efficient numerical algorithms—especially

for those cases where exact results such as critical temperature, critical exponents, avalanche size distributions, and ground states are not available, due to formidable mathematical difficulties and NP-hard complexity. Over the last few decades, the development of efficient Monte Carlo methods such as parallel tempering [42] and population annealing [43] has helped us understand these systems at a much deeper level. However, most numerical studies are still plagued by corrections to finite-size scaling due to the small system sizes currently available, so more powerful algorithms are needed to overcome the computational limitations. In this chapter I review state-of-the-art numerical methods for spin glass simulations.

2.1 Metropolis algorithm

The Metropolis algorithm [44] constructs an ergodic Markov chain that satisfies the detailed balance property with respect to the stationary Boltzmann distribution. If we generate a Markov chain of successive states $s_1 \to s_2 \to ...$, each new state is generated from the previous state with a carefully-designed transition probability $p(s_1 \to s_2)$. The outline of the algorithm is as follows:

1. Starting from a configuration s_1 with known energy E_{s_1}, take a random walk and make a trial change to obtain a new configuration s_2.

2. Compute the energy E_{s_2} of trial configuration s_2.

3. If $E_{s_2} \leq E_{s_1}$, accept the new configuration; If $E_{s_2} > E_{s_1}$, accept the new configuration with probability

$$p(s_1 \to s_2) = e^{-\frac{(E_{s_2} - E_{s_1})}{kT}}. \tag{2.3}$$

The process is repeated until equilibrium is reached for temperature T. To understand how the Metropolis algorithm works, note that at low temperatures the algorithm will almost always drive the system towards a lower energy. However, at

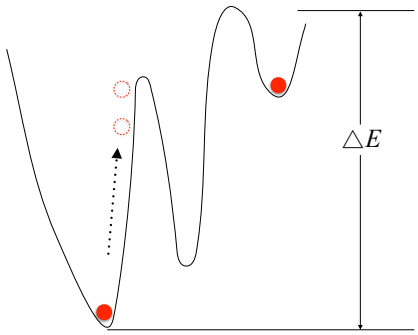

Figure 2.1: Sketch of a rough energy landscape of spin glass. A Monte Carlo move is unlikely if the height of the energy barrier ΔE is large, especially at low temperatures. In this case, a simple Monte Carlo simulation will stall and the system will be stuck in the metastable state.

high temperatures the transition probability is close to one, and the algorithm tends to randomize all of the configurations. The Metropolis algorithm is generally used for sampling multi-dimensional distributions, and its error is independent of the space dimension [45]. However, the disadvantage of this Markov-chain approach is that the new state usually depends on the previous state at low temperatures, and thus they are correlated. To ensure that the measurement of an observable is not biased by correlated configurations, measurements can only be taken after autocorrelation time. However, the dynamics of spin system can be extremely slow at low temperature. Imagine that a simple spin flip can produce a huge change in the energy ΔE of a spin glass system with a rough energy landscape (shown in figure 2.1). The effect of this will be that the probability of new configurations being accepted is very small, so a simple Monte Carlo simulation will stall and the system will be stuck in the metastable state, which result in a long autocorrelation time and large error bars of observables. Therefore, in spin glasses with a rough energy landscape we need to come up with better ideas.

2.2 Parallel tempering

Parallel tempering, also known as replica exchange Markov-Chain Monte Carlo (MCMC) sampling [42], is a simulation method aimed at improving the dynamic properties of Monte Carlo method simulations of physical systems. Essentially, N_T replicas of the system, randomly initialized, are run at a range of temperatures $\{T_1, T_2, ..., T_{N_T}\}$. Configurations at different temperatures are exchanged based on the Metropolis criterion

$$p(E_i, T_i \rightarrow E_{i+1}, T_{i+1}) = \min\{1, e^{\Delta E \Delta\beta}\}, \tag{2.4}$$

where $\Delta\beta = 1/T_{i+1} - 1/T_i$ is the difference between the inverse temperatures and $\Delta E = E_{i+1} - E_i$ is the difference in the energy of the two replicas. The idea behind this method is to make configurations at high temperatures available to the simulations at low temperatures, and vice versa. This results in a very robust ensemble that is able to sample both low- and high-energy configurations. An example shown in figure 2.2 demonstrates that parallel tempering outperforms simple Monte Carlo method in a rough energy landscape.

One important aspect of the parallel tempering algorithm is that optimal temperature intervals must be carefully chosen [45]. When the temperatures are too far apart, the energy distributions at the individual temperatures will not overlap enough, and many moves will be rejected. If the temperatures are too close, CPU time will be wasted. Usually the most accurate data for a fixed amount of computation are obtained if we ensure that the acceptance probabilities are approximately independent of the temperature, roughly between $20\% - 80\%$ [46].

In practice, parallel tempering enables us to simulate intermediate size systems, e.g., $\sim 10^3$ spins, at low temperatures [41].

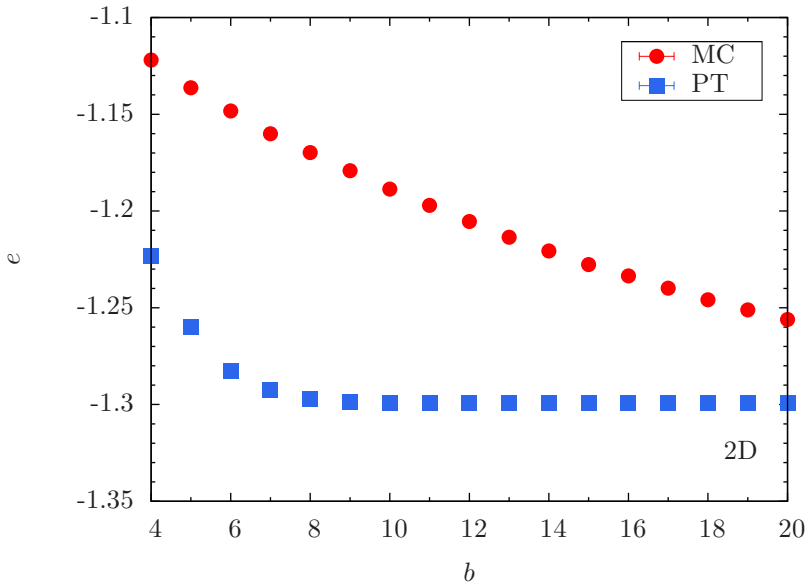

Figure 2.2: This figure shows energy per spin e as a function of Monte Carlo time (measured in lattice sweeps) $t = 2^b$ with (blue dots) and without (red dots) parallel tempering (system size $N = 64$, temperature $T = 0.21$) for a 2D square lattice. The system is in equilibrium when e becomes approximately flat and fluctuates around a mean value. The data show that without parallel tempering (PT), the system does not reach equilibrium even after 2^{20} MCS. In contrast, the system thermalizes much faster with parallel tempering and reaches equilibrium after only a few thousand Monte Carlo sweeps.

2.3 Houdayer cluster algorithm

For ferromagnets, the Metropolis algorithm is plagued by large autocorrelation times at criticality. Empirically the autocorrelation time grows proportional to the correlation length $\tau \propto \xi^z$, with a dynamical critical exponent $z \approx 2$. Since ξ diverges at critical temperature, the Metropolis algorithm severely suffers from critical slowing down. The problem of critical slowing down can be overcome by cluster algorithms. By comparing thermal phase transitions to percolation transitions and applying Fortuin-Kasteleyn transformation to spin configurations, Swendsen-Wang and Wolff [47, 48] cluster algorithms have been developed to greatly reduce the dy-

namical critical exponent. Although the generalization is even valid for spin glasses. The corresponding algorithm is inefficient when frustration is introduced into Hamiltonian [49]. Therefore, these cluster algorithms have been most useful for system without frustration.

The Houdayer cluster move is a rejection-free method [50] for 2D spin glasses. The use of clusters makes global updates possible and leads to a speedup of several orders of magnitude. Essentially, M replicas are run at the same temperature, and the q-space between the two random replicas α and β is then defined as

$$q_i = S_i^{\alpha} S_i^{\beta}. \tag{2.5}$$

There are two domains in the q-space, the sites with $q_i = 1$ and the sites with $q_i = -1$, and clusters are defined to be the connected parts of these domains. One site with $q_i = -1$ in the q-space is randomly chosen, and the cluster to which it belongs is flipped in both configurations. Since the total energy of the two replicas is unchanged by this transformation, acceptance of this cluster move is guaranteed, which allows a much faster thermalization because the two replicas are mixed together very quickly. An example shown in figure 2.3 demonstrates that simulations using Houdayer cluster moves are superior to vanilla parallel tempering at very low temperature. The drawback of Houdayer cluster algorithm is that it only works for 2D (site percolation threshold $p_c = 0.59$) Ising spin glass. Usually there are about as many sites with $q_i = 1$ as with $q_i = 1$, flipping one of those big clusters in both replicas is the same as exchanging the replicas as soon as the site percolation threshold is less than 0.5 which essentially forbids all lattices of dimension $D > 2$ or with more than nearest neighbour connections in $D = 2$.

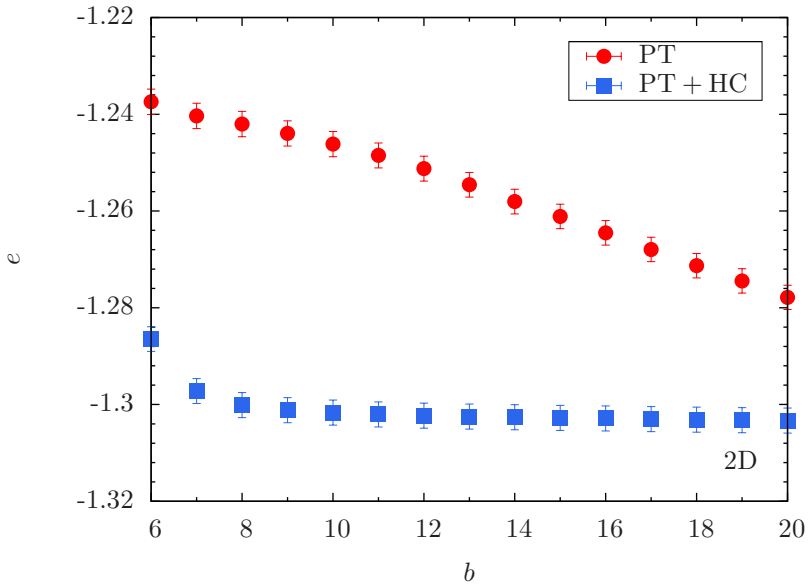

Figure 2.3: This figure shows energy per spin e as a function of Monte Carlo time (measured in lattice sweeps) $t = 2^b$ with (blue dots) and without (red dots) Houdayer cluster moves (system size $N = 64$, temperature $T = 0.02$) for a 2D square lattice. The system is in equilibrium when e becomes approximately flat and fluctuates around a mean value. The data show that without Houdayer cluster moves (HC), the system does not reach equilibrium even after 2^{20} MCS. However, it thermalizes much faster with Houdayer cluster moves and reaches equilibrium after only a few thousand Monte Carlo sweeps. Note temperatures for the simulations here are extremely low (about 1/10 of temperatures in figure 2.2), the simple Monte Carlo method will be useless.

2.4 Test for equilibration

Spin glass dynamics is slow at low temperatures due to the complicated energy landscape. To speed things up, most spin glass simulations now use the Metropolis algorithm and parallel tempering combined with some cluster algorithms. The Metropolis algorithm is widely popular in statistical physics; we start with a random configuration and try to explore the phase space more efficiently, both vertically and horizontally, with parallel tempering and a cluster algorithm. The systems usually have to evolve for many Monte Carlo steps before an equilibrium state at a given

temperature is obtained. Once equilibration time has been reached, the observables become approximately flat and fluctuate around a mean value; the system is in thermal equilibrium and the observables can be measured.

For spin glasses with Gaussian disorder, we can use a strong equilibration test to ensure that the system is in thermal equilibrium. The internal energy per spin is given by

$$U = -\frac{1}{N}\sum_{i,j}[\langle J_{ij}S_iS_j\rangle]_{\text{av}}, \tag{2.6}$$

where $\langle\cdots\rangle$ represents the Monte Carlo average for a given set of bonds and $[\cdots]_{\text{av}}$ denotes an average over the Gaussian disorder. We can perform an integration by parts over J_{ij} to relate U to the average link overlap [51]:

$$U(q_l) = -\left[\left\langle \frac{z}{2}\frac{1-q_l}{T}\right\rangle\right]_{\text{av}}, \tag{2.7}$$

where q_l is the link overlap

$$q_l = \frac{1}{Nd}\sum_{i,j} s_i^\alpha s_j^\alpha s_i^\beta s_j^\beta \tag{2.8}$$

and z is the number of neighbors per site. The data for both quantities approach equilibrium from opposite directions. Figure 2.4 shows equilibration test for spin glasses with Gaussian disorder on a 2D square lattice, data for the energy have to equate to data for the energy computed from the link overlap. This equilibration test does not work for spin glasses with bimodal interactions.

2.5 Finite size scaling for spin glasses

Finite size scaling is a method for finding the critical exponents and the critical temperature by observing how the measured quantities change for different system

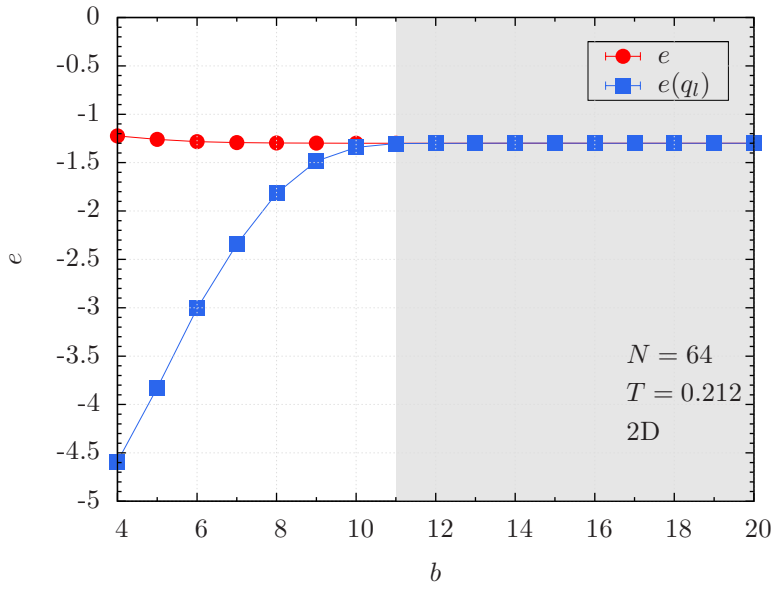

Figure 2.4: Equilibration test for a 2D square lattice with $N = 64$ spins at $T = 0.212$. Once the data for the energy e and the energy $e(q_l)$ computed from link overlap q_l agree, the system is in thermal equilibrium (shaded area).

sizes. Three different useful quantities can be applied with finite size scaling for spin glass: the Binder ratio [52], spin glass susceptibility, and correlation length. These have the following scaling forms:

$$g(t) \sim \tilde{G}(tL^{1/\nu}), \tag{2.9}$$

$$\chi_{\mathrm{SG}}(t) \sim L^{\gamma/\nu}\tilde{C}(tL^{1/\nu}), \tag{2.10}$$

$$\xi(t)/L \sim \tilde{X}(tL^{1/\nu}), \tag{2.11}$$

where $g(t) = (1/2)(3 - \langle q^4\rangle/\langle q^2\rangle^2)$, $\tilde{G}$, $\tilde{C}$, and $\tilde{X}$ are unknown scaling functions, t is reduced temperature $t = (T - T_c)/T_c$ and L is side length. These scaling forms imply that when $T = T_c$ (or $t = 0$) , the data for $g(t)$, $\chi_{\mathrm{SG}}(t)/L^{\gamma/\nu}$, and $\xi(t)/L$ with different system sizes L should cross in the large-L limit at $T = T_c$. Also, they should

collapse onto the same curve if we plot $g(t)$, $\chi_{\mathrm{SG}}(t)/L^{\gamma/\nu}$, and $\xi(t)/L$ as a function of $tL^{1/\nu}$. This method is illustrated in figure 2.5 and 2.6 for the Sherrington-Kirkpatrick Ising spin glass model. The figure 2.5 shows the sketch of Binder ratio as a function of temperature for several small system sizes, the vertical dashed line marks the exactly known value of the critical temperature T_c. The figure 2.6 shows a sketch of finite-size scaling analysis of the data for the exact values of the critical exponent ν. Close to the transition the data fall onto a universal curve, showing that ν is the correct value of the critical exponent.

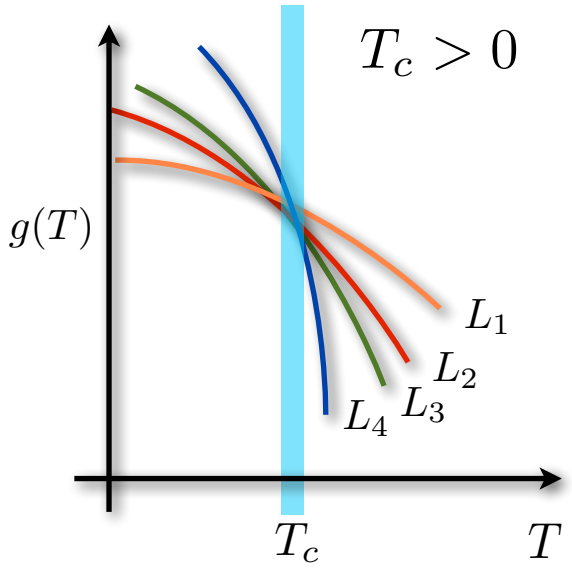

Figure 2.5: Sketch of Binder ratio $g(T)$ for the Sherrington-Kirkpatrick model with different system sizes N as a function of temperature T. The data cross at a point (shaded area) and we obtain the critical temperature T_c.

Generally, use of the correlation length [53] to locate the critical temperature in spin glasses is better than use of the Binder ratio. This is because for the Binder ratio, the data merge but do not clearly splay out in the low temperature region,

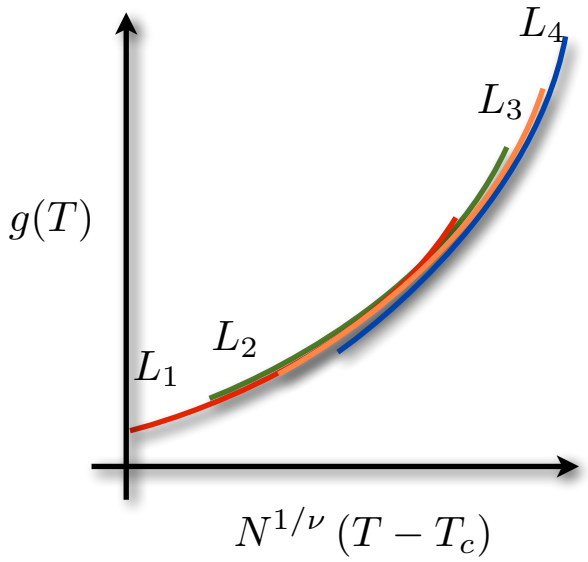

Figure 2.6: Sketch of finite-size scaling analysis of Binder ratio $g(T)$ for the Sherrington-Kirkpatrick model with different system sizes N as a function of $N^{1/\nu}(T - T_c)$. Close to the transition the data fall onto a universal curve, showing that ν is the correct value of the critical exponent.

whereas in the results for the correlation length, the data intersect at the critical temperature and splay out again at lower temperatures. For spin glasses on a graph without geometry, the Binder ratio and susceptibility but not the correlation length can be measured and used to determine the critical temperature and exponents [2].

2.6 Optimization algorithms

Ising spin glasses are prototypical models for disordered systems and have played a central role in statistical physics during the last four decades. In the area of optimization, spin glasses provide a rich class of test problems that are a challenge for most optimizers, mainly because of the large number of local optima and the existence of rough energy landscapes. On the one hand, progress in the theory of combinatorial optimization, and in particular the development of new and more efficient algorithms, contributes to our understanding of spin glass physics. On the other hand, spin glass

physics can also help shed light on some basic, yet unsolved, questions in computer science. Problems that are originally formulated as purely combinatorial tasks can be equivalently rewritten as spin glass models, by identifying the cost function with a Hamiltonian. Applying statistical mechanics tools at a temperature close to $T = 0$ may thus unveil many properties of the original problem and its cost-function minima [54].

Many generally applicable computational methods have been developed to solve hard combinatorial optimization problems. Exact algorithms that efficiently explore the tree of system states include branch-and-cut algorithms [55], exact algorithms that will terminate and are guaranteed to provide the minimum energy solution, but unfortunately these tend to be slow. Heuristic methods provide good, but not necessarily optimal solutions. They have the advantages of being easy to program and of being very fast, which often allows researchers to quickly tackle relatively large systems with little effort. Widely popular heuristic optimization algorithms include Monte Carlo methods: simulated annealing [36], parallel tempering [56], and population annealing [57]; evolutionary algorithms: genetic algorithms [58], particle swarm optimization [59], ant colony optimization, and extremal optimization [60]; tabu search [61]; hysteretic optimization [62]; and quantum annealing [63].

Usually, heuristic algorithms are used for problems that cannot be easily solved. Classes of time complexity are defined to distinguish problems according to their "hardness" and illustrated in figure 2.7. Class P consists of decision problems solvable in polynomial time, and class NP consists of decision problems that are "verifiable" in polynomial time. A major open question in theoretical computer science is whether every problem whose solution can be quickly verified by a computer can also be quickly solved by a computer. It currently appears that P$\neq$ NP, meaning that we have plenty of examples of problems for which we can quickly verify potential

answers but which we cannot solve quickly, such as the traveling salesman problem, the Boolean satisfiability problem, and finding spin glass ground states. There is a class of NP problems that are NP-complete, which means that if you can solve one of them, you can use the same method to solve any other NP problem quickly. Finally, the class of NP-hard problems is the class of problems that are NP-complete or harder. NP-hard problems have the same characteristic as NP-complete problems but they do not necessary belong to the class NP, that is, the class of NP-hard problems also includes problems for which no algorithm at all can be provided. For the spin glass ground states problem, Barahona [64] proved in 1982 that the 3D spin glass model and the planar model with an external field are NP-complete. The complexity result bars algorithms only from solving all instances of the problem in polynomial time. Typical spin glasses are random mixtures of coupling constants, and it's entirely possible that the average spin glass problem can be solved in polynomial time, even though the worst case may be exponential. The ground-state properties capture most of the low temperatures physics, therefore we might be able to study the nature of spin glass state at low temperature without solving the worst problems. A good optimization algorithm is not expected to turn the exponential scaling into a polynomial one, however, smaller scaling constants will potentially give substantial speedup. In the next few chapters we will develop cluster algorithms that speedup thermalization of spin glasses and fair sampling of their ground states.

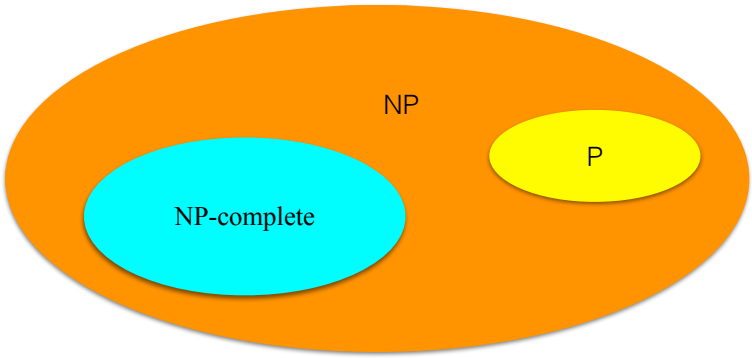

Figure 2.7: This figure [65] illustrates the relationships among the three categories: P, NP, and NP-complete. The existence of problems within NP but outside both P and NP-complete, under assumption P $\neq$ NP, was established by Ladner's theorem [66]. For spin glasses, non-planar model and the planar model with an external field are NP-complete, planar model is P, it is unclear whether there are spin glass problems that are in the complexity class NP but are neither in the class P nor NP-complete.

3. BOOLEAN DECISION PROBLEMS WITH COMPETING INTERACTIONS ON SCALE-FREE NETWORKS: EQUILIBRIUM AND NONEQUILIBRIUM BEHAVIOR IN AN EXTERNAL BIAS *

Scale-free networks play an integral role in nature, as well as in industrial, technological and sociological applications [67]. In these networks, the edge degrees $\{k_i\}$ (the number of neighbors each node has) are distributed according to a power law λ, with the probability $\wp_k$ for a node to have k neighbors given by

$$\wp_k \quad \propto \quad k^{-\lambda}. \tag{3.1}$$

In the meantime, there have been many studies of Boolean variables on scale-free networks and, more recently, even with competing interactions [68, 33, 69, 70, 2]. There is general consensus that stable ferromagnetic and spin-glass phases emerge in these complex systems [2] and that for particular choices of the decay exponent λ the critical temperature diverges, i.e., Boolean variables with competing interactions are extremely robust to local perturbations.

However, the behavior of these intriguing systems in an external magnetic field—which can be interpreted as a global bias—remains to be fully understood. Although a replica ansatz works well when determining the critical temperature of the system [33, 2] in zero field, it is unclear if a stable spin-glass state persists in a field. In addition, when studying the system without local perturbations (i.e., at zero temperature), it is unclear if "damage" in the form of avalanches of Boolean variable

*Reprinted with permission from "Boolean decision problems with competing interactions on scale-free networks: Equilibrium and nonequilibrium behavior in an external bias" by Zheng Zhu, Juan Carlos Andresen, M. A. Moore, and Helmut G. Katzgraber, 2014, Phys. Rev. E 89, 022118 Copyright 2014 by American Physical Society [31].

flips triggered by a field can spread easily across the system.

In this chapter I tackle the two aforementioned problems numerically and show that at finite temperature Boolean variables with competing interactions are remarkably robust to global external biases. In particular, I show that a de Almeida–Thouless line [71] persists to a regime of λ where the system is not in the mean-field Sherrington-Kirkpatrick [15] universality class, i.e., when $\lambda < 4$ [33, 2].

Furthermore, I probe for the existence of self-organized criticality (SOC) when driving the system at zero temperature with an external magnetic field across a hysteresis loop. SOC is a property of large dissipative systems to drive themselves into a scale-invariant critical state without any special parameter tuning [72, 73, 74, 35, 75]. It is a phenomenon found in many problems ranging from earthquake statistics to the structure of galaxy clusters. As such, studying SOC on scale-free networks might help us gain a deeper understanding on how avalanches, i.e., large-scale perturbations, might spread across scale-free networks that are so omnipresent in nature. Recent simulations [76] have shown that a diverging number of neighbors is the key ingredient to obtain SOC in glassy spin systems. In scale-free graphs the average edge degree diverges if $\lambda \leq 2$ (average number of neighbors $\langle k \rangle \propto \sum_{k=3} k^{1-\lambda}$). As such, it might be conceivable that in this regime spin glasses on scale-free graphs exhibit SOC. However, it is unclear what happens for $\lambda > 2$ where the number of neighbors each spin has is finite in the thermodynamic limit ($N \to \infty$), or how the fraction of ferromagnetic versus antiferromagnetic bonds influences the scaling of the avalanche distributions. Within the spin-glass phase, for Gaussian disorder and bimodal disorder with the same fraction p of ferromagnetic and antiferromagnetic bonds, we find that when $\lambda \leq 2$ Boolean variables with competing interactions always display SOC like the mean-field Sherrington-Kirkpatrick model [35]. For $\lambda > 2$ and with bimodal disorder, a critical line in the p–λ plane emerges along which

perturbations to the system are scale free, but not self-organized critical because the fraction of ferromagnetic bonds has to be carefully tuned. The latter is reminiscent of the behavior found in the random-field Ising model [77, 78, 79, 80, 81], as well as random-bond [82] and random-anisotropy Ising models [83].

This chapter is structured as follows. Section 3.1 introduces the Hamiltonian studied, followed by numerical details, observables, and results from equilibrium Monte Carlo simulations in Sec. 3.2. Section 3.3 presents our results on nonequilibrium avalanches on scale-free graphs, followed by concluding remarks. In the appendix A we outline our analytical calculations to determine the de Almeida–Thouless line for spin glasses on scale-free graphs.

3.1 Model

The Hamiltonian of the Edwards-Anderson Ising spin glass on a scale-free graph in an external magnetic field is given by

$$\mathcal{H}(\{s_i\}) = -\sum_{i<j}^{N} J_{ij}\varepsilon_{ij}s_i\, s_j - \sum_i H_i s_i, \tag{3.2}$$

where the Ising spins $s_i \in \{\pm 1\}$ lie on the vertices of a scale-free graph with N sites and the interactions are given by

$$\mathcal{P}(J_{ij}, \varepsilon_{ij}) = \wp_J(J_{ij}) \left[\Big(1 - \frac{K}{N}\Big)\delta(\varepsilon_{ij}) + \frac{K}{N}\delta(\varepsilon_{ij} - 1) \right]. \tag{3.3}$$

If a bond is present, we set $\varepsilon_{ij} = 1$, otherwise $\varepsilon_{ij} = 0$. K represents the mean connectivity of the scale-free graph. The connectivity of site i, $k_i := \sum_j \varepsilon_{ij}$, is sampled from a scale-free distribution as done in Ref. [2]. The interactions J_{ij} between the spins are independent random variables drawn from a Gaussian distribution with

zero mean and standard deviation unity, i.e.,

$$\wp_J(J_{ij}) \sim \exp\left(-J_{ij}^2/2\right). \tag{3.4}$$

In the nonequilibrium studies we also study bimodal-distributed disorder where we can change the fraction of ferromagnetic bonds p, i.e.,

$$\wp_J(J_{ij}) = p\delta(J_{ij}+1) + (1-p)\delta(J_{ij}-1). \tag{3.5}$$

Finally, for the finite-temperature studies we use random fields drawn from a Gaussian distribution with zero mean and standard deviation H_r in Eq. (3.2), instead of a uniform field. This allows us to perform a detailed equilibration test of the Monte Carlo method [51, 84].

The scale-free graphs are generated using preferential attachment with slight modifications [85]. Details of the method are described in Ref. [2]. We impose an upper bound on the allowed edge degrees, $k_{\max} = \sqrt{N}$. Although we can, in principle, generate graphs with k exceeding $\sqrt{N}$, the ensemble is poorly defined in this case: Even randomly chosen graphs cannot be uncorrelated [86, 87, 88]. Furthermore, to prevent dangling ends that do not contribute to frustrated loops in the system, we set a lower bound to the edge degree, namely $k_{\min} = 3$.

3.2 Equilibrium properties in a field

In equilibrium, the behavior of spin glasses in a magnetic field is controversial [28, 89, 29, 84, 90, 91]. While the infinite-range (mean-field) Sherrington-Kirkpatrick (SK) model [15] has a line of transitions at finite field known as the de Almeida–Thouless (AT) line [71] that separates the spin-glass phase from the paramagnetic phase at finite fields or temperatures, it has not been definitely established whether

an AT line occurs in systems with short-range interactions. Spin glasses on scale-free networks are somewhat "in between" the infinite-range and short-range limits depending on the exponent λ. As such, it is unclear if a spin-glass state will persist when an external field H is applied, especially when the spin-glass transition at zero field occurs at finite temperatures, i.e., for $\lambda > 3$.

Note that spin glasses on scale-free graphs share the same universality class as the SK model if $\lambda > 4$ [2]. As such, in this regime, one can expect an AT line. However, for $3 < \lambda < 4$, where $T_c < \infty$, the critical exponents depend on the exponent λ [33, 2]. Therefore, it is unclear if a spin-glass state in a field will persist. For $\lambda \leq 3$ the critical temperature diverges with the system size, i.e., we also expect the system to have a spin-glass state for finite fields. We therefore focus on two values of λ, namely $\lambda = 4.50$ (deep within the SK-like regime because $\lambda = 4$ has logarithmic corrections) [2] and $\lambda = 3.75$ (where the existence of an AT line remains to be determined).

3.2.1 Observables

In simulations, it is most desirable to perform a finite-size scaling (FSS) of dimensionless quantities. One such quantity, the Binder ratio [92], turns out to be poorly behaved in an external field in short-range systems [93]. Therefore, to determine the location of a spin-glass phase transition we measure the connected spin-glass susceptibility given by

$$\chi = \frac{1}{N} \sum_{i,j} [(\langle s_i s_j \rangle_T - \langle s_i \rangle_T \langle s_j \rangle_T)^2]_{\text{av}}, \tag{3.6}$$

where $\langle \cdots \rangle_T$ denotes a thermal average and $[\cdots]_{\text{av}}$ an average over both the bond disorder and different network instances. N is the number of spins. To avoid bias,

each thermal average is obtained from separate copies (replicas) of the spins. This means that we simulate four independent replicas at each temperature.

For any spin glass outside the mean-field regime, the scaling behavior of the susceptibility is given by [2]

$$\chi = N^{2-\eta}\widetilde{C}\left(N^{1/\nu}[\beta - \beta_c]\right) , \tag{3.7}$$

where ν and η are the correlation length and susceptibility exponents, respectively, and $\beta_c = 1/T_c$ is the inverse temperature for a given field strength H_r.

For $\lambda < 4$ (see the appendix A for details) we expect the critical exponent $\gamma = 1$. This is only possible if $2 - \eta = 1/\nu$ in Eq. (3.7). Using the standard scaling relation $\alpha + 2\beta + \gamma = 2$, the hyperscaling relation $d\nu = 2 - \alpha$ (which we assume will hold when $\lambda < 4$), and allowing for the nonstandard meaning of ν in this paper (it is equal to $d\nu$ in standard notation where d is here the dimensionality of the system), it follows for $\lambda < 4$, where $\beta = 1/(\lambda - 3)$ (see the appendix A and Ref. [33]) that

$$\nu = \frac{\lambda - 1}{\lambda - 3} \quad \text{and} \quad \eta = 2 - \frac{1}{\nu}. \tag{3.8}$$

For the case of $\lambda = 3.75$ this means that $\nu = 11/3$ and therefore $\eta = 2 - 1/\nu = 19/11$. As such, curves of $\chi/N^{3/11}$ should have the same scaling behavior as the Binder ratio.

For $\lambda > 4$, the finite-size scaling form presented in Eq. (3.7) is replaced by [84, 30]

$$\chi = N^{1/3}\widetilde{C}\left(N^{1/3}[\beta - \beta_c]\right) . \tag{3.9}$$

In this case the scaling is simpler because the exponents are fixed and independent of λ, i.e., $1/\nu = 2 - \eta = 1/3$. Here, curves of $\chi/N^{1/3}$ should have the same scaling behavior as the Binder ratio. Performing a finite-size scaling of the data therefore

allows one to detect the transition to high precision.

Finally, note that the aforementioned study is, strictly speaking, only valid at zero field. Although $\gamma = 1$ across the AT line, there is no explicit calculation of the critical exponent β in a field. While our data suggest that the values of the zero-field exponents might be the same as those for finite external fields, the accuracy of our results for the exponents in a field is limited by large finite-size corrections.

3.2.2 Equilibration scheme and simulation parameters

The simulations are done using the parallel tempering Monte Carlo method [94, 42]. The spins couple to site-dependent random fields H_i chosen from a Gaussian distribution with zero mean $[H_i]_{\rm av} = 0$ and standard deviation $[H_i^2]_{\rm av}^{1/2} = H_r$. Simulations are performed at zero field as well as at $H_r = 0.1$, 0.2, 0.3, and 0.4. Using Gaussian disorder, we can use a strong equilibration test to ensure that the data are in thermal equilibrium [51, 84, 2]. Here, the internal energy per spin

$$U = (1/N)[\langle \mathcal{H} \rangle_T]_{\rm av} \,, \tag{3.10}$$

with $\mathcal{H}$ defined in Eq. (3.2), has to equate an expression derived from both the link overlap q_4 given by

$$q_4 = \frac{1}{N_b} \sum_{i,j} \varepsilon_{ij} s_i^\alpha s_j^\alpha s_i^\beta s_j^\beta \,, \tag{3.11}$$

and the spin overlap

$$q = \frac{1}{N_b} \sum_{i} s_i^\alpha s_i^\beta \,. \tag{3.12}$$

Here α and β represent two copies of the system with the same disorder and N_b represents the number of neighbors each spin has for a given sample (graph instance). Note that because in Eq. (3.6) we already simulate four replicas, we actually perform an average over all four-replica permutations.

The system is in thermal equilibrium if

$$U = U(q_4) = -\frac{1}{T}\left[\left\langle \frac{N_b}{N}(1-q_4) + H_r^2(1-q)\right\rangle\right]_{\text{av}} . \tag{3.13}$$

Sample data are shown in Fig. 3.1. The energy U computed directly is compared to the energy computed from the link overlap $U(q_4)$. The data for both quantities approach a limiting value from opposite directions. Once $U = U(q_4)$, the data for q^2 (shifted for better viewing in Fig. 3.1) are also in thermal equilibrium. The simulation parameters are shown in Table 3.1.

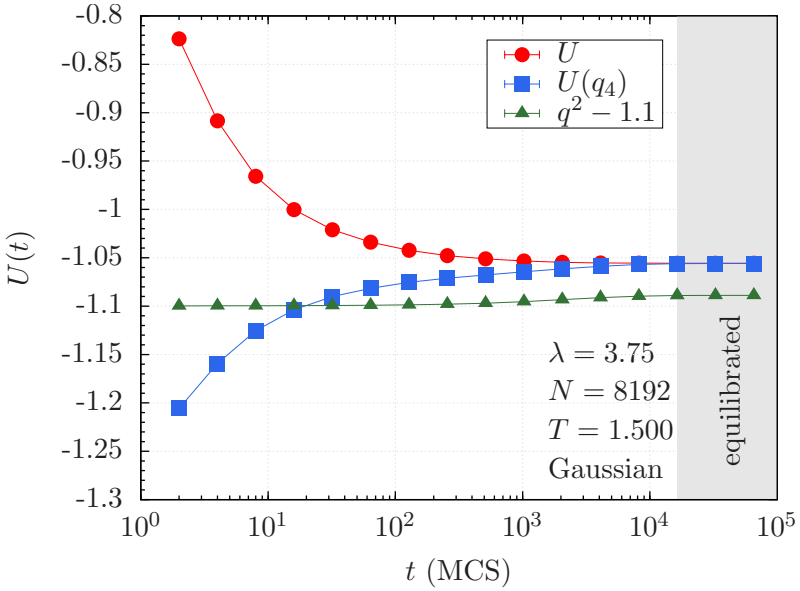

Figure 3.1: Equilibration test for $N = 8192$ spins at $T = 1.500$ (lowest temperature simulated) and $\lambda = 3.75$. Once the data for the energy U and the energy computed from q_4 $[U(q_4)]$ agree, the system is in thermal equilibrium (shaded area). At this point data for q^2 are also independent of Monte Carlo time. Note that the data for q^2 are shifted by a constant factor of 1.1 for better comparison. Error bars are smaller than the symbols.

Table 3.1: Parameters of the simulation: For each exponent λ and system size N, we compute $N_{\rm sa}$ disorder or network instances. $N_{\rm sw} = 2^b$ is the total number of Monte Carlo sweeps for each of the $4N_T$ replicas for a single instance, $T_{\rm min}$ [$T_{\rm max}$] is the lowest [highest] temperature simulated, and N_T is the number of temperatures used in the parallel tempering method for each system size N.

λ	H_r	N	$N_{\rm sa}$	b	$T_{\rm min}$	$T_{\rm max}$	N_T
3.75	0.0	2048	9600	16	1.5000	3.0000	30
3.75	0.0	3072	9600	16	1.5000	3.0000	30
3.75	0.0	4096	9600	16	1.5000	3.0000	30
3.75	0.0	6144	9600	16	1.5000	3.0000	30
3.75	0.0	8192	9600	16	1.5000	3.0000	30
3.75	0.1	512	9600	17	0.9000	3.0000	50
3.75	0.1	768	9600	17	0.9000	3.0000	50
3.75	0.1	1024	9600	17	0.9000	3.0000	50
3.75	0.1	1536	9600	18	0.9000	3.0000	50
3.75	0.1	2048	2400	18	0.9000	3.0000	50
3.75	0.2	768	9600	17	0.9000	3.0000	50
3.75	0.2	1024	9600	17	0.9000	3.0000	50
3.75	0.2	1536	9600	18	0.9000	3.0000	50
3.75	0.2	2048	2400	18	0.9000	3.0000	50
3.75	0.2	4096	2400	19	0.9000	3.0000	50
3.75	0.3	256	9600	17	0.9000	3.0000	50
3.75	0.3	512	9600	18	0.9000	3.0000	50
3.75	0.3	1024	9600	18	0.9000	3.0000	50
3.75	0.3	2048	2400	18	0.9000	3.0000	50
3.75	0.4	256	9600	18	0.9000	3.0000	50
3.75	0.4	512	9600	18	0.9000	3.0000	50
3.75	0.4	1024	9600	18	0.9000	3.0000	50
3.75	0.4	2048	2400	18	0.9000	3.0000	50
4.50	0.0	1024	9600	16	1.0000	3.0000	30
4.50	0.0	2048	9600	16	1.0000	3.0000	30
4.50	0.0	4096	9600	16	1.0000	3.0000	30
4.50	0.0	8192	9600	16	1.0000	3.0000	30
4.50	0.1	512	9600	17	0.9000	3.0000	50
4.50	0.1	1024	9600	17	0.9000	3.0000	50
4.50	0.1	2048	9600	18	0.9000	3.0000	50
4.50	0.1	4096	2400	18	0.9000	3.0000	50
4.50	0.2	256	9600	18	0.6000	3.0000	50
4.50	0.2	512	9600	18	0.6000	3.0000	50
4.50	0.2	1024	9600	18	0.6000	3.0000	50
4.50	0.2	2048	2400	19	0.6000	3.0000	50

Table 3.1 continued

λ	H_r	N	$N_{\rm sa}$	b	$T_{\rm min}$	$T_{\rm max}$	N_T
4.50	0.3	64	9600	18	0.3000	3.0000	50
4.50	0.3	128	9600	19	0.3000	3.0000	50
4.50	0.3	256	9600	20	0.3000	3.0000	50
4.50	0.3	512	9600	22	0.3000	3.0000	50
4.50	0.4	90	9600	19	0.3000	3.0000	50
4.50	0.4	128	9600	19	0.3000	3.0000	50
4.50	0.4	180	9600	19	0.3000	3.0000	50
4.50	0.4	256	9600	20	0.3000	3.0000	50

3.2.3 Numerical results for $\lambda = 4.50$

Corrections to scaling are large for this model despite the large system sizes and number of samples studied. As previously stated, we expect that for $\lambda = 4.50$ a spin-glass state is stable towards an external field because for $\lambda > 4$ the system shares the same universality class as the SK model. To determine the AT line, we plot $\chi/N^{1/3}$ versus the inverse temperature $\beta = 1/T$. Because $\chi/N^{1/3}$ is a dimensionless function [see Eq. (3.9)], data for different system sizes should cross at the putative field-dependent transition temperature. To cope with corrections to scaling and obtain a precise estimate of the critical temperature, we study the crossing temperatures $T_c(N, 2N)$ for pairs of system sizes N and $2N$ assuming

$$T_c(N, 2N) = T_c + A/N^{\omega}\,, \tag{3.14}$$

where A is a fitting parameter and empirically $\omega = 1$. An example extrapolation is shown in Fig. 3.2 for $\lambda = 4.50$ and $H_r = 0.1$. A linear fit is very stable and the extrapolation to the thermodynamic limit clear. Statistical error bars are determined via a bootstrap analysis [95] using the following procedure: For each system

size N and N_{sa} disorder realizations, a randomly selected bootstrap sample of N_{sa} disorder realizations is generated. With this random sample, an estimate of $\chi/N^{1/3}$ is computed for each temperature. The crossing temperature for pairs of N and $2N$ is obtained by fitting the data to a third-order polynomial and a subsequent root determination. We repeat this procedure $N_{\mathrm{boot}} = 500$ times for each lattice size and then assemble N_{boot} complete data sets (each having results for every system size N) by combining the ith bootstrap sample for each size for $i = 1, \ldots, N_{\mathrm{boot}}$. The non-linear fit to Eq. (3.14) is then carried out on each of these N_{boot} sets, thus obtaining N_{boot} estimates of the fit parameters T_c and A. Because the bootstrap sampling is done with respect to the disorder realizations which are statistically independent, we can use a conventional bootstrap analysis to estimate statistical error bars on the fit parameters. These are comparable to the standard deviation among the N_{boot} bootstrap estimates.

The obtained estimates of T_c are listed in Table 3.2. Figure 3.3 shows the field–temperature phase diagram for $\lambda = 4.50$. The shaded area is intended as a guide to the eye. The critical line separates a paramagnetic (PM) from a spin-glass (SG) phase. The dotted (blue) line represents the AT line computed analytically (appendix A) in the limit of $H_r \to 0$. For $4 < \lambda < 5$ the shape of the AT line is given by Eq. (A.17). The analytical approximation fits the data for $\lambda = 4.5$ very well with $H_r(T) \sim C_{4.5}(1 - T/T_c)^{5/4}$ and $C_{4.5} = 0.48(3)$.

3.2.4 Numerical results for $\lambda = 3.75$

Because for $\lambda < 4$ we are no longer in the SK universality class, it is *a priori* unclear if a spin-glass state in a field will exist. Furthermore, when $\lambda = 3.75$, a finite-size scaling according to Eq. (3.7) has to be performed. Because it is not possible to define a distance metric on a scale-free network, there is no notion of a

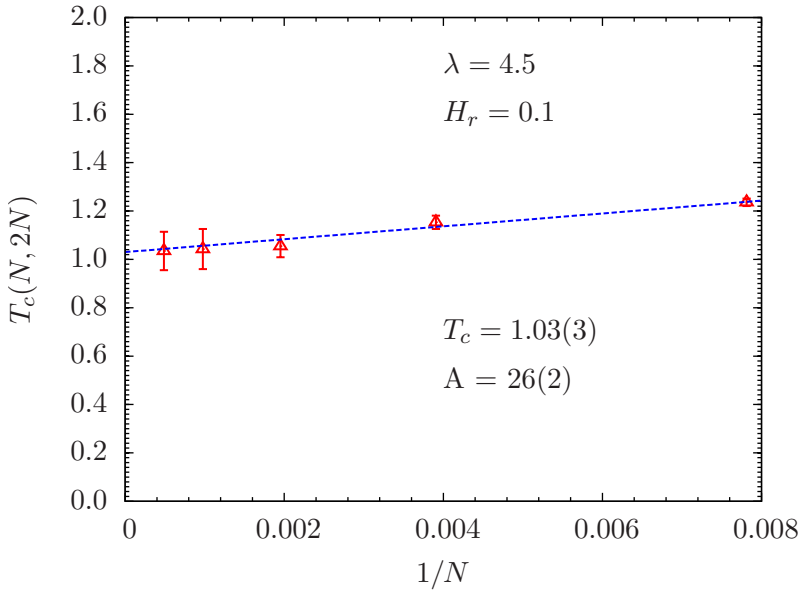

Figure 3.2: Extrapolation to the thermodynamic limit for the critical temperature T_c for $\lambda = 4.50$ and $H_r = 0.1$. We determine the crossing points of critical temperatures of the susceptibility expression for pairs of system sizes N and $2N$. Using Eq. (3.14) with $\omega = 1$ we extrapolate the data to the thermodynamic limit. This allows us to take into account corrections to scaling in an unbiased way.

correlation length or spin-spin correlation function. As such, the critical exponents ν (that describes the divergence of the correlation length) and η (also known as the anomalous dimension) have to be treated carefully. However, we will assume that Eq. (3.7) is valid in this regime on generic finite-size scaling grounds and treat ν and η as parameters when $H_r > 0$ with no special meaning attached to them. In addition, we fix $\nu = 11/3$ and $\eta = 2 - 1/\nu$ — the zero-field values of the critical exponents — and scale the data at finite fields assuming these exponents are valid also when $H_r > 0$.

To determine $T_c(H_r)$, we perform a finite-size scaling analysis of the susceptibility data according to Eq. (3.7). To determine the optimal value of $T_c = 1/\beta_c$ that scales the data best we use the approach developed in Ref. [95]. We assume that

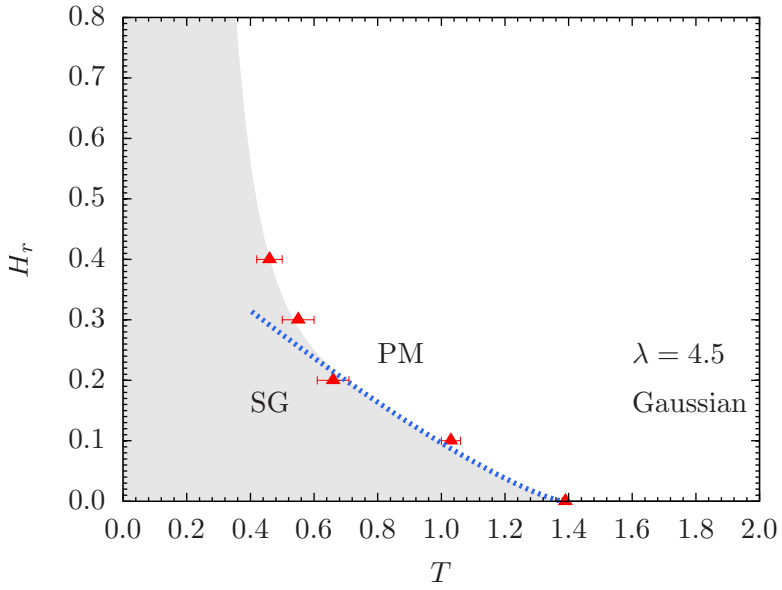

Figure 3.3: Field H_r versus temperature T phase diagram for an Ising spin glass on a scale-free graph with $\lambda = 4.50$. The data points separate a paramagnetic (PM) from a spin-glass (SG) state. The shaded area is intended as a guide to the eye. The dotted (blue) line is a calculation of the AT line in the $H_r \to 0$ limit.

the scaling function in Eq. (3.7) can be represented by a third-order polynomial $y(x) = c_0 + c_1 x + c_2 x^2 + c_3 x^3$ for $|x| \lesssim 1$ and do a global fit to the seven parameters c_i with $i \in \{0, \ldots, 3\}$, β_c, η, and ν. Here $y = \chi / N^{2-\eta}$ and $x = N^{1/\nu}[\beta - \beta_c]$. After performing a Levenberg-Marquardt minimization combined with a bootstrap analysis we determine the optimal critical parameters with an unbiased statistical error bar.

Figure 3.4 shows two representative scaling collapses at zero and nonzero field values. The data scale well and allow one to determine the critical temperature with good precision despite the difficulties that scaling the spin-glass susceptibility poses [95]. Note that for zero field we obtain $\eta = 1.72(1)$ and $\nu = 3.56(17)$, which agree very well with the analytical expressions $\eta = 19/11 = 1.72\ldots$ and $\nu = 11/3 = 3.66\ldots$. However, for finite fields deviations are visible. A summary of the relevant fitting

Table 3.2: Critical parameters T_c, ν, and η for a spin glass with Gaussian random bonds defined on a scale-free graph. The data for $\lambda = 4.50$ have been determined using the mean-field finite-size scaling expression in Eq. (3.9). In this case one can, in principle, define $\eta = 5/3$ and $\nu = 3$, although these should be viewed as parameters placed in Eq. (3.7) to obtain Eq. (3.9). For $\lambda = 3.75$ we determine the critical parameters using Eq. (3.7). The starred estimates of T_c for $H_r > 0$ have been determined by using the zero-field estimates of $\eta = 19/11$ and $\nu = 11/3$ as fixed. Both T_c and $T_c^\star$ agree within error bars, except statistical fluctuations are smaller for $T_c^\star$ because there are fewer fitting parameters.

λ	H_r	T_c	$T_c^\star$	ν	η
3.75	0.0	1.98(2)	1.97(1)	3.56(17)	1.72(1)
3.75	0.1	1.67(5)	1.68(3)	4.42(73)	1.70(3)
3.75	0.2	1.32(8)	1.39(5)	6.53(61)	1.72(2)
3.75	0.3	1.20(6)	1.16(4)	3.31(32)	1.74(2)
3.75	0.4	0.97(7)	1.00(4)	3.68(46)	1.72(2)
4.50	0.0	1.39(1)		3	5/3
4.50	0.1	1.03(3)		3	5/3
4.50	0.2	0.66(5)		3	5/3
4.50	0.3	0.55(5)		3	5/3
4.50	0.4	0.46(4)		3	5/3

parameters is listed in Table 3.2. Note that the value of η for different fields agrees within error bars. However, fluctuations are larger for ν. One can expect that the universality class of the system does not change along the AT line [14]. Therefore, and because it is hard to simulate large systems for large fields, we also determine T_c by fixing $\eta = 19/11$ and $\nu = 11/3$. As listed in Table 3.2, both estimates agree within error bars. This is also visible in Fig. 3.5 which shows the AT line for $\lambda = 3.75$. Overall, the analysis using the zero-field estimates for η and ν gives more accurate results. The dotted (blue) line in Fig. 3.5 is our analytical estimate of the AT line computed in the $H_r \to 0$ limit (appendix A). The estimate fits the data well with $H_r(T) \sim C_{3.75}(1 - T/T_c)^{7/6}$ and $C_{3.75} = 0.76(5)$.

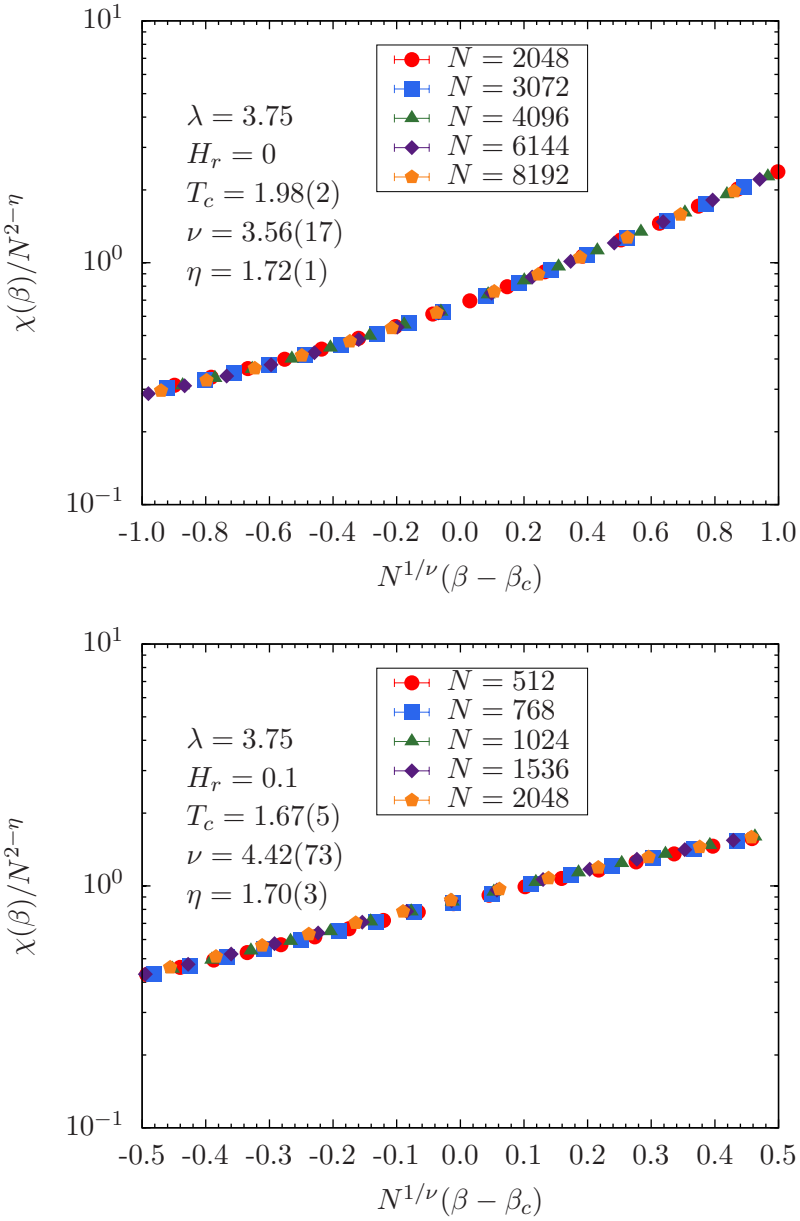

Figure 3.4: Finite-size scaling analysis of $\chi/N^{2-\eta}$ as a function of $N^{1/\nu}(\beta - \beta_c)$ for an Ising spin glass on a scale-free network with Gaussian disorder and $\lambda = 3.75$. The data at zero field (top panel) scale very well. The bottom panel shows representative data for $H_r = 0.1$ scaled according to Eq. (3.7). Error bars are smaller than the symbols.

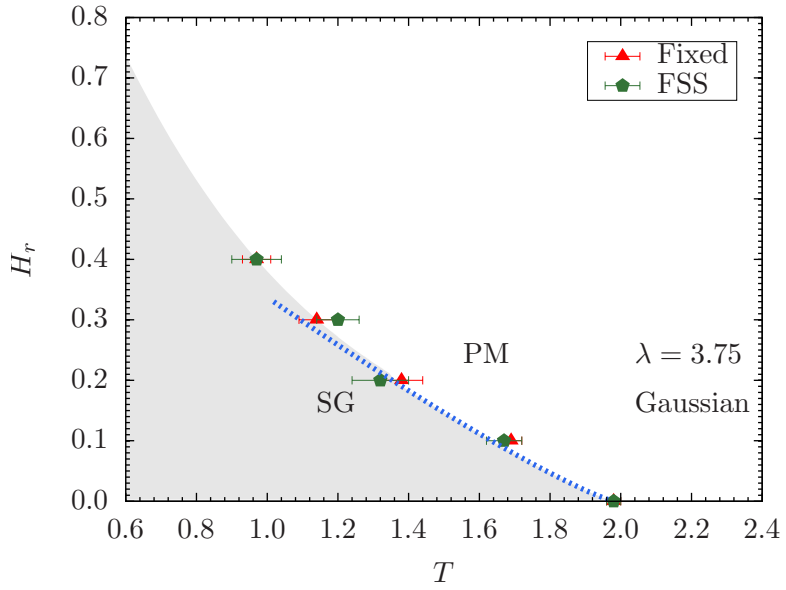

Figure 3.5: Field H_r versus temperature T phase diagram for an Ising spin glass on a scale-free graph with $\lambda = 3.75$. The data points separate a paramagnetic (PM) from a spin-glass (SG) state. The shaded area is intended as a guide to the eye. The dotted (blue) line is a calculation of the AT line in the $H_r \to 0$ limit. Note that estimates for the critical temperature T_c from a finite-size scaling analysis (FSS) according to Eq. (3.7) with T_c, η, and ν as free parameters agree within error bars with estimates at finite fields where $\eta = 19/11$ and $\nu = 11/3$ are used as fixed parameters (labeled with "Fixed" in the plot).

3.3 Nonequilibrium properties in a field

It has recently been shown that a key ingredient for the existence of SOC in glassy spin systems is a diverging number of neighbors [76]. Scale-free networks have a power-law degree distribution. If the exponent $\lambda \leq 2$, then scale-free networks have an average number of neighbors K that diverges with the system size. Therefore, it is possible that SOC might be present in this regime. To test this prediction, in this section we compute nonequilibrium avalanche distributions of spin flips driven by an external field.

3.3.1 Numerical details and measured observables

We study the Hamiltonian in Eq. (3.2) either with Gaussian [Eq. (3.4)] or bimodal [Eq. (3.5)] disorder. The external magnetic field used to drive the avalanches is uniform rather than drawn from a Gaussian distribution, i.e., $H_i = H$ in Eq. (3.2). Spin-flip avalanches are triggered by using zero-temperature Glauber dynamics [77, 79, 96, 76]. In this approach one computes the local fields

$$h_i = \sum_j J_{ij} S_j - H \tag{3.15}$$

felt by each spin. A spin is unstable if the stability $h_i S_i < 0$ is negative. The initial field H is selected to be larger than the largest local field, i.e., $H > |h_i| \ \forall i$. Furthermore, we set all spins $S_i = +1$. The spins are then sorted by local fields and the field H reduced until the stability of the first sorted spin is negative, therefore making the spin unstable. This (unstable) spin is flipped, then the local fields of all other spins updated, and the most unstable spin is flipped again until all spins are stable, i.e., the avalanche ends. Simulation parameters are shown in Table 3.3.

We measure the number of spins that flipped until the system regains equilibrium and record the avalanche size distributions $D(n)$ for all triggered avalanches of size n until $S_i \to -S_i \ \forall i$. When SOC is present (as for the SK model), we expect the avalanche distributions to be power-law distributed with an exponential cutoff that sets in at a characteristic size n^*. Only if $n^*(N) \to \infty$ for $N \to \infty$ without tuning any parameters does the system exhibit true SOC. n^* is determined by fitting the tail of the distributions to $D(n) \sim \exp[-n/n^*(N)]$ with $n^*(N)$ a fitting parameter. This procedure is repeated for different values of λ and the thermodynamic value of $n*$ is determined by an extrapolation in the system size N.

Table 3.3: Simulation parameters in the nonequilibrium study with both Gaussian and bimodal-distributed random bonds: For each exponent λ we study systems of $N = 500 \times 2^m$ spins with $m \in \{1, \ldots, m_{\max}\}$. For Gaussian disorder, when $\lambda < 4$, we also simulate systems with 48 000 spins ($m = 6$ corresponds to 32 000 spins). All distributions are computed using N_{sa} disorder realizations.

disorder type	λ	$m_{\max}$	N_{sa}
Gaussian	1.50	6	12 000
Gaussian	2.00	6	12 000
Gaussian	2.50	6	12 000
Gaussian	3.00	6	12 000
Gaussian	3.50	6	12 000
Gaussian	4.00	5	12 000
Gaussian	4.50	5	12 000
Gaussian	5.00	5	12 000
Gaussian	5.50	5	12 000
Gaussian	6.00	4	12 000
Gaussian	6.50	4	12 000
Gaussian	7.00	4	12 000
Bimodal	1.50	6	12 000
Bimodal	2.00	6	12 000
Bimodal	2.25	6	12 000
Bimodal	2.50	6	12 000
Bimodal	3.00	6	12 000
Bimodal	3.50	6	12 000
Bimodal	4.00	6	12 000
Bimodal	4.50	5	12 000
Bimodal	5.00	5	12 000

3.3.2 Numerical results for Gaussian disorder

We start by showing avalanche distributions for selected values of the exponent λ which show the characteristic behavior of the system.

Figure 3.6 (top panel) shows avalanche distributions $D(n)$ for $\lambda = 4.50$ recorded across the whole hysteresis loop (bottom panel). Here, the number of neighbors does not diverge with the system size because $\lambda = 4.50 > 2$. The distributions show no system size dependence. The fact that the data show a curvature in a log-log plot clearly indicate that these are not power laws. Although tens of thousands of spins are simulated, the largest avalanches found span less than 1% of the system. The vertical line represents the extrapolated typical avalanche size n^* which is rather small and indicates that the system is not in an SOC state.

In contrast, Fig. 3.7, top panel, shows data for $\lambda = 1.5 < 2$ in the regime where the number of neighbors diverges with the system size. The distributions $D(N)$ have a clearly visible power-law behavior with a crossover size $n^*(N)$ that grows with increasing system size. Furthermore, a careful extrapolation to the thermodynamic limit shows that $1/n^* = -0.0012(23)$, i.e., $n^* = \infty$. The hysteresis loop shown in the bottom panel of Fig. 3.7 suggests that for this value of λ larger rearrangements of spins are possible.

We have repeated these simulations for several values of the exponent λ. Our results are summarized in Fig. 3.8, where $1/n^*$ is plotted as a function of λ. Clearly, $1/n^* = 0$ only if $\lambda \leq 2$, i.e., in the regime where the number of neighbors diverges, in perfect agreement with the results of Ref. [76] for hypercubic systems, as well as the SK model [35]. Note that we have also recorded distributions of magnetization jumps (not shown) [35, 76] that qualitatively display the same behavior as the avalanche size distributions.

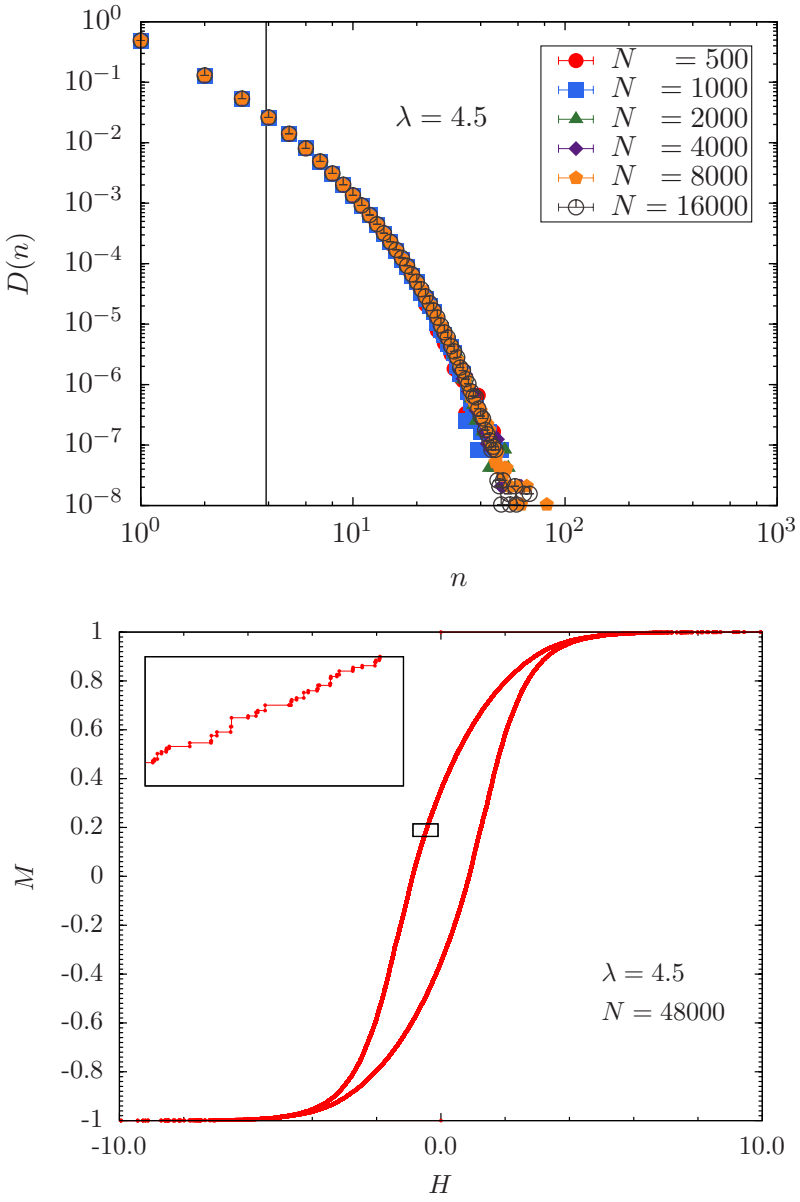

Figure 3.6: Top: Avalanche distribution $D(n)$ for the Edwards-Anderson spin-glass model with Gaussian disorder on scale-free networks with $\lambda = 4.50$ recorded across the whole hysteresis loop. The data show no system size dependence. The vertical (black) line marks the extrapolated value of n^*. Clearly, no signs of SOC are visible in the data. Bottom: Magnetization $M = (1/N)\sum_i s_i$ versus field H hysteresis loop for $\lambda = 4.50$ and 48000 spins. The data are for one single sample and meant as an illustration for the typical behavior of the system in a field. The inset shows a zoom into the boxed region. The discrete steps due to magnetization jumps in the hysteresis loop are clearly visible.

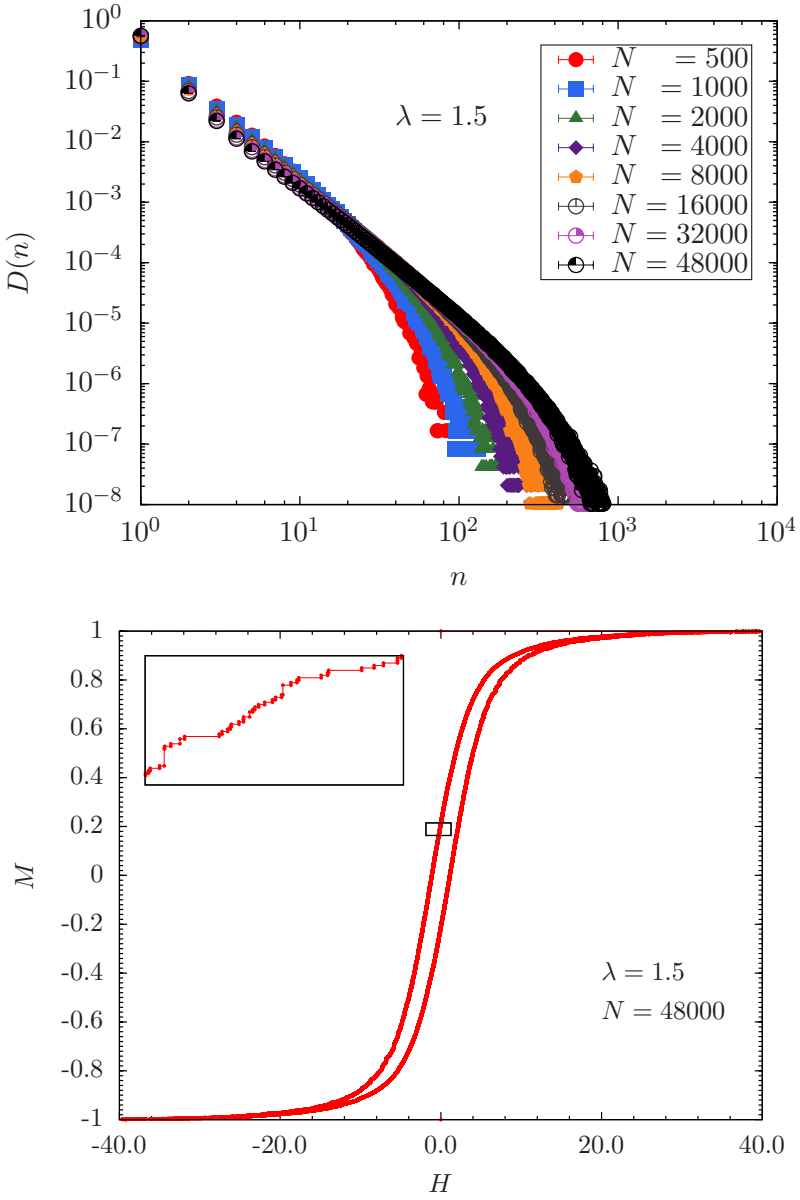

Figure 3.7: Top: Avalanche distribution $D(n)$ for the Edwards-Anderson spin-glass model with Gaussian disorder on scale-free networks with $\lambda = 1.5$ recorded across the whole hysteresis loop. For $\lambda = 1.5 < 2.0$ the number of neighbors diverges. The data show a clear system-size dependence with the distributions becoming increasingly power-law-like for increasing system size N. As shown in Fig. 3.8, the extrapolated cutoff value is $n^* = \infty$, i.e., the system exhibits true SOC behavior. Bottom: Magnetization $M = (1/N)\sum_i s_i$ versus field H hysteresis loop for $\lambda = 1.50$ and 48000 spins. The data are for one single sample and meant as an illustration for the typical behavior of the system in a field. The inset shows a zoom into the boxed region. The discrete steps due to magnetization jumps in the hysteresis loop are clearly visible. Qualitatively, the data seem to show larger rearrangements as for $\lambda = 4.50$ (Fig. 3.6).

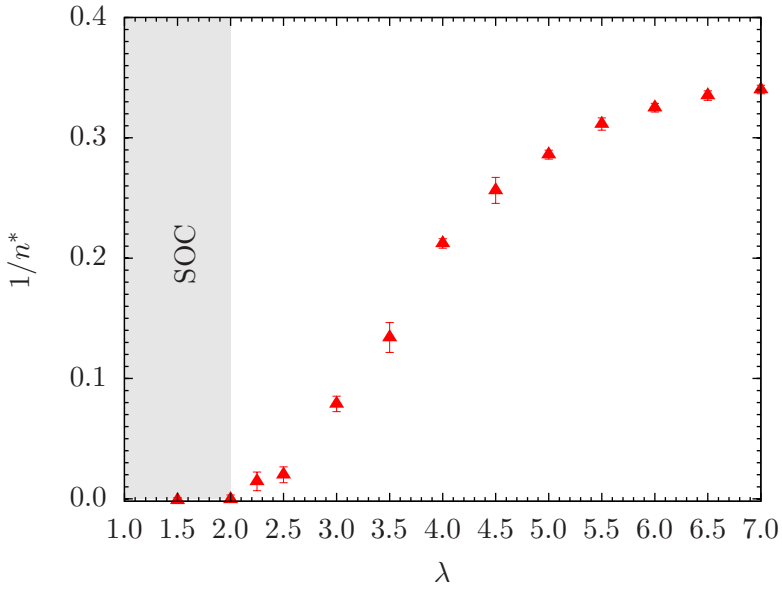

Figure 3.8: Characteristic avalanche size n^* extrapolated to the thermodynamic limit for different values of λ and Gaussian disorder. Plotted are $1/n^*$ versus λ. Only when $1/n^* = 0$ (here within error bars) we can expect the system to show SOC behavior. This is only the case for $\lambda \leq 2$, i.e., in the regime where the number of neighbors diverges.

3.3.3 Numerical results for bimodal disorder

So far, we have only probed for the existence of SOC within the spin-glass phase. Bimodal disorder [Eq. (3.5)] has the advantage that one can easily tune the fraction of ferromagnetic bonds by changing p. When $p = 1$ the system is a pure ferromagnet, whereas for $p = 0$ it is an antiferromagnet and for $p = 0.5$ a spin glass (comparable to the Gaussian case).

Sethna *et al.*, as well as others, have studied the random-field Ising model [97, 77, 82, 78, 79, 80, 81] where the level of ferromagnetic behavior is tuned by changing the width of the random-field distribution σ. In particular, for three space dimensions, there is a critical value σ_c where a jump in the hysteresis loop appears, i.e., large system-spanning rearrangements of the spins start to occur when $\sigma > \sigma_c$. We call this

regime *supercritical* because here system-spanning avalanches will always occur in a predominant fashion. For $\sigma = \sigma_c$ true power-law distributions of the spin avalanches are obtained, whereas for $\sigma < \sigma_c$ no system-spanning rearrangements are found. We call the latter scenario *subcritical*.

Here we find a similar behavior when tuning the fraction of ferromagnetic bonds p. Figure 3.9 shows the typical behavior we observe for the avalanche distributions $D(n)$. For $p = 0.63$ and $\lambda = 3.50$ (Fig. 3.9, top panel), the distributions show small system-size dependence. A detailed analysis of the characteristic avalanche size $n^*(N)$ shows that it extrapolates to a finite value in the thermodynamic limit.

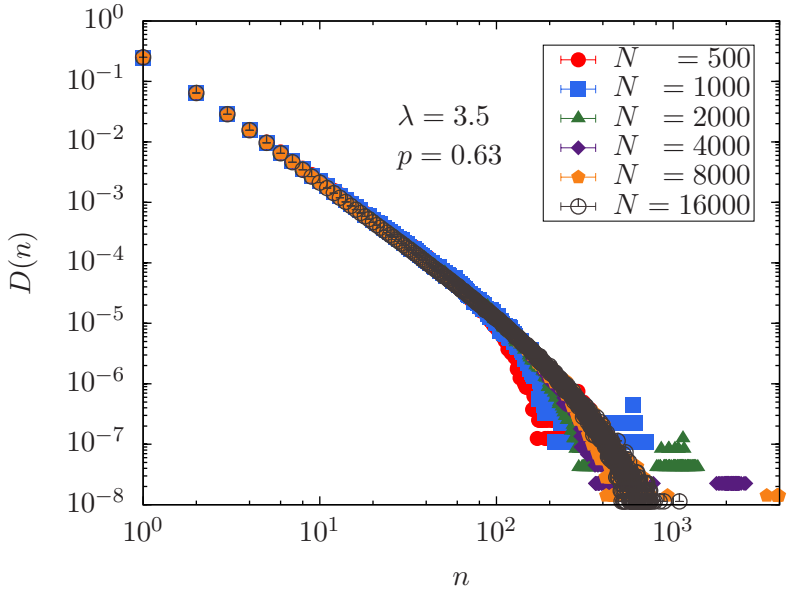

Figure 3.9: Avalanche distribution $D(n)$ for the Edwards-Anderson spin-glass model with bimodal disorder on scale-free networks with $\lambda = 3.5$ recorded across the whole hysteresis loop. Top panel: Data for $p = 0.63 < p_c$. Here the system displays subcritical behavior, i.e., the characteristic avalanche size n^* is finite. Center panel: For $p = 0.66 \approx p_c$ the system is in the critical regime where the distributions are well described by power laws. Bottom panel: For $p = 0.70 > p_c$ the system is in the supercritical regime. A jump in the hysteresis loop occurs, i.e., very large rearrangements are very probable, as can be seen in the bump that develops in the distributions $D(n)$ for large n.

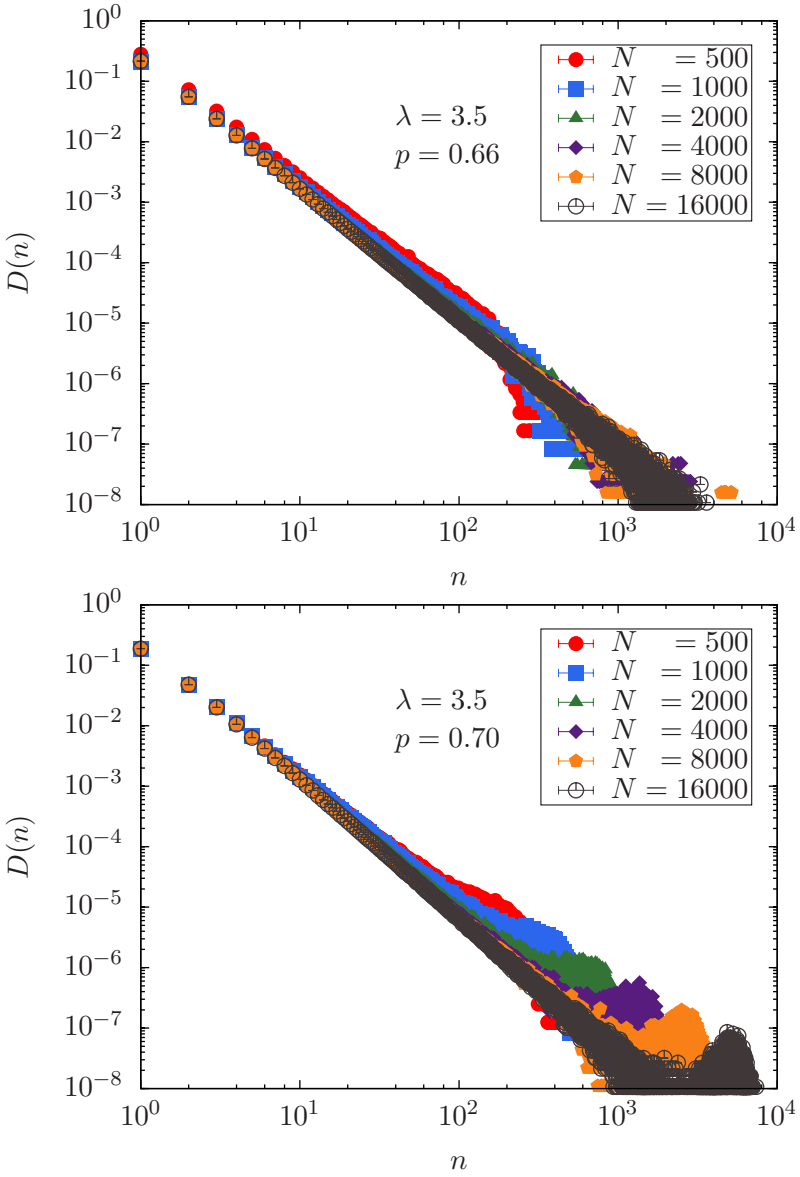

Figure 3.9 continued

This means we are in the subcritical regime. However, for $\lambda = 3.50$ and $p = 0.66$ clear power laws in the distributions $D(n)$ emerge (Fig. 3.9, center panel). Here $n^* \to \infty$, i.e., true power-law behavior. However, for $\lambda = 3.50$ and $p = 0.70$, although most of the distributions show a clear power-law-like behavior, a bump for large n appears (Fig. 3.9, bottom panel). In this case the probability for very large rearrangements

increases. Direct inspection of the underlying hysteresis loops (not shown) shows a jump in the magnetization, i.e., we are in the supercritical regime. We repeat these simulations for different exponents λ and vary the fraction of ferromagnetic bonds p until the distributions are power laws. This allows us to construct the phase diagram shown in Fig. 3.10. We find a critical line $p_c(\lambda)$ (triangles, solid curve) that separates the subcritical region from the supercritical region. Along the critical line avalanche size distributions are power laws. Note that this critical line shows no close correlations with the spin-glass–to–ferromagnetic boundary computed in Ref. [2] (dotted line in Fig. 3.10). For $\lambda \leq 2$ and when $p = 0.5$, i.e., within the spin-glass phase where the graph connectivity diverges, we recover true SOC.

3.4 Summary and conclusions

We have studied Boolean (Ising) variables on a scale-free graph with competing interactions in an external field both in thermal equilibrium, as well as in a nonequilibrium hysteretic setting.

At finite temperatures, we show that for $\lambda > 3$, where at zero field the system orders at finite temperatures [2], spin glasses on scale-free graphs do order in a field, i.e., their behavior is very much reminiscent of the mean-field SK model in a field. Naively, one could have expected that outside the SK regime ($\lambda < 4$) a behavior reminiscent of (diluted) one-dimensional spin glasses with power-law interactions [98, 99, 100] emerges where a spin-glass state in a field seems stable only within the mean-field regime of the model [89, 84]. These results again illustrate the superb robustness of Boolean decision problems on scale-free networks to perturbations. In this case, a stable spin-glass state emerges at nonzero temperatures even in the presence of magnetic fields (external global biases).

At zero temperature, when driven with an external field, Boolean decision prob-

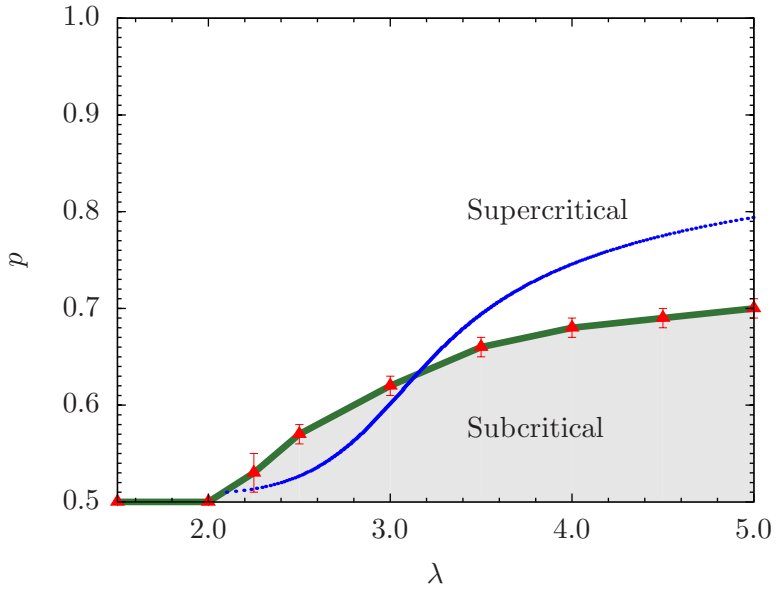

Figure 3.10: Fraction of ferromagnetic bonds p versus λ phase diagram for the Edwards-Anderson spin-glass model on scale free networks with bimodal interactions between the spins. For $\lambda > 2$ a critical line $p_c(\lambda)$ separates the subcritical regime where avalanches are small, from the supercritical regime where system-spanning avalanches are very common. Along the critical line $p_c(\lambda)$ (triangles, solid line) avalanche sizes are distributed according to power laws. For $\lambda \leq 2$ the number of neighbors diverges. In this regime for $p = 0.5$ the system displays avalanches that are power laws, i.e., true SOC. The dotted line represents the spin-glass–to–ferromagnetic phase boundary from Fig. 2 in Ref. [2].

lems on scale-free networks show self-organized critical behavior only when the number of neighbors diverges with the system size, i.e., for $\lambda \leq 2$. For $\lambda > 2$ and with bimodal disorder, a behavior reminiscent of the random-field Ising model is found [77, 82, 78, 79, 80, 81] where system-spanning avalanches only occur whenever the fraction of ferromagnetic bonds $p_c(\lambda)$ is tuned towards a critical value. These results show that "damage" can easily spread on real networks where typically $\lambda \lesssim 3$. Therefore, in contrast the robustness found at finite temperatures, Boolean decision problems on scale-free networks show a potential fragility when driven in a nonequilibrium scenario at zero temperature. Our results agree with the conclusions in Ref.

[76] that SOC is not necessarily a property of the mean-field regime but is instead a result of a diverging number of neighbors z.

4. BEST-CASE PERFORMANCE OF QUANTUM ANNEALERS ON NATIVE SPIN-GLASS BENCHMARKS: HOW CHAOS CAN AFFECT SUCCESS PROBABILITIES

Although a useful universal quantum computer [101, 40] is far from reality at the moment, the advent of quantum annealing (QA) machines based on quantum adiabatic optimization techniques [102, 103, 104, 105, 106, 63, 107, 108, 109, 110, 111, 112] has sparked a small computing revolution in recent years. Being the first novel hardware based on non-silicon chips used to perform computations exploiting the potential advantages of quantum fluctuations [113], quantum annealing machines might affect the way a multitude of hard optimization problems are solved today.

The first somewhat useful programmable commercial device that attempts to exploit this unique power are the D-Wave One and Two quantum annealers [114], that are designed to solve quadratic unconstrained binary optimization (QUBO) problems [115], such as finding the ground state of a disordered Ising spin-glass Hamiltonian, a well-known NP-hard problem in this general formulation [64]. Because many problems across disciplines can be mapped onto QUBOs, multiple studies of the D-Wave quantum annealer's performance, compared to some classical optimization approaches, such as simulated annealing (SA) [36], have been performed [37, 116, 117, 118, 119, 120, 38, 121, 122, 123, 124]. Tests [116, 117, 119, 121] by different research teams suggest that the D-Wave quantum annealer does benefit from quantum effects. However, it is unclear if this quantum advantage is involved in the optimization of cost functions. Furthermore, to date these studies reveal no clear evidence of limited quantum speedup [38] over classical optimization algorithms on traditional computers.

Recent work by Katzgraber *et al.* [3] suggests that current benchmarking approaches using spin glasses with uniformly-distributed disorder on the Chimera graph [125], such as bimodal or range-k, might not be the best benchmark problems in the quest for quantum speedup. In particular, Ref. [126] proposes an innovative approach based on insights from the study of spin glasses to design hard benchmark problems *within* the constraints of the D-Wave device. To overcome the limitations posed by the D-Wave architecture, Ref. [126] proposes to use instances with a unique ground state, as well as many metastable states. In this chapter I study the interplay between the generation of hard benchmark instances with the design of problems suitable for the D-Wave device that are robust to noise. Ideally, thus, a two-tier (unfortunately computationally-expensive) data mining approach is needed to produce ideal test instances for any quantum annealing device: First, random benchmark instances are mined for their desired properties (e.g., unique ground state) that make them hard problems to solve. Second, these instances are tested for their robustness to the intrinsic noise present in any hardware device.

The fact that different numerical studies [107, 108, 111, 127] demonstrated that QA might outperform SA in certain problems—especially those with rough energy landscapes—has motivated the authors of Refs. [126] and [128] to design tunable hard benchmarking problems. Reference [126] goes a step further, by being able to carefully tune the barrier thickness between dominant features in the energy landscape, thus putatively allowing for the detection of any quantum advantage that a quantum annealing device might pose over traditional optimization approaches. Despite these efforts, noise due to thermal excitations and control errors on qubits and couplers have a detrimental effect on the performance of the D-Wave quantum annealer [129, 130, 118, 131, 132] that likely is masking any potential limited quantum speedup [38]. A simple explanation for these problems is given by

the fragility of spin glasses to small perturbations, also known as chaotic effects [133, 134, 135, 136, 137, 138, 139, 140, 141, 142] to either couplers (bond chaos), qubits via longitudinal fields (field chaos), or both couplers and qubits (temperature chaos). Here, small fluctuations can produce large changes in the free energy of the system thus perturbing the original problem Hamiltonian to be solved.

Although quantum error correction [118, 131, 132] can, in principle, mitigate these errors, it does so at a cost of needing multiple physical qubits to encode one logical qubit, thus reducing the effective system size of problems to be studied. This also means that "error-corrected" benchmark instances, while more robust to noise, will likely be too small to be in the scaling regime of interest. As such, designing hard benchmark instances that are robust to noise and require no overhead in the embedding to keep the problem size at a maximum are of utmost importance to detect quantum speedup. In this chapter I classically study *resilience*, i.e., the probability that the ground-state configuration is not affected by random fields and random-bond fluctuations found on the chip for different benchmark instance classes, by using realistic uncorrelated noise models for the D-Wave Two quantum annealer. Furthermore, I present strategies on how to develop hard benchmark instances that, at the same time, are robust to noise. Note that our methodology is generic, i.e., it can be applied to any architecture.

This chapter is structured as follows. In Sec. 4.1 I introduce the different benchmark instance classes studied, as well as the noise model. Furthermore, I describe the heuristic used to find the ground-state configurations. Our numerical results on the D-Wave chimera topology are presented in Sec. 4.2, followed by concluding remarks.

4.1 Model, observables and algorithm

Our calculations are for the currently-available D-Wave Two device. However, the ideas can be generalized to any topology.

4.1.1 Model

The *native* benchmark for the D-Wave Two quantum annealer is an Ising spin glass [14, 40, 143] defined on the Chimera topology of the system [125]. The Hamiltonian of the problem to be optimized is given by

$$\mathcal{H} = -\sum_{\{i,j\}\in\mathcal{V}} J_{ij} s_i s_j - \sum_{i\in\mathcal{V}} s_i h_i \,, \tag{4.1}$$

where $s_i \in \{\pm 1\}$ signify Ising spins on the vertices $\mathcal{V}$ of the Chimera lattice. Figure 4.1 shows a 512 qubit Chimera lattice with 8×8 $\mathrm{K}_{4,4}$ cells. In addition, each spin s_i is coupled to a local random field h_i. The sum is over all edges $\mathcal{E}$ connecting vertices $\{i,j\} \in \mathcal{V}$. The interactions J_{ij} between the spins are drawn from carefully chosen, discrete disorder distributions within the hardware constraints of the D-Wave Two architecture.

To emulate the effects of thermal noise in the device, we perturb the discrete values of the couplers J_{ij} by a random amount ΔJ_{ij} drawn from a Gaussian distribution with zero mean and standard deviation ΔJ. For simplicity, we assume the noise is quenched and uncorrelated. This "white noise" represents a realistic (classical) noise model for coupler fluctuations that is typically used to study the effects of noise in electronic devices, as well as telecommunications. Although the qubit noise in the D-Wave Two device is closer to $1/f$ noise with a "pink" power spectrum, for simplicity we couple the individual qubits to uncorrelated quenched random fields drawn from a Gaussian distribution with zero mean and standard deviation h. We

do not expect this simplification to qualitatively change our results.

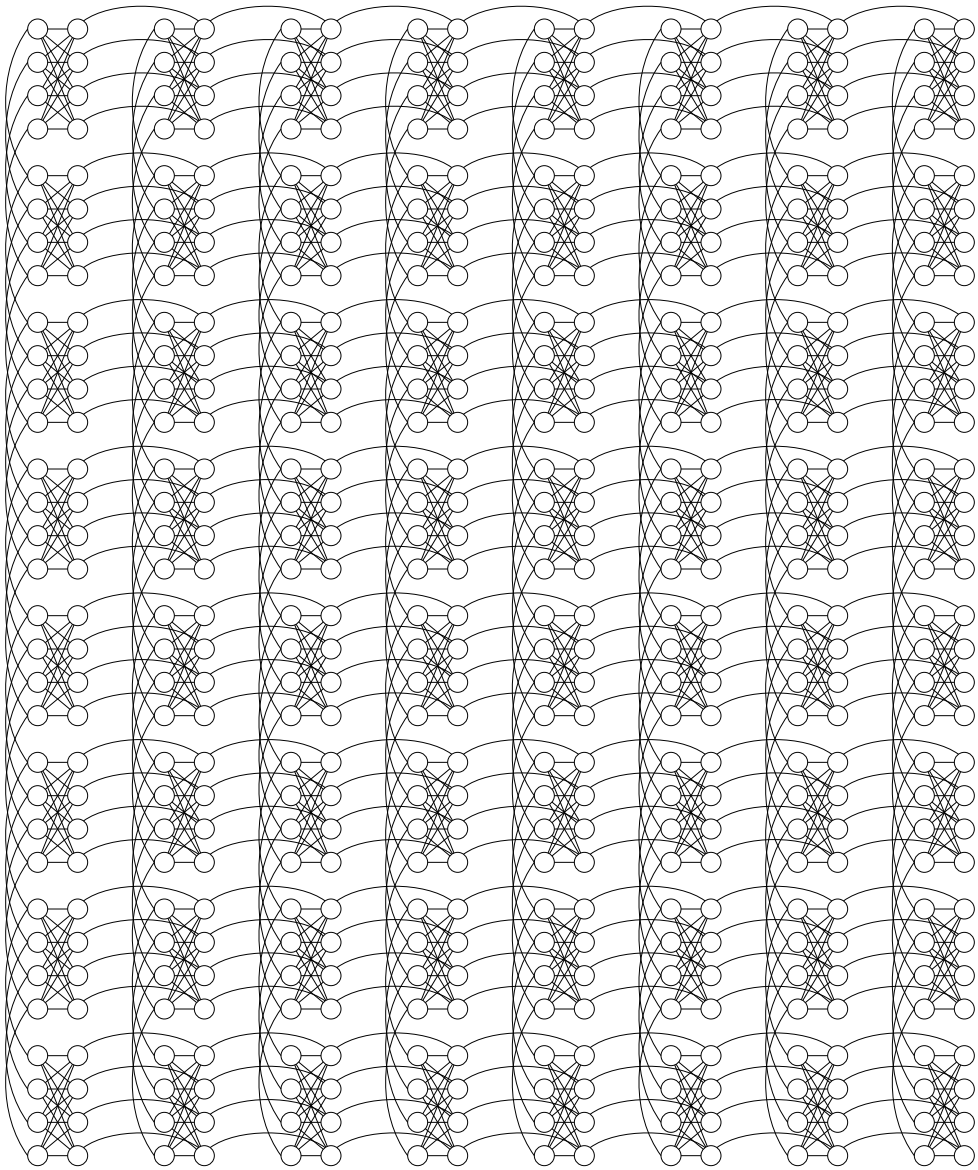

Figure 4.1: Adjacency matrix of the D-Wave Two chip with 8×8 $K_{4,4}$ cells and 512 qubits (circles) connected by couplers (lines).

4.1.2 Instance classes and observables

Carefully-chosen interactions between the spins determine the hardness and robustness of instance classes [126]. To develop hard instances, multiple requirements have to be fulfilled. First, it is of paramount importance to ensure that the instances have a *unique* ground-state configuration that minimizes the cost function in Eq. (4.1). Furthermore, it is desirable to have dominant metastable states such that the system is easily trapped – a process that can be accomplished by a post-processing selection and mining of the data based on insights from the study of the dynamics of spin glasses using classical simulation techniques [144, 126]. Ultimately, an ideal benchmark instance is robust to noise, has a unique ground state and, ideally, many metastable states.

To gauge the fraction of unique ground-state configurations for a particular instance class, we define a quantity we call *yield* ($\mathcal{Y}$), i.e.,

$$\mathcal{Y} = N_{\text{unique}}/N_{\text{total}}. \tag{4.2}$$

In Eq. (4.2) N_{total} is the total number of *randomly-generated* instances for that particular instance class and N_{unique} is the number of instances featuring a unique ground state (no degeneracy).

One simple approach pioneered in Ref. [126] to design instance classes with high yield, is to ensure that as few qubits s_i as possible have zero local fields in Eq. (4.3)

$$\mathcal{F}_i = \sum_{j \neq i} J_{ij} s_j + h_i. \tag{4.3}$$

If for a given qubit $\mathcal{F}_i \equiv 0$, then the qubit's value does not change the energy of the system. Therefore, if a system with N qubits has k free qubits with zero

local field, the degeneracy of the ground state is increased by a factor 2^k. We have exhaustively computed the probability that a particular combination of two, three, or four integer values in the range $[\pm 1, \pm i_{\max}]$ (with $i_{\max} = 28$) [145] for the couplers J_{ij} on the Chimera topology yields the smallest fraction of qubits with zero local fields. Furthermore, we have attempted to "spread out" the integers as much as possible in the range $[-1, 1]$ after a normalization of the coupler values with $i_{\max}$. In addition to the previously-studied cases of bimodal disorder, i.e.,

$$\mathrm{U}_1 \in \{\pm 1\},$$

as well as uniform range-k disorder with $k = 4$ [116, 38]

$$\mathrm{U}_4 \in \{\pm 1, \pm 2, \pm 3, \pm 4\},$$

we also study Sidon-type instances [146, 126], namely

$$\mathrm{U}_{5,6,7} \in \{\pm 5, \pm 6, \pm 7\},$$

which are similar to uniform range-7 instances, however only the three largest integers that form a Sidon set are kept. Finally, we study a larger Sidon set

$$\mathrm{S}_{28} \in \{\pm 8, \pm 13, \pm 19, \pm 28\}.$$

The $\mathrm{U}_{5,6,7}$ and S_{28} Sidon instance classes reduce the probability of zero local fields drastically by design, and thus maximize the yield of unique ground states. In fact, while U_1 has an average probability of 23% (average percentages of local fields being zero) to have zero local fields, this number is reduced to 6% in the U_4 class. $\mathrm{U}_{5,6,7}$ has only 4.5% zero local fields and S_{28} 1.5%.

To increase the resilience of noise for a given instance, one has to maximize the change in energy when flipping a spin, i.e., the minimum classical energy gap. Ideally, this change in energy should be considerably larger than the typical noise fluctuations

to prevent qubit errors. For Ising spins, this energy gap is given by $\Delta E = 2/i_{\max}$, where $i_{\max}$ is the largest integer in the unnormalized bond distribution. For example, $\Delta E(\mathrm{U}_1) = 2$, whereas $\Delta E(\mathrm{U}_4) = 1/2$, $\Delta E(\mathrm{U}_{5,6,7}) = 2/7$, and $\Delta E(\mathrm{S}_{28}) = 1/14 \sim 0.07$. For the current D-Wave Two machine with 512 qubits, coupler fluctuations are typically ~ 0.035 if the bonds are normalized to unity ("auto-scaling mode"). This means that in this case the S_{28} instance class pushes the limits of the machine because $\Delta E(\mathrm{S}_{28}) \sim 2\Delta J$.

To quantify the robustness of ground-state configurations to noise, we define the resilience R of an instance to be

$$R = N_{\mathrm{same}}/N_{\mathrm{trials}} \tag{4.4}$$

where N_{same} is the number of trials with different random noise perturbations that do not change the original ground-state configurations. We perform $N_{\mathrm{trials}} = 10$ trials (or gauges) to compute R. The resilience of an instance class is the resilience for each instance R averaged over disorder, i.e., $\mathcal{R} = [R]_{\mathrm{av}}$, where $[\cdots]_{\mathrm{av}}$ represents an average over multiple random bond configurations. A preference should be given to whole instance classes with high resilience. However, individual instances that are unaffected by the perturbations are also robust instances to noise and can be used for benchmarking purposes. Conversely, to study the effects of noise in quantum annealing machines and how to reduce these, instances with a *small* resilience can also be generated [123].

4.1.3 Algorithm details

In order to measure the yield and resilience of a particular instance class, ground states of instances from all instance classes have to be found. We apply a heuristic method that uses the parallel tempering Monte Carlo algorithm [42] combined with

isoenergetic cluster moves [147] to speed up the thermalization. Simulation parameters are listed in Table 4.1 and thermalization has been determined by a logarithmic binning of the data. Once the last three bins agree within error bars, we deem the system to be in thermal equilibrium. The detailed algorithm to detect ground states was first introduced in Ref. [99]. However, to increase the accuracy of our heuristic, here four instead of two copies of the system with the same disorder are simulated with *independent* Markov chains. We perform N_{SW} updates [148]. For $N_{\mathrm{SW}}/8$ updates we keep track of the lowest energy E of each Markov chain at the lowest temperature simulated. If $E^{(1)} = E^{(2)} = E^{(3)} = E^{(4)}$, it is very likely the ground state energy E_0 has been found. For the remaining number of updates we keep statistics of the configurations that minimize the Hamiltonian and thus estimate the degeneracy distribution of the ground state. However, there is no guarantee that any solution obtained by this heuristic method is the true optimum, or that we have found all configurations that minimize the Hamiltonian. Fortunately, for the Sidon-type instance classes the degeneracy is small by construction. Therefore, it is likely that we found all ground-state configurations. Once the ground-state configurations of all instances have been found, the average yields for different instance classes can be computed.

In addition to the effects of the minimum energy gap ΔE on the resilience for each instance class, we also consider the effects of the number of first excited states on the resilience. To estimate the number of first excited states, for the remaining $(7/8)N_{\mathrm{SW}}$ sampling updates we also keep track of all configurations that have an energy $E_1 = E_0 + \Delta E$.

Table 4.1: Simulation parameters: For each instance class and system size N, we compute N_{sa} instances. $N_{\mathrm{sw}} = 2^b$ is the total number of Monte Carlo sweeps for each of the $4N_T$ replicas for a single instance, T_{min} [T_{max}] is the lowest [highest] temperature simulated, and N_T is the number of temperatures used in the parallel tempering method. For the lowest N_{icm} temperatures isoenergetic cluster moves are applied.

Class	N	N_{sa}	b	T_{min}	T_{max}	N_T	N_{icm}
U_1	512	900	19	0.150	3.050	30	13
U_4	512	900	19	0.150	3.000	30	14
$\mathrm{U}_{5,6,7}$	128	900	19	0.150	3.000	30	14
$\mathrm{U}_{5,6,7}$	288	900	19	0.150	3.000	30	14
$\mathrm{U}_{5,6,7}$	512	900	19	0.150	3.000	30	14
$\mathrm{U}_{5,6,7}$	800	900	19	0.150	3.000	30	14
$\mathrm{U}_{5,6,7}$	1152	900	19	0.150	3.000	30	14
S_{28}	512	900	19	0.150	3.000	30	14

4.2 Results

4.2.1 Yield of non-degenerate ground states

For the current D-Wave Two architecture with 512 qubits, the yield of unique ground states is strongly dependent on the instance class (disorder between spins) used. When the disorder is drawn from a bimodal distribution (U_1) the yield in all our experiments was exactly 0%. Surprisingly, uniform range-4 instances (U_4) also have $\mathcal{Y} = 0\%$. However, by increasing the range of the integers and selecting them from a Sidon set while removing the lowest values gives $\mathcal{Y} = 4.5(4)\%$ for the $\mathrm{U}_{5,6,7}$ class. Although a small fraction, it is clearly nonzero. Finally, for the large Sidon set S_{28} we obtain a fraction $\mathcal{Y} = 20.0(6)\%$ of unique ground states [149], i.e., optimal for large-scale benchmarking.

4.2.2 Resilience to noise

Figure 4.2 shows the resilience to random-field noise for different instance classes. As the typical field strength h increases, the resilience $\mathcal{R}$ for all instance classes decreases. This is expected, because the bandwidth of split states due to increased random-field strength results in more energy levels crossing. Furthermore, for a fixed field strength, instance classes with small energy gaps ΔE tend to have lower resilience. This is to be expected: it is easier for split states to have a lower energy than the original ground state when the gap is small. Note that while instance classes $\mathrm{U}_{5,6,7}$ and U_4 have a similar resilience, the yield of unique ground states is considerably higher for $\mathrm{U}_{5,6,7}$, i.e., a careful design of the spin-spin interactions is key when attempting to benchmark a quantum annealing device.

Figure 4.3 shows the resilience of different instance classes as a function of different typical coupler perturbations ΔJ. Again, for all instance classes studied, the resilience decreases as fluctuations increase. In addition, instance classes with small energy gaps have a lower resilience. It is important to note that bond noise has a stronger impact to the resilience than field noise. Considering each qubit has typically ~ 6 neighbors in the Chimera lattice, the impact of bond noise is amplified by multiple connections of qubits. Therefore, reducing the fluctuations of the couplers is more important than dealing with the intrinsic flux noise of each qubit.

Unfortunately, for the D-Wave architecture, to find an instance class that is both hard and robust to noise, compromise has to be made. The U_1 instance class has the highest resilience to noise, however, the huge ground-state degeneracy makes it easier for classical algorithms such as SA to find minimum-energy configurations [3, 126]. On the flip side, the Sidon instance class is known to be hard [126] and produces many unique ground states, but its resilience is comparably low due to the small energy

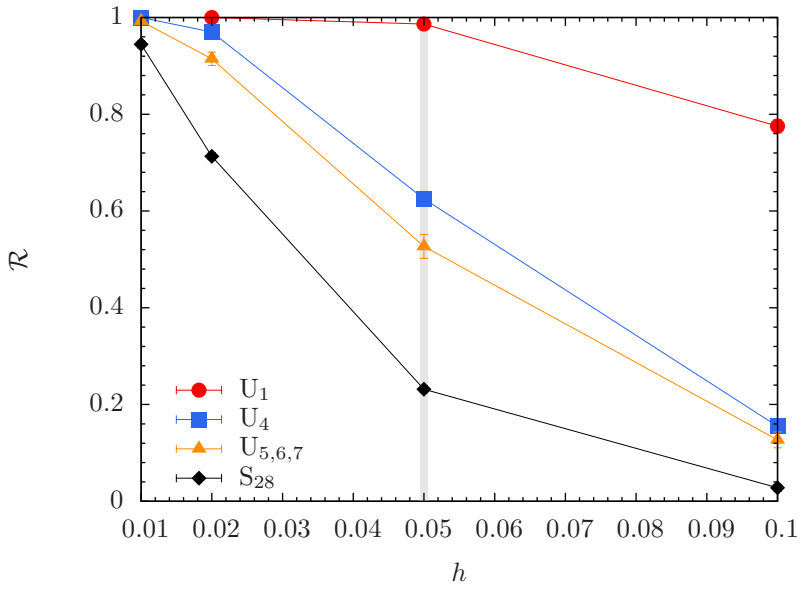

Figure 4.2: Resilience ($\mathcal{R}$) of different instance classes (see text) for a $N = 512$ qubit system on the Chimera graph as a function of Gaussian random field strength (h). Instance classes are less resilient to noise with increasing field strength and decreasing classical energy gap. The shaded line represents the current field noise strength of approximately 5% in the D-Wave Two system.

gap. A compromising natural choice would therefore be to either use the U_4 or $U_{5,6,7}$ instance classes. However, while the resilience for both U_4 and $U_{5,6,7}$ are comparable, the yield of unique ground states needed to construct hard benchmark problems is much higher for $U_{5,6,7}$. We thus conclude that for the current Chimera topology, the $U_{5,6,7}$ instance class is the optimal compromise to design hard benchmark problems within the D-Wave Two architecture constraints. For the remainder of this paper we thus focus on this particular instance class.

Figure 4.4 shows the resilience of the $U_{5,6,7}$ instance class for different system sizes N of the Chimera lattice as a function of the random-bond fluctuation strength ΔJ. Clearly, for increasing system size the resilience $\mathcal{R}$ decreases (larger system sizes typically have a higher degeneracy, therefore level crossings are more common

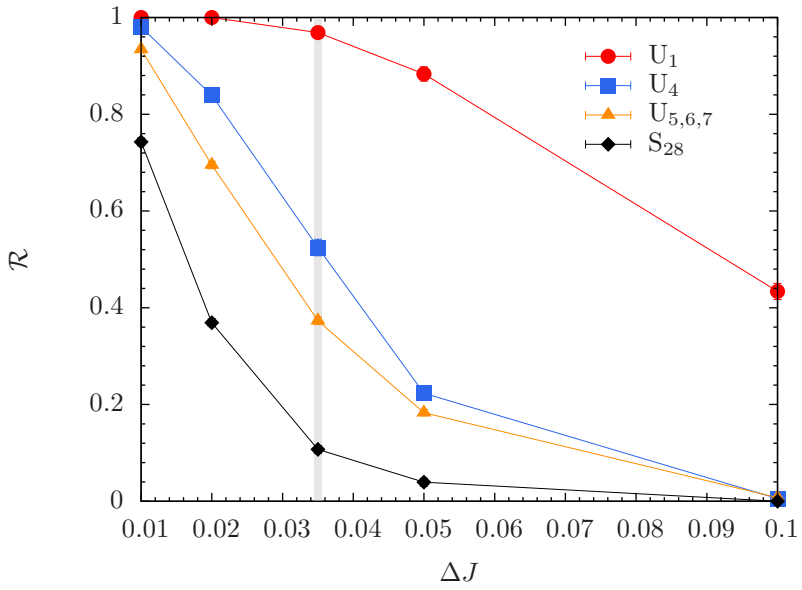

Figure 4.3: Resilience ($\mathcal{R}$) of different instance classes (see text) for a $N = 512$ qubit system on the Chimera graph as a function Gaussian random bond fluctuation strength (ΔJ). Instance classes are less resilient to noise with increasing bond fluctuation strength and a decreasing classical energy gap. The shaded line represents the current bond noise strength in the D-Wave Two system, i.e., $\sim 3.5\%$. Note that bond noise has a stronger effect than field noise (Fig.4.2) on the device.

than with smaller systems). This means that to scale up the system size of the D-Wave Two—or any other quantum annealing device—in the future, a much more precise control over the device's noise is imperative and/or the implementation of error correction schemes [118, 131, 132].

4.2.3 Effects of the number of first excited states

Figure 4.5 shows the resilience $\mathcal{R}$ of the $U_{5,6,7}$ instance class as a function of the degeneracy of the first excited state on the Chimera topology with $N = 512$ spins. The higher the degeneracy of the first excited state, the lower the resilience. This can be explained by the increased probability of level crossing. We also color code each dot in the figure: The heat map represents the number of instances that had a

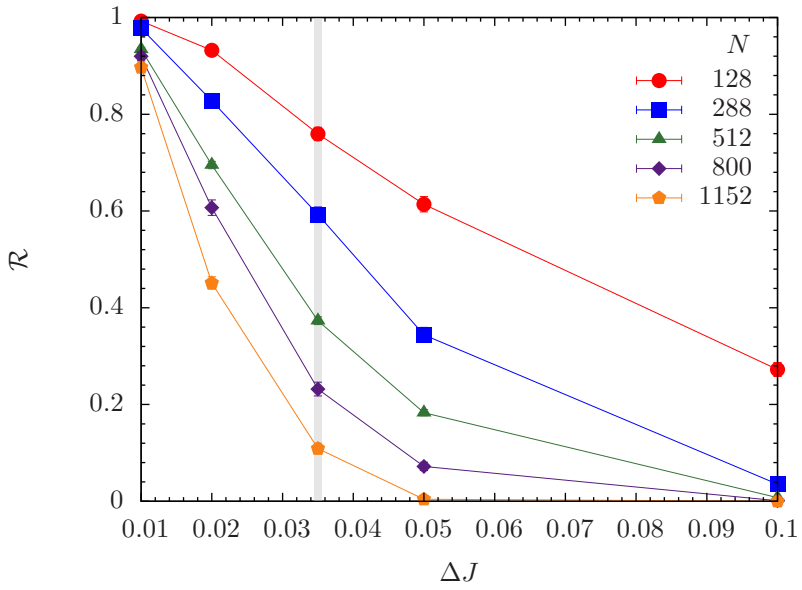

Figure 4.4: Resilience $\mathcal{R}$ of the $U_{5,6,7}$ instance class as a function of the bond fluctuation strength (ΔJ) for different system sizes N on the Chimera topology. The resilience clearly decreases for increasing noise and system size. The shaded vertical line represents the current bond-noise strength in the D-Wave Two system, approximately 3.5%.

given degeneracy N_1 of the first excited state out of the 900 simulated. In this case, the bulk of the instances have between 4 and 8 degenerate first excited states. This results in a reduction of the resilience, compared to instances that contain only one or two first excited states.

While instances with only one or two first excited states are extremely rare, the effort needed to find these might outweigh the approximately 30% in the resilience reduction by allowing states with three to four first excited states. We thus recommend to fix the number of first excited states to be less or equal than four in this case.

We have also computed the Hamming distance between the ground state and all first excited states for a given instance. Our results suggest that when the average

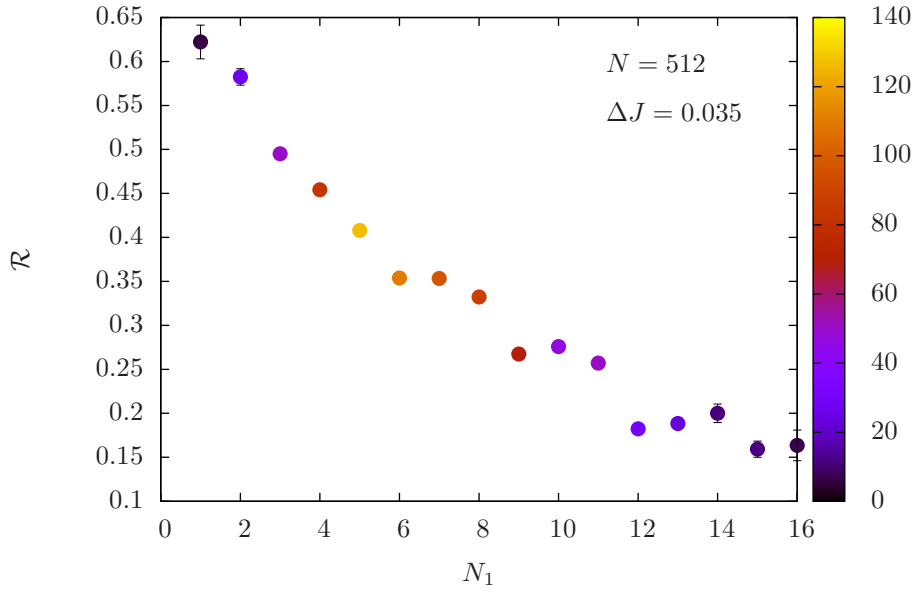

Figure 4.5: Resilience $\mathcal{R}$ as a function of the number of first excited states N_1 for $N = 512$ spins on the Chimera lattice. The data are for the $U_{5,6,7}$ instance class. The color bar shows approximately how often a given number of first excited states occurs for the 900 instances studied. In this case, between four and eight first excited states are most common.

Hamming distance is small, the resilience to noise is higher. A simple explanation is that both ground-state and excited configurations are quite similar and therefore the noise affects them comparably, i.e., both the ground state and the first excited states are lifted approximately by the same amount.

4.3 Conclusions

In order to develop both hard and robust benchmark instances, we have tested different instance classes by computing their yield (fraction of instances with a unique ground-state configuration) and resilience to noise fluctuations. Ideally, hard instances (high yield) with a high resilience are optimal for benchmarking purposes. Both yield and resilience can be tuned by a careful design of the instance classes—within the hardware restrictions of the machine—followed by a mining of the data.

Although the numerical effort to do such "designer instances" is nonnegligible, we think this is a key ingredient in designing good benchmarks for quantum annealing devices, as well as any other computing architectures. It seems that both resilience and yield for the Chimera topology are slightly anticorrelated. A good compromise is thus the $U_{5,6,7}$ instance class that has a good resilience to both field and coupler noise, as well as a nonzero yield of unique ground states, with a small number of first excited states.

We emphasize that our results for the resilience represent a *best-case scenario* for any quantum annealing machine. Any other source of error can only decrease the success probabilities further. However, it could be that the introduction of carefully-crafted correlations between bond and field noise might reduce the errors and increase the resilience. Bond noise is the most limiting issue for the current D-Wave Two quantum annealer and is highly dependent on the connectivity of the graph. While it is desirable to have a high connectivity to be able to embed interesting problems on any putative architecture, one has to also keep in mind that noise levels should be far lower than in the current D-Wave machine.

This classical study of both resilience and yield plays an important role in the design of future adjacency matrices for quantum annealing machines. Our results and methods can easily be generalized to other systems and thus should be of general interest when designing hard instance problems that attempt to circumvent the limitations of current hardware. Furthermore, calibration of future generations of the D-Wave device should be improved to allow for the encoding of more complex Sidon sets and thus the design of harder benchmark problems.

We conclude by pointing out that while the main goal of this work is to produce problems that are robust to noise, the methodology presented can also be used to design tailored instances that are particularly sensitive to noise. This could play

an important role when designing approaches to better calibrate devices, as done in Ref. [150].

5. EFFICIENT CLUSTER ALGORITHM FOR SPIN GLASSES IN ANY SPACE DIMENSION*

A plethora of problems across disciplines map onto spin-glass-like Hamiltonians [143]. Despite decades of intense analytical and numerical scrutiny, a deep understanding of these paradigmatic models of disordered systems remains elusive. Given the inherent difficulties of studying these Hamiltonians analytically beyond mean-field theory as well as the continuous increase of computer power, progress in this field has benefited noticeably from numerical studies. The development of efficient Monte Carlo methods such as parallel tempering [42] and population annealing [43] has helped in understanding these systems at a much deeper level; however, most numerical studies are still plagued by corrections to finite-size scaling due to the small system sizes currently available [151].

In contrast, simulations of spin Hamiltonians without disorder and frustration are comparably simple: Ferromagnetic systems have greatly benefited from the development of cluster algorithms [47, 48] that help in overcoming critical slowing down close to phase transitions. Therefore, the holy grail of spin-glass simulations is to introduce accelerated cluster dynamics that improve upon the benefits of efficient simulation methods such as population annealing or parallel tempering Monte Carlo. In 2001 Houdayer introduced a seminal rejection-free cluster algorithm tailored to work for two-dimensional Ising spin glasses [50]. The method updates large patches of spins at once, therefore effectively randomizing the configurations and efficiently overcoming large barriers in the free-energy landscape. Furthermore, the energy of

*Reprinted from "Efficient Cluster Algorithm for Spin Glasses in Any Space Dimension" by Zheng Zhu, Andrew J. Ochoa, Helmut G. Katzgraber, 2015, Phys. Rev. Lett, Copyright 2015 by American Physical Society [147].

the system remains unchanged when performing a cluster move. This means that the numerical overhead is very small, because there is no need to, for example, compute any random numbers for a cluster update. The use of these cluster moves made it possible to obtain a speedup of several orders of magnitude in two space dimensions and therefore simulate considerably larger system sizes.

While cluster algorithms such as Swendsen-Wang and Wolff [47, 48] work well for ferromagnetic systems in any space dimension because the clusters reflect the spin correlations in the system, this is not the case for algorithms that build clusters like the Houdayer cluster algorithm. In this case the clusters do not reflect overlap correlations [152, 153] and cluster updates only have an accelerating effect on the dynamics if the clusters do not span the entire system and are not comprised of single spins. This is the case either when temperatures are close to zero (small clusters), or when the underlying geometry of the problem has a percolation threshold below 50% – as is the case in three space dimensions. Updating such a system-spanning cluster amounts to swapping out both replicas, thus not randomizing the configurations. This means that while the method works in principle, it does not really provide any simulational benefit. As such, Houdayer cluster moves work, in principle, only for models where the percolation threshold is above 50%, as is the case in two-dimensional Ising spin-glass Hamiltonians. One way to remedy this situation is to increase the percolation threshold artificially, e.g., by diluting the lattice [154]. However, this is often not desirable and highly dependent on the problem to be studied.

In this chapter I show an algorithm that I have developed where Houdayer-like cluster moves can be applied to spin systems on topologies where the percolation threshold is below 50%, provided that the interplay of temperature and frustration prevents clusters from spanning the whole system. We therefore introduce *isoener-*

getic cluster moves for spin-glass-like Hamiltonians in any space dimension. These rejection-free cluster moves accelerate thermalization by several orders of magnitude even for systems with space dimensions larger than 2. We show that the inherent frustration present in spin-glass Hamiltonians prevents clusters from spanning the whole system for temperatures below the characteristic energy scale of the problem. As such, spin-glass simulations can be sped up considerably in the hard-to-reach low-temperature regime of interest in many numerical studies.

The fact that the isoenergetic cluster moves are rejection free and leave the energy of the system unchanged is also of great importance to any heuristic based on Monte Carlo updates to compute ground-state configurations of spin-glass-like Hamiltonians. For example, the convergence of simulated annealing [36] can be considerably improved by adding isoenergetic cluster moves at each temperature step. Because the moves change the spin configurations but leave the energy of the system intact, the approach has the potential to "tunnel" through energy barriers, thus overall improving convergence.

I first introduce the benchmark model, followed by a short description of the Houdayer cluster algorithm and an outline of our isoenergetic cluster algorithm. Results in two and three space dimensions, as well as on the nonplanar Chimera topology [125] are presented.

5.1 Benchmark model and observables

The Hamiltonian of a generic Ising spin glass is defined by

$$\mathcal{H} = \sum_{i \neq j}^{N} J_{ij} s_i s_j, \tag{5.1}$$

where $s_i \in \{\pm 1\}$ represent Ising spins and N is the total number of spins. In this study the interactions J_{ij} are selected from a Gaussian distribution with mean zero and variance $J^2 = 1$. Because we are only interested in highlighting the improved thermalization by adding isoenergetic cluster moves, we measure the average energy per spin defined via $[\langle \mathcal{H} \rangle]/N$, as well as the link overlap

$$q_\ell = (1/N_b) \sum_{ij}^{N} s_i^{(1)} s_j^{(1)} s_i^{(2)} s_j^{(2)}. \tag{5.2}$$

Here, $\langle \cdots \rangle$ represents a Monte Carlo average, the superscripts represent two replicas of the system, $[\cdots]$ an average over the disorder, and N_b is the number of bonds in the system. Using Gaussian disorder, one can equate the internal energy per spin to the internal energy computed from the link overlap [51], $E(q_\ell)$, i.e.,

$$E(q_\ell) = -\frac{J^2}{T} \frac{N_b}{N} (1 - q_\ell). \tag{5.3}$$

To test that the system is thermalized, we thus study the time-dependent behavior of

$$\Delta = [\langle E(q_\ell) \rangle - \langle \mathcal{H}/N \rangle]. \tag{5.4}$$

When $\Delta \to 0$, the bulk of the disorder instances is thermalized [144]. Simulation parameters are listed in Table 5.1

5.1.1 Reminder: Houdayer cluster algorithm

The Houdayer cluster algorithm (HCA) [50] is an efficient algorithm to study *two-dimensional* Ising spin glasses at low temperatures where thermalization is slow. It is similar to replica Monte Carlo [155], but with the difference that both replicas are at the *same* temperature. By allowing large cluster rearrangements of configura-

tions, the HCA improves thermalization by efficiently tunneling through configuration space.

The algorithm works as follows: In the HCA, two independent spin configurations (replicas) are simulated at the same temperature. The site overlap between replicas (1) and (2), $q_i = s_i^{(1)} s_i^{(2)}$, is calculated. This creates two domains in q-space: sites with $q_i = 1$ and $q_i = -1$. Clusters are defined as the connected parts of these domains in q-space. One then randomly chooses one site with $q_i = -1$ and builds the cluster by adding all the connected spins in the domain with probability 1. When no more spins can be added to the cluster in q-space, the spins in *both* replicas that correspond to cluster members are flipped with probability 1, irrespective of their orientation. The method can be implemented in a very efficient way because cluster members are added with probability 1 and the cluster updates are rejection free. To ensure ergodicity, the cluster move is combined with standard single-spin Monte Carlo updates. Summarizing, one simulation step using the HCA consists of the following steps:

1. Perform one Monte Carlo sweep (N Metropolis updates) in each replica.

2. Perform one Houdayer cluster move.

3. Perform one parallel tempering update for a pair of neighboring temperatures.

Note that the last step is not necessary; however, the combination of HCA moves and parallel tempering (PT) updates improves thermalization considerably and represents the standard modus operandi.

In theory, the efficiency of the HCA depends strongly on the percolation threshold of the desired topology to be simulated. Because spins are added to the cluster with probability 1, if the percolation threshold of the studied lattice is below 50%, then the

cluster might span the entire system and an update will not yield a new configuration. This is the reason why HCA is claimed to only work in two space dimensions [50] where the percolation threshold is above 50% (see also Figures 5.1 to 5.3).

5.1.2 Isoenergetic cluster algorithm

Our proposed isoenergetic cluster moves are closely related to the HCA. We begin by simulating two replicas with the same disorder at multiple temperatures. The cluster moves alone are not ergodic, so, again, these must be combined with simple Monte Carlo updates. One simulation step using isoenergetic cluster moves consists of the following steps:

1. Perform one Monte Carlo sweep (N Metropolis updates) in each replica.

2a. If the number of cluster members with $q_i = -1$ is greater than $N/2$, then all the spins in one of the configurations can be flipped, thus reducing the cluster size while leaving the energy unchanged.

2b. Perform one Houdayer cluster move for all temperatures $T \lesssim J$.

3. Perform one parallel tempering update for a pair of neighboring temperatures.

The main difference thus lies in applying cluster moves to a carefully-selected set of temperatures where the isoenergetic cluster moves (ICMs) are efficient (steps 2a & 2b) because clusters do not percolate, as well as reducing cluster sizes and thus the numerical overhead by exploiting spin-reversal symmetry (step 2a) [159, 160]. For example, in the case of the Chimera lattice the overhead of ICM over PT is approximately 25% and roughly independent of the system size for the studied N. However, the overhead for HCA over PT is at least 50% and grows with increasing system size.

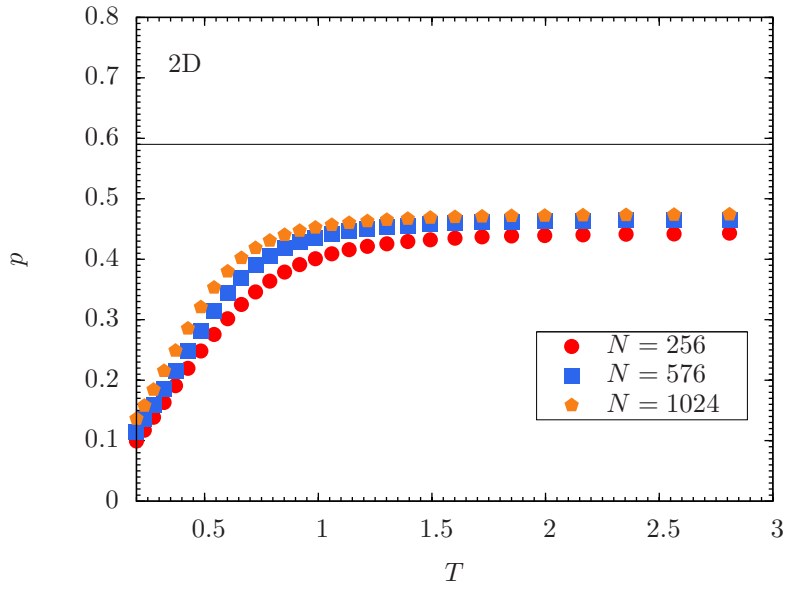

Figure 5.1: Fraction of spins p of potential cluster members as a function of temperature T for different system sizes N in two space dimensions (2D). The horizontal line represents the percolation threshold of a two-dimensional square lattice, i.e., $p_c \approx 0.592$ [156]. Because $p \to 0.5$ for $T \to \infty$, for all T clusters do not percolate, which is why the HCA is efficient in two-dimensional planar geometries. Error bars are computed via a jackknife analysis over configurations and are smaller than the symbols.

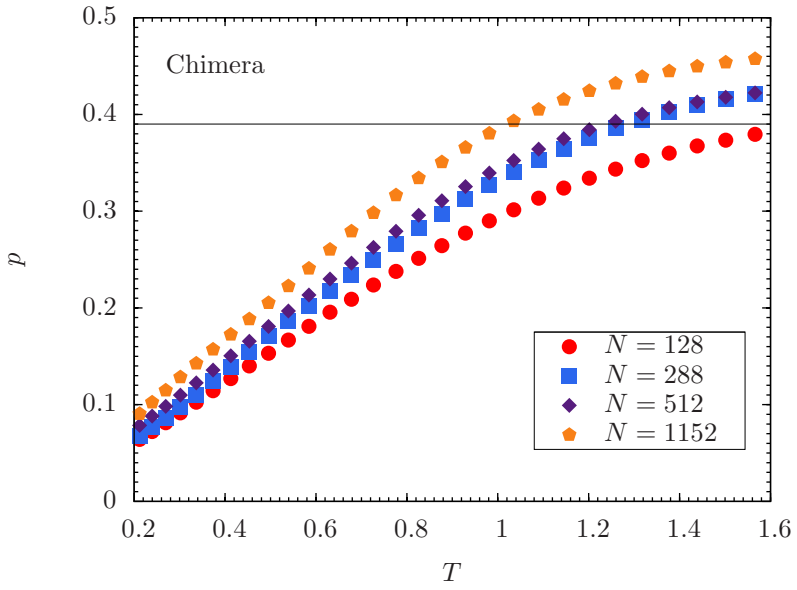

Figure 5.2: Fraction of spins p as a function of temperature T for different system sizes N on the Chimera topology. The horizontal line represents the percolation threshold of the nonplanar Chimera topology, namely $p_c \approx 0.387$ computed here using the approach developed in Ref.[157]. For $T \gtrsim J = 1$ clusters percolate and cluster updates provide no gain. Error bars are computed via a jackknife analysis over configurations and are smaller than the symbols.

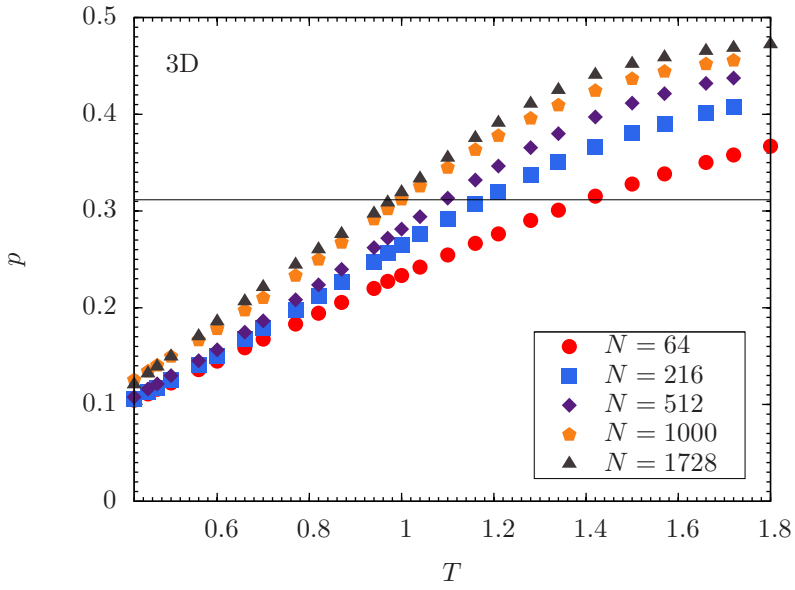

Figure 5.3: Fraction of spins p as a function of temperature T for different system sizes N in three space dimensions (3D). The horizontal line represents the percolation threshold of the three-dimensional cubic lattice ($p_c \approx 0.311$ [158]). For $T \gtrsim J = 1$ clusters percolate. Error bars are computed via a jackknife analysis over configurations and are smaller than the symbols.

Figures 5.1 to 5.3 show the fraction of spins with negative overlap (i.e., the fraction of potential cluster members) as a function of temperature T for different system sizes N and on three different topologies. Fig. 5.1 shows data in two space dimensions where the percolation threshold is $p_c \approx 0.592$ [156] (solid horizontal line). As such, for all temperatures simulated, the fraction of cluster members is below the percolation threshold and saturates at 50% for $T \to \infty$. This means that isoenergetic cluster updates are efficient for all temperatures studied because the clusters never percolate. Naively, one would expect that in higher space dimensions clusters percolate for all T. This is, however, not the case due to the frustration present in spin glasses, as can be seen for the Chimera topology (Fig. 5.2) or in three space dimensions (Fig. 5.3). For increasing system size the fraction of cluster members converges to a limiting

curve that crosses the percolation threshold (horizontal solid lines) at approximately $T \approx J = 1$. This means that for all $T \gtrsim J$ clusters percolate and the cluster updates are just numerical overhead without any advantage to the simulation. However, for $T \lesssim J$ the fraction of cluster members lies below the percolation threshold. This means that performing cluster moves in this temperature regime should improve thermalization. Note that it is a coincidental property that for three-dimensional Ising spin glasses $T_c \sim 1$ [95], i.e., that cluster moves can be applied to any $T \lesssim T_c$ [161].

When the interactions J_{ij} are drawn from a Gaussian distribution, the ground state is unique. As can be seen in figs. 5.1 to 5.3, the fraction p of spins potentially in a cluster also approaches zero for $T \to 0$, i.e., both replicas are in the ground state for low enough T. Therefore, the cluster is composed of no members or the entire lattice. In the case of disorder distributions that yield a highly-degenerate ground state, such as it is the case for bimodal disorder, it is possible to continue to have clusters at zero temperature. It is thus possible to efficiently hop around the ground-state manifold by applying cluster moves to low-lying or even zero-temperature states. We do emphasize, however, that if clusters are too small, then the isoenergetic cluster moves also become ineffective. Therefore, plotting the p as done in figs. 5.1 to 5.3 is essential in determining the efficiency and applicability of the method.

5.2 Benchmarking results

Figures 5.4 to 5.6 show Δ [Eq. (5.4)] as a function of Monte Carlo time (measured in lattice sweeps) $t = 2^b$. Fig. 5.4 shows data in two space dimensions for simulations using isoenergetic cluster moves (PT+ICM) and vanilla parallel tempering (PT) Monte Carlo for $N = 1024$ spins at $T = 0.212$. Once $\Delta \sim 0$, we deem the system thermalized. Clearly, the inclusion of cluster moves—as can also be expected from

Table 5.1: Parameters of the simulation in two space dimensions (2D), three space dimensions (3D), and on the Chimera (Ch) topology. For each topology simulated and system sizes N, we compute N_{sa} disorder instances and measure over 2^b Monte Carlo sweeps (and isoenergetic cluster moves) for each of the $2N_T$ replicas. T_{min} [T_{max}] is the lowest [highest] temperature simulated, and N_T is the total number of temperatures used in the parallel tempering Monte Carlo method. Isoenergetic cluster moves only occur for the lowest N_{c} temperatures simulated (determined from figs. 5.1 to 5.3).

	N	N_{sa}	b	T_{min}	T_{max}	N_T	N_{c}
2D	256, 576, 1024	10^4	22	0.2120	1.6325	30	30
Ch	128, 288, 512, 800, 1152	10^4	22	0.2120	1.6325	30	19
3D	64, 216, 512, 1000, 1728	$1.5\,10^4$	23	0.4200	1.8000	26	13

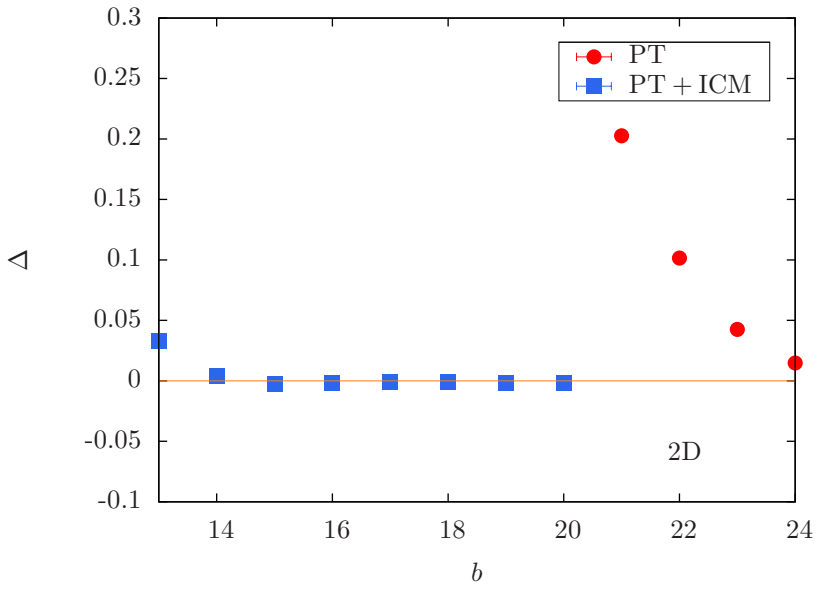

Figure 5.4: Δ [Eq. (5.4)] as a function of simulation time $t = 2^b$ measured in Monte Carlo sweeps in two space dimensions (2D) for $N = 1024$ and $T = 0.212$. Simulations using vanilla PT thermalize at at least 2^{25} Monte Carlo sweeps, whereas with the addition of ICMs thermalization is reduced to approximately 2^{16} Monte Carlo sweeps. This means approximately two orders of magnitude improvement. Error bars are computed via a jackknife analysis over configurations.

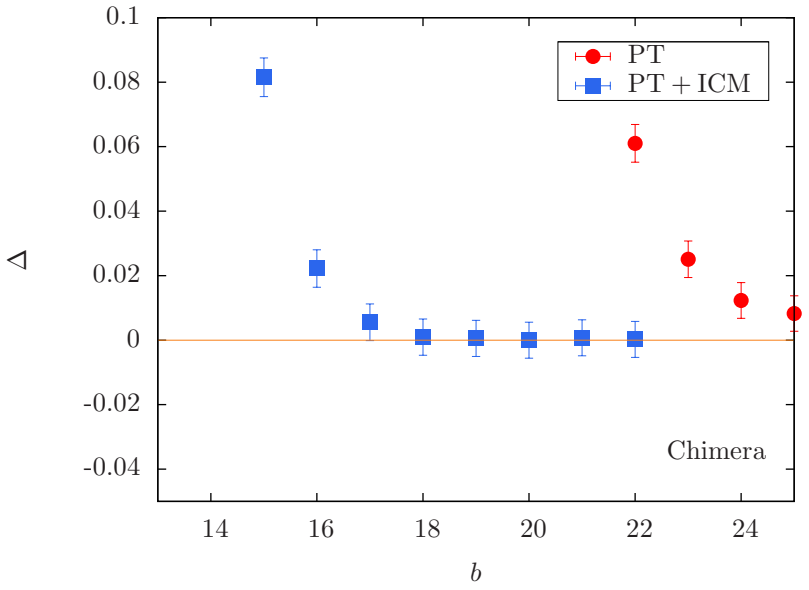

Figure 5.5: Δ as a function of simulation time $t = 2^b$ measured in Monte Carlo sweeps for an Ising spin glass on Chimera with $N = 1152$ spins at $T = 0.212$. Simulations using PT thermalize at approximately 2^{25} Monte Carlo sweeps, whereas the addition of ICMs reduces thermalization to 2^{18} Monte Carlo sweeps. Again, approximately two orders of magnitude speedup. Error bars are computed via a jackknife analysis over configurations.

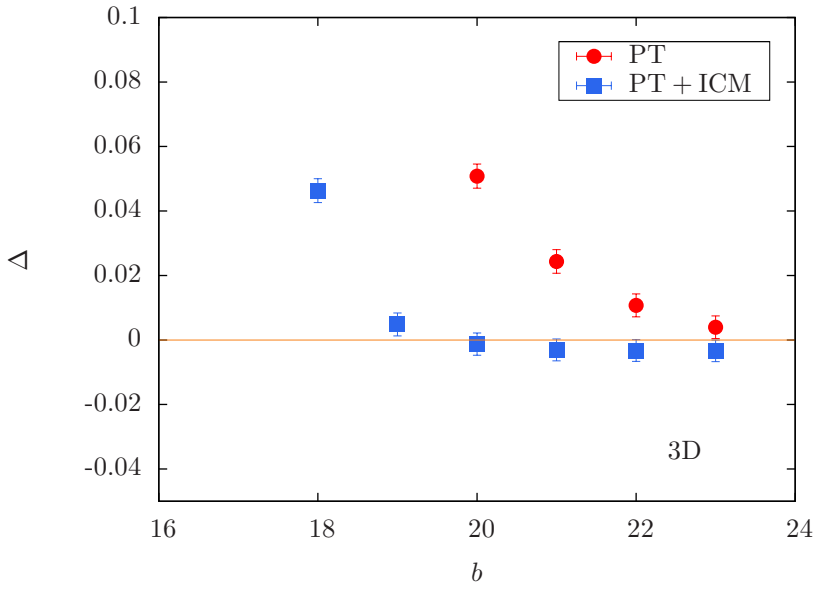

Figure 5.6: Δ as a function of simulation time $t = 2^b$ measured in Monte Carlo sweeps in three space dimensions (3D) for $N = 1728$ and $T = 0.42 \sim 0.43 T_c$. Using standard PT, the system thermalizes approximately after 2^{23} Monte Carlo sweeps. This time is reduced to $\sim 2^{20}$ Monte Carlo sweeps when ICMs are added. Error bars are computed via a jackknife analysis over configurations.

the results of Houdayer—show an improved thermalization. Fig. 5.5 shows data on the Chimera topology with $N = 1152$ spins and $T = 0.212$, where the HCA is not expected to show any improvement over PT due to $p_c < 0.5$. As can be seen, our ICM clearly improve thermalization in comparison to PT by at least two orders of magnitude; an amount that grows with increasing system size. Finally, Fig. 5.6 shows Δ as a function of simulation time in three space dimensions with $N = 1728$ spins and $T = 0.42 \ll T_c$. Although not as impressive as for the Chimera topology, we see a speedup of approximately one order of magnitude — an amount that again grows with increasing system size.

Finally, Fig. 5.7 shows the ratio of the thermalization time using PT and using PT+ICM for different topologies at the lowest simulation temperature (see Tab. 5.1)

as a function of the system size N. In all cases, the speedup increases with increasing system size, therefore illustrating that the addition of isoenergetic cluster moves greatly improves thermalization.

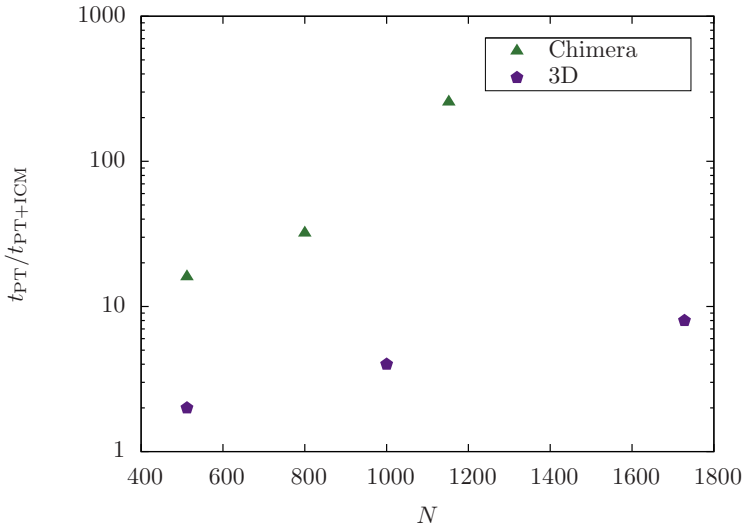

Figure 5.7: Ratio between the *approximate* average thermalization time of PT and PT+ICM for different topologies at the lowest simulation temperature (see Tab. 5.1) as a function of system size N. In all cases the speedup increases with increasing system size. Note that thermalization times have been determined by eye.

5.3 Summary

We have presented a rejection-free cluster algorithm for spin glasses in any space dimension that greatly improves thermalization. By restricting Houdayer cluster moves to temperatures where cluster percolation is hampered by the interplay of frustration and temperature, we are able to extend the Houdayer cluster algorithm for two-dimensional spin glasses to any topology/space dimension. Our standard implementation of the cluster updates represents only a minor overhead [160] compared to the thermalization time speedup obtained from the isoenergetic cluster moves –

a speedup that increase with the system size [162], significantly minimize resource usage and reduce the finite size scaling corrections.

6. EFFICIENT SAMPLING OF GROUND STATE CONFIGURATIONS FOR QUASI TWO-DIMENSIONAL ISING SPIN GLASSES

Spin glass physics provides a rich source of challenging theoretical and computational problems. In particular, the problem of finding ground states is very difficult because of the quenched disorder and frustration that are present in spin glass models. Therefore, many different algorithms have been proposed to solve the ground state problem. Generally speaking, the time that an exact method such as branch-and-cut [163] takes to find ground states is at a much greater order of magnitude than heuristic methods such as genetic algorithms [164], simulated annealing, parallel tempering [56, 165], population annealing [57], and quantum annealing [103]. The first three classical Monte Carlo heuristics based on thermal annealing are known to almost uniformly sample all ground states and low-lying excited states. Quantum annealing is a general heuristic method that can find ground states by controlling quantum fluctuations, it allows a system to exploit quantum superposition and tunnel through the rough energy landscape, which will potentially find the ground states more quickly.

However, research by Matsuda, Nishimori and Katzgraber [166] suggests that while quantum annealing is superior to simulated annealing for finding ground state energy, it has a bias towards a subset of the ground states. As a consequence, verifying that an optimizer can sample all ground state configurations is a far more stringent test for any newly developed algorithm. It is well known that parallel tempering is more efficient than simulated annealing at finding spin glass ground states with equal probability [56], and recent results show that population annealing and parallel tempering are comparably efficient [57]. Here I show that the Isoenergetic

Cluster Algorithm (ICA) [147] from the previous chapter enhances the sampling of ground states for quasi two-dimensional Ising spin glasses with a space dimension less than three. The method is based on a combination of low-temperature parallel tempering (PT) Monte Carlo and rejection-free isoenergetic cluster move. We illustrate the approach for Ising spin glasses on the D-Wave Two quantum annealer topology, known as the Chimera graph, as well as for two-dimensional Ising spin glasses with interactions $J_{ij} \in \{\pm 1, \pm 2, \pm 4\}$ (see next section).

The rest of this chapter is organized as follows. In the next section, I introduce the criteria from the theory of binomial distribution for fair sampling with equal probability, and I provide a detailed description of fair sampling algorithm ICA. Following that, I present numerical results for both PT and ICA on a Chimera graph as well as a 2D square lattice. The last section presents our concluding remarks.

6.1 Model, algorithm and observables

In order to illustrate ICA, we start with an Ising spin glass model on a non-planar Chimera graph. An example of the Chimera topology with 8×8 blocks of 8 spins can be found in chapter 4. Its non-planar topology makes finding ground states of Ising spin glasses defined on a Chimera graph worst-case NP-hard problems [64]. The Hamiltonian for the spin glass model is given by

$$\mathcal{H}(\{s_i\}) = -\sum_{i<j}^{N} J_{ij} s_i \, s_j, \tag{6.1}$$

where $s_i \in \{\pm 1\}$ are the Ising spins and $J_{ij} \in \{\pm 1, \pm 2, \pm 4\}$ are the interactions. The interactions are selected based on the range of ground state degeneracy we can simulate with our high-performance computing cluster.

Suppose n is the total number of times that ground states are found for a sample

with ground state degeneracy G. The probability distribution for finding any particular ground state is called a *binomial* distribution. If p is the probability of success and q is the probability of failure in a binomial trial, then the expected number of successes in n trials is $e = np$ and the variance of the binomial distribution is $\sigma^2 = npq$. Therefore, the theoretical relative variance Q_{th} is given by

$$Q_{\text{th}} = \sigma/e = \sqrt{(1-p)/np} = \sqrt{(G-1)/n}. \tag{6.2}$$

An algorithm is said to be optimal if the relative fluctuation of the frequency of ground states is close or equal to the theoretical value $\sqrt{(G-1)/n}$. In practice, this numerical relative variance for any algorithm is greater than the theoretical value, due to limited computational resources.

Here are the details of our fair sampling algorithm ICA:

1. Run N_T sets of replicas of the system at a range of temperatures $\{T_1, T_2, ..., T_{N_T}\}$, with each set consisting of $M = 4$ replicas at the same temperature, thus $4 \times N_T$ copies of the system with the same disorder are randomly initialized.

2. N_{sw} iterations are performed, each iteration consisting of one Monte Carlo sweep, a parallel tempering update, and a isoenergetic cluster move (but only for the lowest N_{hc} temperatures).

3. For the first $N_{\text{sw}}/8$ iterations, we keep track of the lowest energies for the 4 replicas with the lowest temperature.

4. After $N_{\text{sw}}/8$ iterations, the lowest energies E_1, E_2, E_3, and E_4 for the 4 replicas with the lowest temperature are compared, and if $E_1 = E_2 = E_3 = E_4$, we claim that the ground state has been found and we begin to record the ground state configurations and frequency for the remaining $7N_{\text{sw}}/8$ updates.

Table 6.1: Parameters of the simulation: For each instance class and system size N, we compute N_{sa} instances. $N_{\mathrm{sw}} = 2^b$ is the total number of Monte Carlo sweeps for each of the $4N_T$ replicas for a single instance, T_{min} [T_{max}] is the lowest [highest] temperature simulated, and N_T and N_{hc} are the number of temperatures used in the parallel tempering method and in the isoenergetic cluster algorithm, respectively.

Topology	N	N_{sa}	b	T_{min}	T_{max}	N_T	N_{hc}
2D	144	360	25	0.2120	1.6325	30	19
2D	256	359	25	0.2120	1.6325	30	19
2D	576	355	25	0.2120	1.6325	30	19
2D	784	343	25	0.2120	1.6325	30	19
2D	1024	245	25	0.2120	1.6325	30	19
Chimera	128	360	25	0.2120	1.6325	30	19
Chimera	288	360	25	0.2120	1.6325	30	19
Chimera	512	360	25	0.2120	1.6325	30	19
Chimera	800	359	25	0.2120	1.6325	30	19
Chimera	1152	360	25	0.2120	1.6325	30	19

Note there is no guarantee that any solution obtained by this heuristic method is the true optimum, or that we have found all configurations that minimize the Hamiltonian. The simulation parameters are shown in Table 6.1.

6.2 Numerical results

In order to test whether ICA can sample ground states with equal probabilities, we multiply the numerical relative variance Q_{num} by the square root of the total number of times ground states are found, $\sqrt{n}$, and we plot this quantity $Q_{\mathrm{num}}\sqrt{n}$ as a function of the ground state degeneracy $G-1$. It is not difficult to verify that $Q_{\mathrm{th}}\sqrt{n}$ is the square root of the ground state degeneracy $G-1$, and therefore the function $Q_{\mathrm{th}}\sqrt{n} = \sqrt{G-1}$ is a straight line in logarithmic scale for both the x-axis ($x = G-1$) and the y-axis ($y = Q_{\mathrm{th}}\sqrt{n}$).

Figure 6.1 shows the quantities $Q_{\mathrm{num}}\sqrt{n}$ and $Q_{\mathrm{th}}\sqrt{n}$ as a function of ground state degeneracy $G-1$ for different spin glass samples on a chimera graph; as we

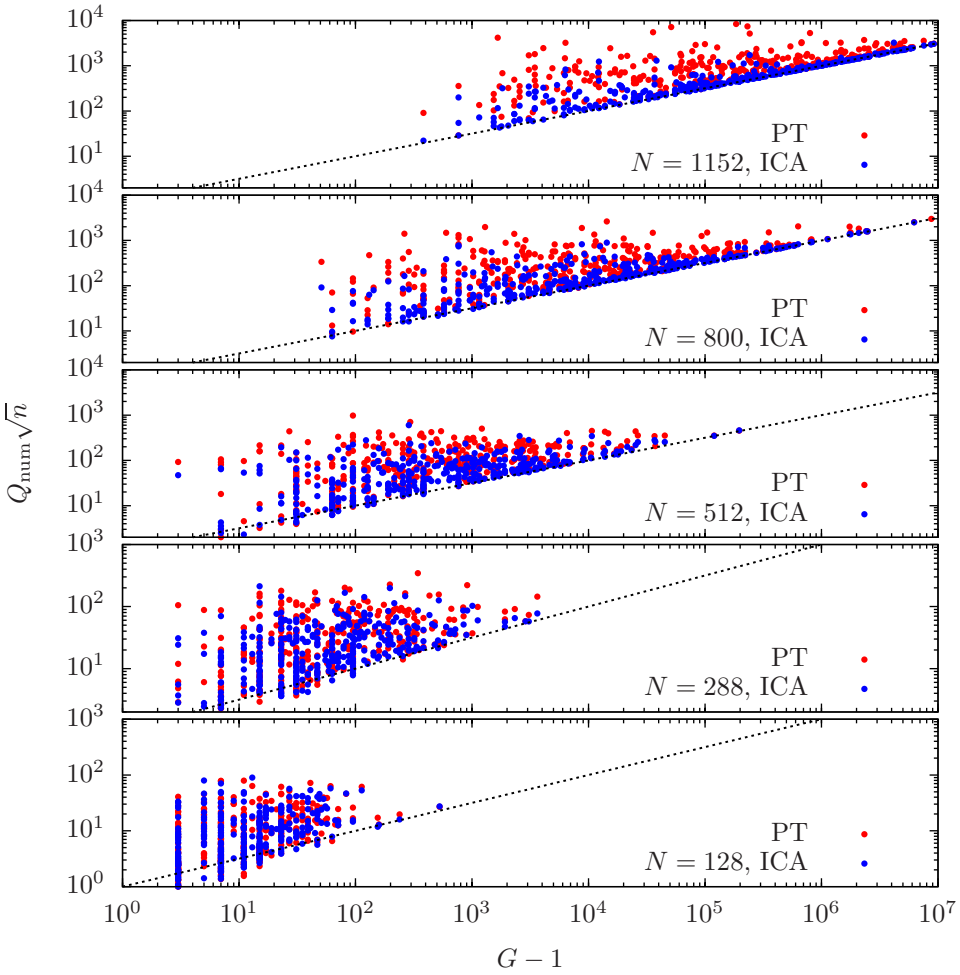

Figure 6.1: Scatter plot of quantities $Q_{\mathrm{num}}\sqrt{n}$ as a function of the ground state degeneracy $G - 1$ for different spin glass samples with different system sizes N on a Chimera graph. The data points for ICA (blue color) are closer to the theoretical limit than those for the PT (red color), and this improvement gets better as the system size increases.

mentioned earlier, the quantity $Q_{\mathrm{num}}\sqrt{n}$ is almost always greater than $Q_{\mathrm{th}}\sqrt{n}$ due to limited computational resources. However, the algorithm is claimed to be optimal if the data points from the numerical relative variance are close to a straight line. It is clear that the data points from ICA (blue color) are closer to a straight line than the data points from PT (red color), and the discrepancy between ICA and PT seems

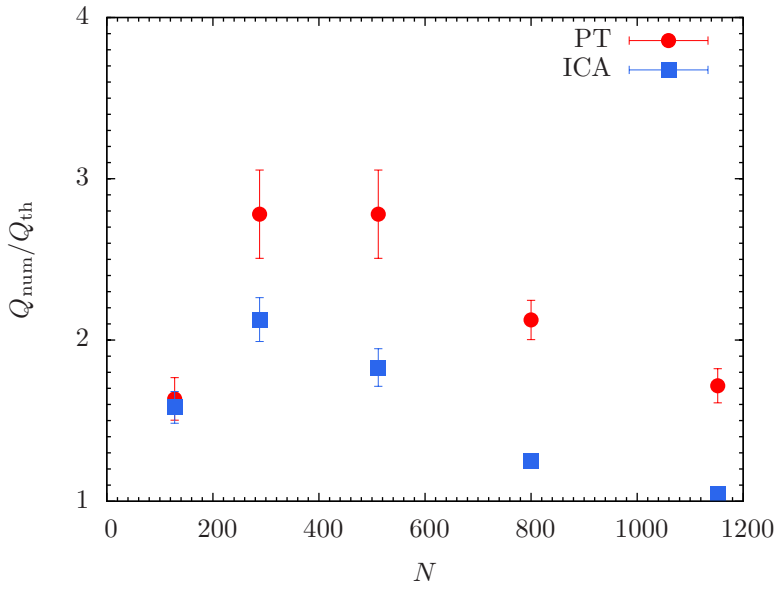

Figure 6.2: Median ratio $Q_{\rm num}/Q_{\rm th}$ over different spin glass samples as a function of the system size N on a Chimera graph. The data points show that ICA (blue color) is better than PT (red color) for all system sizes, and the general trend for both algorithms is that the ratio goes up as the system size increases, then it peaks at a certain point, and beyond a certain system size the ratio goes down as the system size continues to increase. Note there is no critical point and phase transition here.

to become greater as the system size increases.

In Fig. 6.2 we plot the median ratio $Q_{\rm num}/Q_{\rm th}$ over different samples as a function of the system size N, and a ratio of one means the algorithm is perfectly optimal. The data points show that ICA (blue color) is better than PT for all system sizes, and the general trend for both algorithms is that in the beginning the ratio goes up as the system size increases, then it peaks at a certain point, and beyond a certain system size the ratio goes down as the system size continues to increase. One explanation for this trend is that there are two main factors that determine the ratio, the system size and the ground state degeneracy, and a larger system size with the same ground state degeneracy makes fair sampling harder while the same system size with a larger ground state degeneracy makes fair sampling easier, so that the dominant

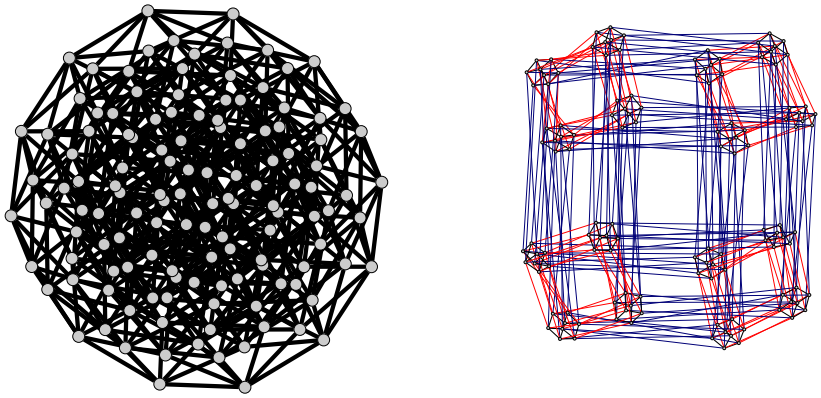

Figure 6.3: Two examples of ground state configurations with different Hamming distances on a Chimera graph for system size $N = 512$. The Hamming distance denotes the difference between two binary strings (ground state configurations). Each dot in the figure represents a ground state, black lines are 1-bit differences, red lines are 2-bit differences, and anything that is a light color or blue is an even greater difference. In the example on the left, all ground state configurations are related by 1-bit differences, while the example on the right shows that Hamming distances between certain ground state configurations can be large—which means that it will take longer for the system to move from one ground state to another and this will cause larger fluctuations in the ground state frequency.

factor determines whether the ratio goes up or down. Below a certain system size the dominant factor is the system size, while above that size the ground state degeneracy is dominant. In addition, careful examination of samples with the same system size and ground state degeneracy shows that the $Q_{\mathrm{num}}/Q_{\mathrm{th}}$ ratio is closely related to the Hamming distances between ground state configurations: the samples with large Hamming distances between the ground states tend to have a high $Q_{\mathrm{num}}/Q_{\mathrm{th}}$ ratio, while those with small Hamming distances are more likely to have a low $Q_{\mathrm{num}}/Q_{\mathrm{th}}$ ratio. Two examples of ground state configurations with different Hamming distances on a Chimera graph are shown in Fig. 6.3, for $N = 512$. Note that the statistical error bars are determined by a bootstrap analysis using the following procedure:

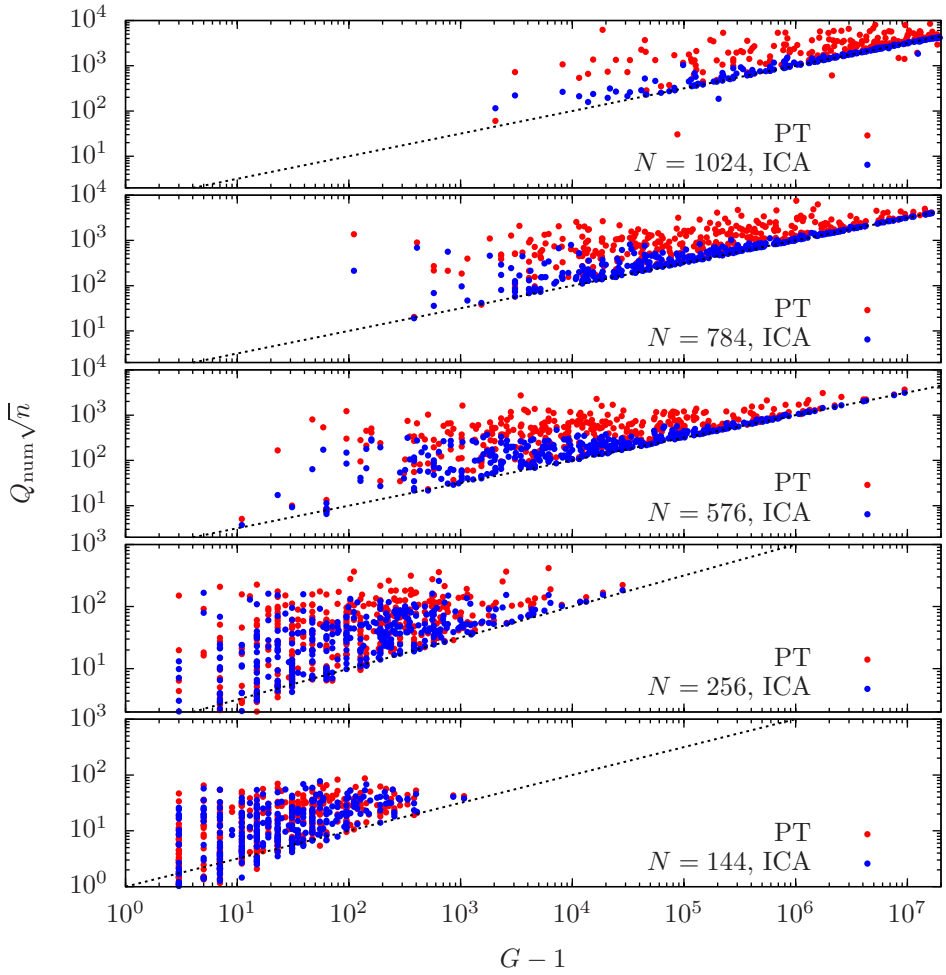

Figure 6.4: Scatter plot of quantities $Q_{\rm num}\sqrt{n}$ as a function of the ground state degeneracy $G - 1$ for different spin glass samples with different system sizes N on a 2D lattice. The data points for ICA (blue color) are closer to the theoretical limit than those for the PT (red color), and this improvement gets better as the system size increases.

For each system size N and $N_{\rm sa}$ disorder realizations, a randomly selected bootstrap sample of the $N_{\rm sa}$ disorder realizations is generated. The median ratio $Q_{\rm num}/Q_{\rm th}$ is computed with this random sample. We repeat this procedure $N_{\rm boot}$ times for each system size to obtain the average and standard deviation using these $N_{\rm boot}$ data points.

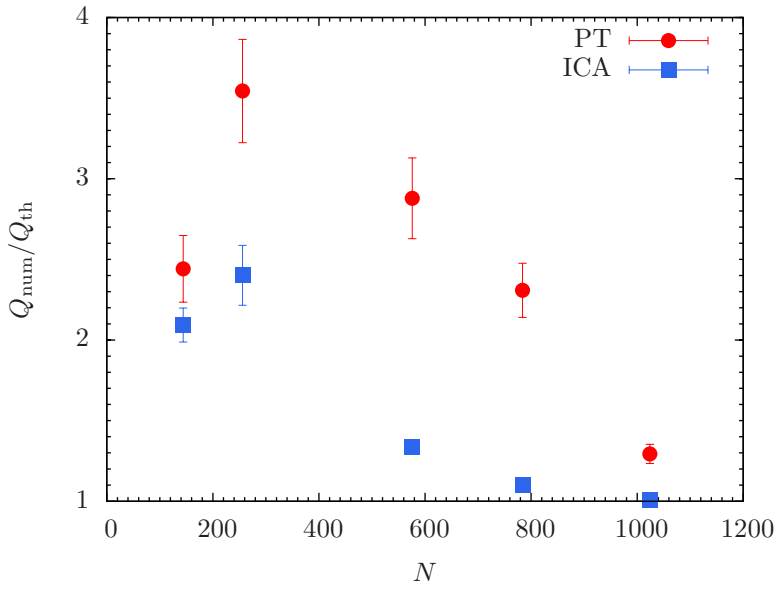

Figure 6.5: Median ratio $Q_{\rm num}/Q_{\rm th}$ over different spin glass samples as a function of the system size N on a 2D lattice. The data points show that ICA (blue color) is better than PT (red color) for all system sizes, and the general trend for both algorithms is that the ratio goes up as the system size increases, then it peaks at a certain point, and beyond a certain system size the ratio goes down as the system size continues to increase. Note there is no critical point and phase transition here.

Fig. 6.4 shows the quantities $Q_{\rm num}\sqrt{n}$ and $Q_{\rm th}\sqrt{n}$ as a function of the ground state degeneracy $G-1$ for different spin glass samples on a 2D lattice. Similar to the Chimera graph case, the data points from ICA (blue color) are closer to a straight line than the data points from PT (red color), and the discrepancy between ICA and PT becomes larger as the system size increases. In Fig. 6.5, the median ratio $Q_{\rm num}/Q_{\rm th}$ over different samples again demonstrates that ICA is superior to PT.

6.3 Conclusions

We have developed a novel cluster Monte Carlo algorithm for sampling ground states of Ising spin glasses on a Chimera graph as well as on a 2D square lattice. In this algorithm, parallel tempering updates combined with rejection-free isoenergetic

cluster moves create a robust ensemble that is able to sample both low- and high-energy configurations and allow global moves on the rough energy landscape. This improves thermalization for Ising spin glasses on a quasi two-dimensional nonplanar Chimera graph with dimension less than three, and a more equiprobable sampling of ground states has been achieved, which ensures all ground states for benchmarks can be found/computed. We also found that Hamming distances between different ground state configurations are closely related to the relative variance of frequency with which the ground states are found: ground states with small Hamming distances have a lower relative variance of frequency.

7. LIMITATIONS OF APPLYING TENSOR RENORMALIZATION GROUP METHODS TO GLASSY SYSTEMS

The simulation of strongly correlated quantum or classical statistical systems in two or higher dimensions remains a great challenge and stimulated great interest on tensor-network models in recent years [167, 168, 169, 170]. A tensor-network state is a high-dimensional generalization of the one-dimensional matrix-product state [171, 172] studied by the density-matrix renormalization group [173]. It captures the key feature of entanglement in interacting quantum systems and is considered to be an excellent tool to study correlated systems. On the other hand, in classical statistical system with local interactions, the Boltzmann weight can be expressed as a tensor product and all thermodynamic quantities can be determined by studying equivalent tensor-network model. The tensor renormalization group method (TRG) [168] was initially introduced by Levin and Nave as a real space renormalization group approach for classical spin systems on 2D regular lattices, then Xiang [174, 175] developed coarse graining TRG methods based on the higher-order singular value decomposition (HOTRG) [176] to study physical properties of 2D or 3D lattice models. HOTRG has recently been successfully applied to 2D and 3D Ising models [175]. However, it is unclear whether HOTRG can be applied to the 2D Edwards-Anderson (EA) spin glass model.

Although the EA model has been intensively studied over the past few decades, many aspects are still far from completely understood. Unlike the ferromagnetic Ising model, the EA spin glass model is a magnetic system exhibiting both quenched disorder and frustration without translation symmetry. Wang and coauthors [177] recently investigated whether TRG can be applied to the 2D EA model. They found

that TRG might lead to negative values of the partition function at low temperatures, and they argued that a larger cut-off parameter D_c could be used to decrease the probability of a negative partition function value. How to avoid negative partition function values at low temperatures is an open problem in the use of TRG for spin glasses.

In this chapter I argue that the primary reason for negative partition function values is the limited precision of the data type (double) used rather than the small cut-off parameter D_c. TRG fails because of the near-cancellation of the positive and negative tensor components in the partition function, a very high-precision data type is required for obtaining the difference of the tensor components with useful accuracy.

7.1 Model

In this section we illustrate the problems of HOTRG using the two-dimensional EA Ising spin glass defined on a 2D lattice, its Hamiltonian is given by

$$H(\{s_i\}) = -\sum_{i<j}^{N} J_{ij} s_i \, s_j, \tag{7.1}$$

where $s_i \in \{\pm 1\}$ are the Ising spins, and the bimodal-distributed interactions are given by

$$P(J_{ij}) = p(J_{ij} - 1) + (1 - p)(J_{ij} + 1), \tag{7.2}$$

with p being the fraction of ferromagnetic bonds. Although the EA model has been intensively simulated over the past few decades, most of the insights such as nature of the spin glass phase rely entirely on numerical simulations and remain highly debated [29, 178, 28, 179, 180, 30, 84].

7.2 Algorithm

The partition function for the classical statistical model with local interactions can be obtained by taking the product of local tensors at each site and summing over all bond indices. It is straightforward to show that the tensor-network representation of the partition function on a square lattice is given by

$$Z = Tr \prod_i T_{x_i x_i' y_i y_i'}. \tag{7.3}$$

The local tensor $T_{x_i x_i' y_i y_i'}$ can be defined by tracing out s_i from the product of W:

$$T_{x_i x_i' y_i y_i'} = \sum_{\alpha=1}^{D} W^2_{\alpha,x_i} W^1_{\alpha,x_i'} W^2_{\alpha,y_i} W^1_{\alpha,y_i'}, \tag{7.4}$$

where D is the original bond dimension and W^1 and W^2 are 2×2 matrices defined by

$$W^1 = \begin{pmatrix} \sqrt{\cosh(1/T)} & \sqrt{\sinh(1/T)} \\ \sqrt{\cosh(1/T)} & -\sqrt{\sinh(1/T)} \end{pmatrix}. \tag{7.5}$$

To coarse grain the network, two neighboring tensors are contracted into one:

$$M^{(n)}_{xx'yy'} = \sum_i T^{(n)}_{x_1 x_1' y i} T^{(n)}_{x_2 x_2' i y'}, \tag{7.6}$$

where $x = x_1 \otimes x_2$, $x' = x_1' \otimes x_2'$, and the superscript n denotes the n'th iteration. This reduces the lattice size by a factor of 2, and the contracted tensor $M^{(n)}$ along the x axis (or the y axis) has a higher bond dimension D^2. Without truncating the basis space, the bond dimension will grow to D^{2n} after n steps of coarse graining (one step of coarse graining consists of a contraction of the tensor along both the x and y axes). TRG truncates tensor $M^{(n)}$ into a lower-rank tensor with different

strategies. HOTRG is a simple TRG method based on higher-order singular value decomposition: one can renormalize tensor $M^{(n)}$ by multiplying a unitary matrix $U(n)$ on each horizontal side (or vertical side) to truncate the expanded dimension from D^2 to D_c,

$$T^{(n+1)}_{xx'yy'} = \sum_{ij} U^{(n)}_{ix} M^{(n)}_{ijyy'} U^{(n)}_{jx'}, \tag{7.7}$$

where $U(n)$ is determined by the higher-order singular value decomposition of the expanded tensor $M^{(n)}$. A new tensor $T^{(n+1)}$ with a reduced bond dimension is obtained, and truncation errors can be reduced by increasing the cut-off bond dimension D_c.

7.3 Numerical results

7.3.1 Exact method

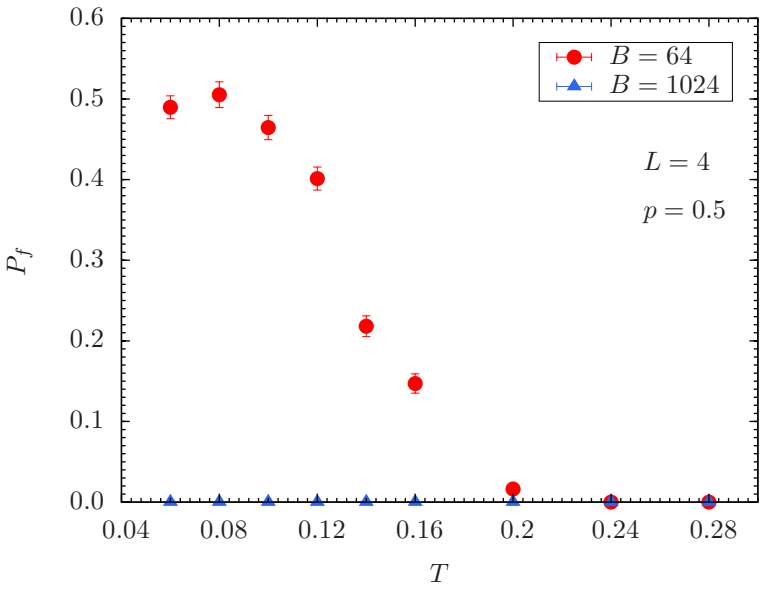

Figure 7.1: Failure rate P_f of the partition function for 2D Edwards-Anderson spin glass as a function of the temperature T. 960 samples with $L = 4$ and $p = 0.5$ were generated to calculate the failure rate and error bars.

The code was written in the C++ programming language, and all the thermodynamic quantities were stored with a double- or higher-precision data type from the GNU Multiple Precision Arithmetic Library (GMP) [181]. Without the truncation of TRG, a coarse graining scheme based on the tensor-network model should in principle produce an exact partition function for 2D EA Ising spin glass. Due to memory limitations, the maximum system size for this brute force method is $L = 4$ (The system with $L = 8$ requires $2^{35} = 34$GB memory) .

In order to demonstrate that the limited precision of the data type is the primary reason for negative partition function values for spin glass at low temperatures, we first define the *failure rate* P_f of the partition function as the number of samples with negative partition function values divided by the total number of samples: ($P_f = n_{\text{negative}}/n_{\text{total}}$). A total of 960 samples ($L = 4$) with randomly distributed bimodal interactions ($p = 0.5$) were generated, and partition functions for these samples were calculated with a double- (64 bits) and a higher-precision (1024 bits) data type. Figure 7.1 shows the failure rate of the partition function as a function of temperature. It is clear that with a double precision data type, the failure rate goes up as the temperature decreases. However, the failure rate vanishes with a 1024-bit precision data type.

To further show that higher-precision data types can reduce the failure rate of the partition function for 2D spin glass, we plot the failure rate P_f as a function of the data type's precision B. Figure 7.2 shows that the failure rate goes down as the data precision increases. These results are strong evidence that negative partition function values are caused by the limited precision of the data type.

The success of TRG for ferromagnetic Ising models implies that there is an intrinsic difference between the Ising model and spin glass. To probe this difference, we carried out two steps of coarse graining for 2D spin glass and for the Ising model

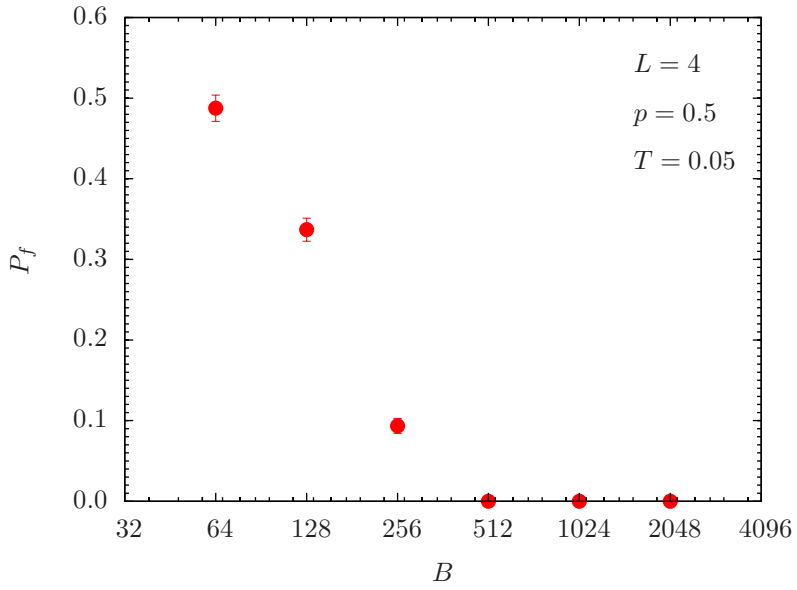

Figure 7.2: Failure rate P_f of the partition function for 2D Edwards-Anderson spin glass as a function of the number of bits B. 960 samples with $L = 4$ and $p = 0.5$ at $T = 0.05$ were generated to calculate the failure rate and error bars.

with $L = 4$, and then plotted 256 tensor components of the contracted tensor $T^{(n+1)}$. Figure 7.3 shows that for spin glass, near-cancellation of the positive and negative tensor components of the partition function requires a higher-precision data type in order to obtain the difference of the tensor components with useful accuracy. In contrast, for the Ising model, all components are positive, so double precision is good enough to obtain accurate results.

7.3.2 HOTRG

We applied HOTRG to 2D EA spin glass and computed the failure rate of the partition function as function of the cut-off parameter and data precision for different system sizes. Figure 7.4 shows that the failure rate P_f goes up as the system size L increases, which is not surprising since the precision and truncation errors add up. With a fixed system size and data precision, the failure rate goes down as the

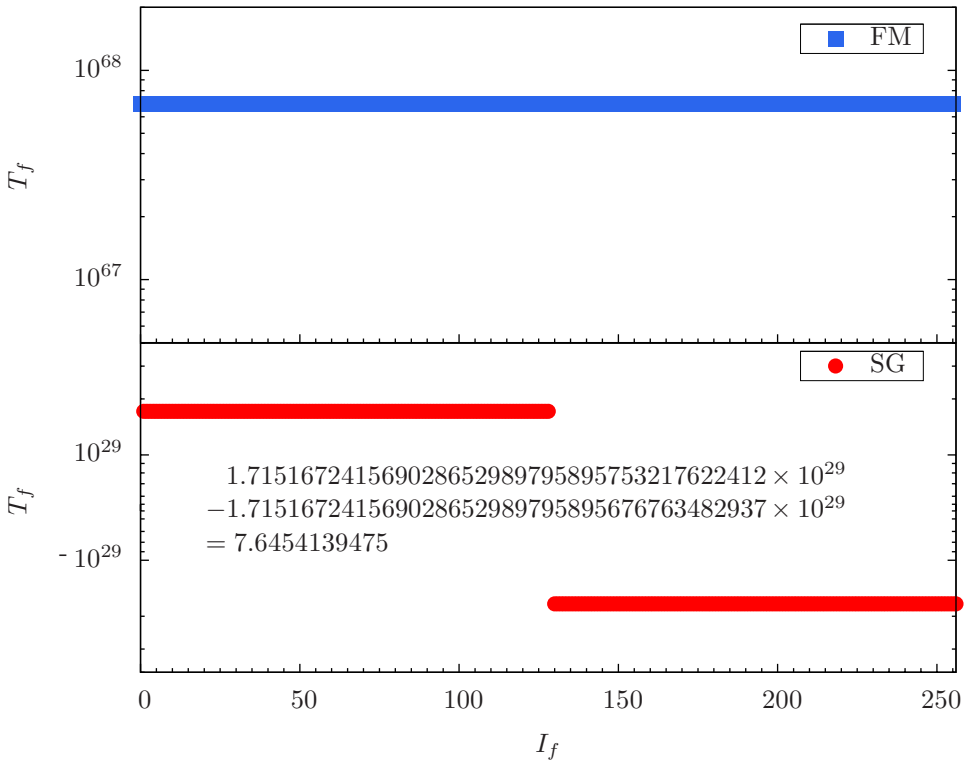

Figure 7.3: Example plot for 256 tensor components of 2D Edwards-Anderson spin glass with $p = 0.5$, $L = 4$, and $T = 0.05$ and components of the ferromagnetic Ising model with $L = 4$ and $T = 0.05$. T_f is the tensor element value and I_f is the tensor element index of the final contracted tensor.

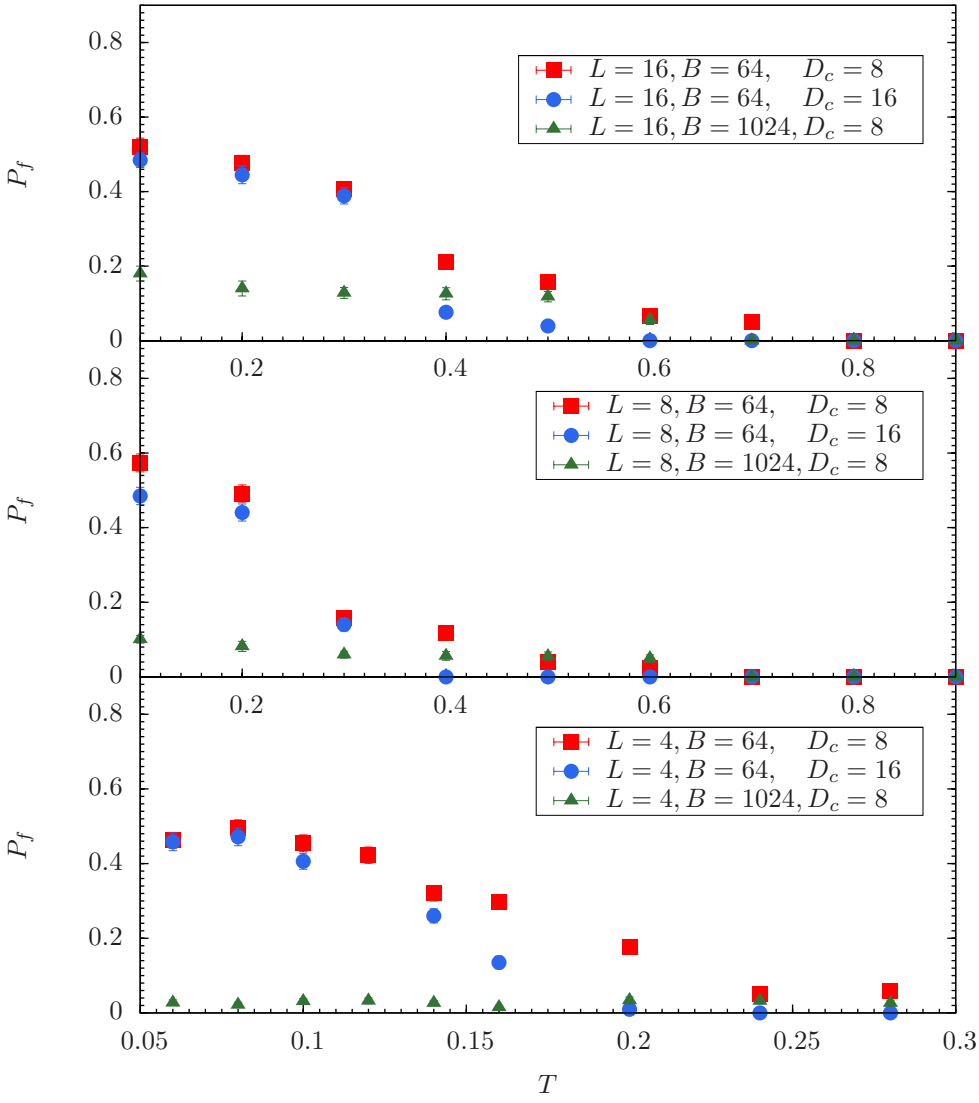

Figure 7.4: Failure rate P_f of the partition function for 2D Edwards-Anderson spin glass with HOTRG as a function of the temperature T and number of bits B. 480 samples with $L = 4, 8, 16$ and $p = 0.5$ were generated to calculate the failure rate and error bars.

cut-off parameter D_c is increased, but the result doesn't get much better at low temperatures. However, with greater data precision (going from 64 bits to 1024 bits), the failure rate drops sharply, which again demonstrates the importance of data precision for the low-temperature numerical simulation of spin glass.

7.4 Conclusions

By studying the partition function for the two-dimensional EA Ising spin-glass model on a square lattice using the tensor renormalization group method (TRG), we demonstrated that the limited precision of the data type rather than a small cut-off parameter is the primary reason for the negative partition function values for spin glass at low temperatures. In order to obtain accurate partition function values at very low temperatures, both a high-precision data type and a large cut-off parameter are required, thus illustrating that TRG can not be applied to frustrated magnetic systems.

8. SUMMARY AND OUTLOOK

In chapter 3 I show that for $\lambda > 3$, spin glasses on scale-free graphs in thermal equilibrium do order at finite temperatures in a field. These results again illustrate that Boolean decision problems on scale-free networks are superbly robust to global perturbations. It will be interesting to perform these simulations for real networks in the future, as well as the study of q-state Potts variables [182]. At zero temperature, when driven with an external field, Boolean decision problems on scale-free networks show self-organized critical behavior only when the number of neighbors diverges with the system size, i.e., for $\lambda \leq 2$. These results show that "damage" can easily spread on real networks, where typically $\lambda \leq 3$. Boolean decision problems on scale-free networks show a potential fragility when driven in non-equilibrium scenarios at zero temperature. However, no unifying mathematical formalism has been elaborated so far and it appears unclear how to identify whether a given spin system displays SOC behavior [183]. Upcoming research will analyze general characteristics or sufficient conditions that guarantee a system will display SOC.

In order to develop hard and robust benchmark instances for a quantum annealer, in chapter 4 [184] I tested different instance classes by computing their yield and resilience. The data show that bond noise has a greater impact than field noise, while resilience decreases with a lower classical energy gap and a larger degeneracy of the first excited state. The U_1 instance class has the highest resilience but virtually zero yield, while the Sidon instance class is the least resilient to Gaussian random noise but has a large fraction of unique ground states. The U_4 and $U_{5,6,7}$ instance classes have roughly the same resilience, but the $U_{5,6,7}$ instances have a much higher yield, so instance classes like $U_{5,6,7}$ with medium high resilience and yield will be

best suited for detecting quantum enhancement for the D-Wave quantum annealer. Future research will apply the bulk ϵ-perturbation developed by Palassini and Young [185] to design hard instances. For an instance, we determine an exact ground state, apply a specific perturbation to the couplings and determine a ground state of the perturbed system. Intuitively, we call a landscape complicated if the spin configurations of the unperturbed and perturbed ground states are "very" different. Otherwise the energy landscape is uncomplicated as the perturbation only slightly changes the ground state.

The phenomenon of quantum tunneling (QA) suggests a better performance of QA with respect to simulated annealing (SA) in cases of high but narrow energy barriers. Such intuitive expectation can be made quantitative using the following argument [186]: if the system tries to overcome an energy barrier of height Δ, the classical probability of escape over the barrier is of the order of $\exp(-\Delta/T)$, where T denotes the temperature of the system, while the quantum tunneling probability is of the order of $\exp(-\Delta^{1/2}w/\Gamma)$, where w denotes the width of the barrier and Γ denotes the strength of the quantum fluctuation. For N-spin glasses, $\Delta \propto N$, and with a linear annealing schedule for the transverse field, one gets $\tau \propto \exp(N^{1/2})$ for the annealing time (instead of $\tau \propto \exp(N)$ for thermal annealing). This $O(N^{1/2})$ advantage can be potentially used to detect quantum speedup for D-Wave machine. Upcoming research will apply fast Fourier transform algorithm to automatically detect peak of probability distribution of spin glass order parameter and mine a large number of instances down to a much smaller set of engineered instances with the tunable height of energy barriers. Hopefully we will be able to detect the first signs of quantum speedup by comparing performance of D-Wave Two machine and SA on these benchmark instances.

In chapter 5 and 6 I developed a rejection-free cluster algorithm for spin glasses

in any space dimension, and this greatly improves thermalization and equiprobable sampling of ground states. By restricting Houdayer cluster moves to temperatures where cluster percolation is hampered by the interplay of frustration and temperature, we were able to extend the Houdayer cluster algorithm for two-dimensional spin glasses to any topology/space dimension. Our standard implementation of the cluster updates represents only minor overhead in relation to the thermalization time speedup obtained from the isoenergetic cluster moves—a speedup that increases with the system size. The isoenergetic cluster moves can be potentially applied to Ising spin glasses with multispin interactions on two-dimensional triangular lattice (50 percent of site percolation threshold), a topology with NP-hard complexity for finding ground states [187] and an alternative topology for quantum annealer hardware. In addition, our cluster moves can be added to any algorithm such as population annealing to speed up dynamics. The future research will emphasize the applications of cluster moves in other research disciplines.

In chapter 7 I investigated the partition function of the two-dimensional Edwards-Anderson Ising spin-glass model on a square lattice by using the tensor renormalization group method based on higher-order singular value decomposition (HOTRG). We demonstrated that the limited precision of the data type rather than the small cut-off parameter is the primary reason for the negative partition function value for spin glass at low temperatures. In order to obtain an accurate partition function value at very low temperatures, both a high precision data type and a large cut-off parameter are required. This illustrates that HOTRG can not be applied to frustrated magnetic systems. The nature of negative partition function for spin glass is still unknown. However, the comparison of tensor components of 2D Edwards-Anderson spin-glass and ferromagnetic Ising model might suggest the presence of minus sign problem [188], which refers to failure of numerical methods because of

the near-cancellation of the positive and negative contributions to the integral and each contribution has to be integrated to very high precision in order for their difference to be obtained with useful accuracy. Future research will focus on identifying the underlying mechanism of the highly oscillatory tensor components of Ising spin glasses.

REFERENCES

[1] M. Mézard, G. Parisi, and R. Zecchina, "Analytic and Algorithmic Solution of Random Satisfiability Problems," *Science*, vol. 297, p. 812, 2002.

[2] H. G. Katzgraber, K. Janzen, and C. K. Thomas, "Boolean decision problems with competing interactions on scale-free networks: Critical thermodynamics," *Phys. Rev. E*, vol. 86, p. 031116, 2012.

[3] H. G. Katzgraber, F. Hamze, and R. S. Andrist, "Glassy Chimeras Could Be Blind to Quantum Speedup: Designing Better Benchmarks for Quantum Annealing Machines," *Phys. Rev. X*, vol. 4, p. 021008, 2014.

[4] M. Aizenman and D. J. Barsky, "Sharpness of the phase transition in percolation models," *Comm. Math. Phys.*, vol. 108, pp. 489–526, 1987.

[5] L. Onsager, "Crystal Statistics. I. A Two-Dimensional Model with an Order-Disorder Transition," *Phys. Rev.*, vol. 65, p. 117, 1944.

[6] G. Jaeger, "The ehrenfest classification of phase transitions: Introduction and evolution," *Archive for History of Exact Sciences*, vol. 53, pp. 51–81, 1998.

[7] E. Ising, "Beitrag zur Theorie des Ferromagnetismus," *Z. Phys.*, vol. 31, p. 253, 1925.

[8] L. D. Landau *Phys. Z. Sowjetunion*, vol. 11, p. 26, 1937.

[9] P. Weiss, "L'hypothèse du champ moléculaire et la propriété ferromagnétique," *J. Phys. Theor. Appl.*, vol. 6, no. 1, pp. 661–690, 1907.

[10] H. E. Stanley, *An Introduction to Phase Transitions and Critical Phenomena*. Oxford: Oxford University Press, 1971.

[11] M. E. Fisher, "The theory of equilibrium critical phenomena," *Reports on Progress in Physics*, vol. 30, p. 615, 1967.

[12] L. P. Kadanoff, W. Götze, D. Hamblen, R. Hecht, E. Lewis, V. V. Palciauskas, M. Rayl, J. Swift, D. Aspnes, and J. Kane, "Static phenomena near critical points: Theory and experiment," *Rev. Mod. Phys.*, vol. 39, pp. 395–431, 1967.

[13] K. G. Wilson, "Renormalization group and critical phenomena. ii. phase-space cell analysis of critical behavior," *Phys.Rev.B*, vol. 4, pp. 3184–3205, 1971.

[14] K. Binder and A. P. Young, "Spin glasses: Experimental facts, theoretical concepts and open questions," *Rev. Mod. Phys.*, vol. 58, p. 801, 1986.

[15] D. Sherrington and S. Kirkpatrick, "Solvable model of a spin glass," *Phys. Rev. Lett.*, vol. 35, p. 1792, 1975.

[16] L. Cugliandolo and J. Kurchan, "On the out-of-equilibrium relaxation of the sherrington-kirkpatrick model," *Journal of Physics A: Mathematical and General*, vol. 27, p. 5749, 1994.

[17] M. Mézard, G. Parisi, N. Sourlas, G. Toulouse, and M. Virasoro, "Nature of the Spin-Glass Phase," *Phys. Rev. Lett.*, vol. 52, pp. 1156–1159, 1984.

[18] D. Panchenko, "The parisi ultrametricity conjecture," 2011. (arXiv:1112.1003).

[19] L. Pastur and M. Shcherbina, "Absence of self-averaging of the order parameter in the sherrington-kirkpatrick model," *Journal of Statistical Physics*, vol. 62, pp. 1–19, 1991.

[20] S. F. Edwards and P. W. Anderson, "Theory of spin glasses," *J. Phys. F: Met. Phys.*, vol. 5, p. 965, 1975.

[21] S. Boettcher, "Stiffness of the Edwards-Anderson Model in all Dimensions," *Phys. Rev. Lett.*, vol. 95, p. 197205, 2005.

[22] A. B. Harris, T. C. Lubensky, and J.-H. Chen, "Critical Properties of Spin-Glasses," *Phys. Rev. Lett.*, vol. 36, p. 415, 1976.

[23] D. S. Fisher and D. A. Huse, "Ordered phase of short-range Ising spin-glasses," *Phys. Rev. Lett.*, vol. 56, p. 1601, 1986.

[24] D. A. Huse and D. S. Fisher, "Pure states in spin glasses," *J. Phys. A*, vol. 20, p. L997, 1987.

[25] D. S. Fisher and D. A. Huse, "Equilibrium behavior of the spin-glass ordered phase," *Phys. Rev. B*, vol. 38, p. 386, 1988.

[26] G. Parisi, "Infinite number of order parameters for spin-glasses," *Phys. Rev. Lett.*, vol. 43, p. 1754, 1979.

[27] G. Parisi, "The order parameter for spin glasses: a function on the interval 0–1," *J. Phys. A*, vol. 13, p. 1101, 1980.

[28] A. P. Young and H. G. Katzgraber, "Absence of an Almeida-Thouless line in Three-Dimensional Spin Glasses," *Phys. Rev. Lett.*, vol. 93, p. 207203, 2004.

[29] T. Jörg, H. G. Katzgraber, and F. Krzakala, "Behavior of Ising Spin Glasses in a Magnetic Field," *Phys. Rev. Lett.*, vol. 100, p. 197202, 2008.

[30] D. Larson, H. G. Katzgraber, M. A. Moore, and A. P. Young, "Spin glasses in a field: Three and four dimensions as seen from one space dimension," *Phys. Rev. B*, vol. 87, p. 024414, 2013.

[31] Z. Zhu, J. C. Andresen, M. A. Moore, and H. G. Katzgraber, "Boolean decision problems with competing interactions on scale-free networks: Equilibrium and nonequilibrium behavior in an external bias," *Phys. Rev. E*, vol. 89, p. 022118, 2014.

[32] D. J. Amit, H. Gutfreund, and H. Sompolinsky, "Spin-glass models of neural networks," *Phys. Rev. A*, vol. 32, pp. 1007–1018, 1985.

[33] D.-H. Kim, G. J. Rodgers, B. Kahng, and D. Kim, "Spin-glass phase transition on scale-free networks," *Phys. Rev. E*, vol. 71, p. 056115, 2005.

[34] J. D. Bryngelson and P. G. Wolynes, "Spin glasses and the statistical mechanics of protein folding," *PNAS*, vol. 84, pp. 7524–7528, 1987.

[35] F. Pázmándi, G. Zaránd, and G. T. Zimányi, "Self-organized criticality in the hysteresis of the sherrington-kirkpatrick model," *Phys. Rev. Lett.*, vol. 83, p. 1034, 1999.

[36] S. Kirkpatrick, C. D. Gelatt, Jr., and M. P. Vecchi, "Optimization by simulated annealing," *Science*, vol. 220, p. 671, 1983.

[37] S. Boixo, T. Albash, F. M. Spedalieri, N. Chancellor, and D. A. Lidar, "Experimental signature of programmable quantum annealing," *Nat. Comm.*, vol. 4, p. 2067, 2013.

[38] T. F. Rønnow, Z. Wang, J. Job, S. Boixo, S. V. Isakov, D. Wecker, J. M. Martinis, D. A. Lidar, and M. Troyer, "Defining and detecting quantum speedup," *Science*, vol. 345, no. 420, 2014.

[39] D. Challet and M. Marsili, "Phase transition and symmetry breaking in the minority game," *Phys. Rev. E*, vol. 60, pp. R6271–R6274, 1999.

[40] H. Nishimori, *Statistical Physics of Spin Glasses and Information Processing: An Introduction*. New York: Oxford University Press, 2001.

[41] A. Young, "Numerical simulations of spin glasses: Methods and some recent results," pp. 31–44, 2006.

[42] K. Hukushima and K. Nemoto, "Exchange Monte Carlo method and application to spin glass simulations," *J. Phys. Soc. Jpn.*, vol. 65, p. 1604, 1996.

[43] J. Machta, "Population annealing with weighted averages: A Monte Carlo method for rough free-energy landscapes," *Phys. Rev. E*, vol. 82, p. 026704, 2010.

[44] N. Metropolis, A. W. Rosenbluth, M. N. Rosenbluth, A. H. Teller, and E. Teller, "Equation of State Calculations by Fast Computing Machines," *J. Chem. Phys.*, vol. 21, p. 1087, 1953.

[45] H. G. Katzgraber, "Introduction to Monte Carlo Methods." (arXiv:0905.1629), 2009.

[46] N. Rathore, M. Chopra, and J. J. de Pablo, "Optimal allocation of replicas in parallel tempering simulations," *J. Chem. Phys.*, vol. 122, p. 024111, 2005.

[47] R. H. Swendsen and J.-S. Wang, "Nonuniversal critical dynamics in Monte Carlo simulations," *Phys. Rev. Lett.*, vol. 58, p. 86, 1987.

[48] U. Wolff, "Collective Monte Carlo updating for spin systems," *Phys. Rev. Lett.*, vol. 62, p. 361, 1989.

[49] T. Rizzo, "Spin glasses: statics and dynamics: summer school, paris 2007," *Progr. Probab*, vol. 62, pp. 143–157, 2009.

[50] J. Houdayer, "A cluster Monte Carlo algorithm for 2-dimensional spin glasses," *Eur. Phys. J. B.*, vol. 22, p. 479, 2001.

[51] H. G. Katzgraber, M. Palassini, and A. P. Young, "Monte Carlo simulations of spin glasses at low temperatures," *Phys. Rev. B*, vol. 63, p. 184422, 2001.

[52] K. Binder and D. Heermann, *Monte Carlo Simulation in Statistical Physics: An Introduction*. Graduate Texts in Physics, Springer-Verlag, 2010.

[53] H. G. Ballesteros, A. Cruz, L. A. Fernandez, V. Martin-Mayor, J. Pech, J. J. Ruiz-Lorenzo, A. Tarancon, P. Tellez, C. L. Ullod, and C. Ungil, "Critical behavior of the three-dimensional Ising spin glass," *Phys. Rev. B*, vol. 62, p. 14237, 2000.

[54] A. K. Hartmann and H. Rieger, *Optimization Algorithms in Physics*. Berlin: Wiley-VCH, 2001.

[55] F. Liers, M. Jünger, G. Reinelt, and G. Rinaldi in *New Optimization Algorithms in Physics* (A. K. Hartmann and H. Rieger, eds.), Berlin: Wiley-VCH, 2004.

[56] J. J. Moreno, H. G. Katzgraber, and A. K. Hartmann, "Finding low-temperature states with parallel tempering, simulated annealing and simple Monte Carlo," *Int. J. Mod. Phys. C*, vol. 14, p. 285, 2003.

[57] W. Wang, J. Machta, and H. G. Katzgraber, "Comparing Monte Carlo methods for finding ground states of Ising spin glasses: population annealing, simulated annealing and parallel tempering," 2014. (arXiv:1412.2104).

[58] K. F. Pal in *Parallel Problem Solving from Nature*, (Berlin), p. 170, Springer, 1994.

[59] A. Bautu, E. Bautu, and H. Luchian, "Particle swarm optimization hybrids for searching ground states of ising spin glasses," pp. 415–418, 2007.

[60] S. Boettcher and A. G. Percus, "Optimization with Extremal Dynamics," *Phys. Rev. Lett.*, vol. 86, p. 5211, 2001.

[61] M. Laguna and P. Laguna, "Applying tabu search to the two-dimensional ising spin glass," *International Journal of Modern Physics C*, vol. 6, pp. 11–23, 1995.

[62] S. Boettcher, "Extremal Optimization for Sherrington-Kirkpatrick Spin Glasses," *E. Phys. J. B*, vol. 46, p. 501, 2005.

[63] G. Santoro, E. Martoňák, R. Tosatti, and R. Car, "Theory of quantum annealing of an Ising spin glass," *Science*, vol. 295, p. 2427, 2002.

[64] F. Barahona, "On the computational complexity of Ising spin glass models," *J. Phys. A*, vol. 15, p. 3241, 1982.

[65] H. G. Katzgraber, "Computational physics class slides," 2015 spring. http://katzgraber.org/teaching/SS15/index.html.

[66] R. E. Ladner, "On the structure of polynomial time reducibility," *J. ACM*, vol. 22, pp. 155–171, 1975.

[67] R. Albert, H. Jeong, and A.-L. Barabási, "Internet: Diameter of the World-Wide Web," *Nature*, vol. 401, p. 130, 1999.

[68] J. M. Mooij and H. J. Kappen, "Spin-glass phase transitions on real-world graphs." (arXiv:cond-mat/0408378), 2004.

[69] A. L. Ferreira, J. F. F. Mendes, and M. Ostilli, "First- and second-order phase transitions in Ising models on small-world networks: Simulations and comparison with an effective field theory," *Phys. Rev. E*, vol. 82, p. 011141, 2010.

[70] M. Ostilli, A. L. Ferreira, and J. F. F. Mendes, "Critical behavior and correlations on scale-free small-world networks: Application to network design," *Phys. Rev. E*, vol. 83, p. 061149, 2011.

[71] J. R. L. de Almeida and D. J. Thouless, "Stability of the Sherrington-Kirkpatrick solution of a spin glass model," *J. Phys. A*, vol. 11, p. 983, 1978.

[72] C. M. Newman and D. L. Stein, "Spin-glass model with dimension-dependent ground state multiplicity," *Phys. Rev. Lett.*, vol. 72, p. 2286, 1994.

[73] M. Cieplak, A. Maritan, and J. R. Banavar, "Optimal paths and domain walls in the strong disorder limit," *Phys. Rev. Lett.*, vol. 72, p. 2320, 1994.

[74] K. Schenk, B. Drossel, and F. Schwabl, "Self-Organized Criticality in Forest-Fire Models," in *Computational Statistical Physics* (K. H. Hoffmann and M. Schreiber, eds.), p. 127, Berlin: Springer-Verlag, 2002.

[75] B. Gonçalves and S. Boettcher, "Hysteretic Optimization for Spin Glasses," *J. Stat. Mech.*, vol. P01003, 2008.

[76] J. C. Andresen, Z. Zhu, R. S. Andrist, H. G. Katzgraber, V. Dobrosavljević, and G. T. Zimanyi, "Self-Organized Criticality in Glassy Spin Systems Requires a Diverging Number of Neighbors," *Phys. Rev. Lett.*, vol. 111, p. 097203, 2013.

[77] J. P. Sethna, K. Dahmen, S. Kartha, J. A. Krumhansl, B. W. Roberts, and J. D. Shore, "Hysteresis and hierarchies: Dynamics of disorder-driven first-order phase transformations," *Phys. Rev. Lett.*, vol. 70, p. 3347, may 1993.

[78] O. Perkovic, K. A. Dahmen, and J. P. Sethna, "Avalanches, Barkhausen Noise, and Plain Old Criticality," *Phys. Rev. Lett.*, vol. 75, p. 4528, 1995.

[79] O. Perkovic, K. A. Dahmen, and J. P. Sethna, "Disorder-induced critical phenomena in hysteresis: Numerical scaling in three and higher dimensions," *Phys. Rev. B*, vol. 59, p. 6106, 1999.

[80] M. C. Kuntz, O. Perkovic, K. A. Dahmen, B. W. Roberts, and J. P. Sethna, "Hysteresis, Avalanches, and Noise: Numerical Methods." (arXiv:cond-mat/9809122v2), 1998.

[81] J. P. Sethna, K. A. Dahmen, and O. Perkovic, "Random-Field Ising Models of Hysteresis." (arXiv:cond-mat/0406320v3), 2004.

[82] E. Vives and A. Planes, "Avalanches in a fluctuationless first-order phase transition in a random-bond Ising model," *Phys. Rev. B*, vol. 50, pp. 3839–3848, 1994.

[83] E. Vives and A. Planes, "Hysteresis and avalanches in the random anisotropy Ising model," *Phys. Rev. B*, vol. 63, p. 134431, 2001.

[84] H. G. Katzgraber, D. Larson, and A. P. Young, "Study of the de Almeida-Thouless line using power-law diluted one-dimensional Ising spin glasses," *Phys. Rev. Lett.*, vol. 102, p. 177205, 2009.

[85] A. L. Barabasi and R. Albert, "Emergence of Scaling in Random Networks," *Science*, vol. 286, p. 509, 1999.

[86] Z. Burda and A. Krzywicki, "Uncorrelated random networks," *Phys. Rev. E*, vol. 67, p. 046118, 2003.

[87] M. Boguñá, R. Pastor-Satorras, and A. Vespignani, "Cut-offs and finite size effects in scale-free networks," *Eur. Phys. J. B*, vol. 38, p. 205, 2004.

[88] M. Catanzaro, M. Boguñá, and R. Pastor-Satorras, "Generation of uncorrelated random scale-free networks," *Phys. Rev. E*, vol. 71, p. 027103, 2005.

[89] H. G. Katzgraber and A. P. Young, "Probing the Almeida-Thouless line away from the mean-field model," *Phys. Rev. B*, vol. 72, p. 184416, 2005.

[90] R. A. Baños, A. Cruz, L. A. Fernandez, J. M. Gil-Narvion, A. Gordillo-Guerrero, M. Guidetti, D. Iñiguez, A. Maiorano, E. Marinari, V. Martin-Mayor, J. Monforte-Garcia, A. Muñoz Sudupe, D. Navarro, G. Parisi, S. Perez-Gaviro, J. J. Ruiz-Lorenzo, S. F. Schifano, B. Seoane, A. Tarancon, P. Tellez, R. Tripiccione, and D. Yllanes, "Thermodynamic glass transition in a spin glass without time-reversal symmetry," *Proc. Natl. Acad. Sci. U.S.A.*, vol. 109, p. 6452, 2012.

[91] M. Baity-Jesi, R. Alvarez Baños, A. Cruz, L. A. Fernandez, J. M. Gil-Narvion, Gordillo-Guerrero, D. Iñiguez, A. Maiorano, F. Mantovani, E. Marinari, V. Martin-Mayor, J. Monforte-Garcia, A. Muñoz Sudupe, D. Navarro,

G. Parisi, S. Perez-Gaviro, M. Pivanti, F. Ricci-Tersenghi, J. J. Ruiz-Lorenzo, S. F. Schifano, B. Seoane, A. Tarancon, R. Tripiccione, and D. Yllanes, "Dynamical transition in the $D = 3$ Edwards-Anderson spin glass in an external magnetic field." (arxiv:cond-mat/1307.4998), 2013.

[92] K. Binder, "Critical properties from Monte Carlo coarse graining and renormalization," *Phys. Rev. Lett.*, vol. 47, p. 693, 1981.

[93] J. C. Ciria, G. Parisi, F. Ritort, and J. J. Ruiz-Lorenzo, "The de-Almeida-Thouless line in the four-dimensional Ising spin glass," *J. Phys. I France*, vol. 3, p. 2207, 1993.

[94] C. Geyer, "Monte Carlo Maximum Likelihood for Dependent Data," in *23rd Symposium on the Interface* (E. M. Keramidas, ed.), (Fairfax Station, VA), p. 156, Interface Foundation, 1991.

[95] H. G. Katzgraber, M. Körner, and A. P. Young, "Universality in three-dimensional Ising spin glasses: A Monte Carlo study," *Phys. Rev. B*, vol. 73, p. 224432, 2006.

[96] H. G. Katzgraber, F. Pázmándi, C. R. Pike, K. Liu, R. T. Scalettar, K. L. Verosub, and G. T. Zimányi, "Reversal-field memory in the hysteresis of spin glasses," *Phys. Rev. Lett.*, vol. 89, p. 257202, 2002.

[97] Y. Imry and S.-K. Ma, "Random-Field Instability of the Ordered State of Continuous Symmetry," *Phys. Rev. Lett.*, vol. 35, p. 1399, 1975.

[98] G. Kotliar, P. W. Anderson, and D. L. Stein, "One-dimensional spin-glass model with long-range random interactions," *Phys. Rev. B*, vol. 27, p. 602, 1983.

[99] H. G. Katzgraber and A. P. Young, "Monte Carlo studies of the one-dimensional Ising spin glass with power-law interactions," *Phys. Rev. B*, vol. 67, p. 134410, 2003.

[100] L. Leuzzi, G. Parisi, F. Ricci-Tersenghi, and J. J. Ruiz-Lorenzo, "Diluted One-Dimensional Spin Glasses with Power Law Decaying Interactions," *Phys. Rev. Lett.*, vol. 101, p. 107203, 2008.

[101] M. A. Nielsen and I. L. Chuang, *Quantum Computation and Quantum Information*. Cambridge: Cambridge University Press, 2000.

[102] A. B. Finnila, M. A. Gomez, C. Sebenik, C. Stenson, and J. D. Doll, "Quantum annealing: A new method for minimizing multidimensional functions," *Chem. Phys. Lett.*, vol. 219, p. 343, 1994.

[103] T. Kadowaki and H. Nishimori, "Quantum annealing in the transverse Ising model," *Phys. Rev. E*, vol. 58, p. 5355, 1998.

[104] J. Brooke, D. Bitko, T. F. Rosenbaum, and G. Aepli, "Quantum annealing of a disordered magnet," *Science*, vol. 284, p. 779, 1999.

[105] E. Farhi, J. Goldstone, S. Gutmann, and M. Sipser, "Quantum Computation by Adiabatic Evolution." arXiv:quant-ph/0001106, 2000.

[106] J. Roland and N. J. Cerf, "Quantum search by local adiabatic evolution," *Phys. Rev. A*, vol. 65, p. 042308, 2002.

[107] A. Das and B. K. Chakrabarti, *Quantum Annealing and Related Optimization Methods*. Edited by A. Das and B.K. Chakrabarti, Lecture Notes in Physics 679, Berlin: Springer, 2005.

[108] G. E. Santoro and E. Tosatti, "TOPICAL REVIEW: Optimization using quantum mechanics: quantum annealing through adiabatic evolution," *J. Phys. A*, vol. 39, p. R393, 2006.

[109] D. A. Lidar, "Towards Fault Tolerant Adiabatic Quantum Computation," *Phys. Rev. Lett.*, vol. 100, p. 160506, 2008.

[110] A. Das and B. K. Chakrabarti, "Quantum Annealing and Analog Quantum Computation," *Rev. Mod. Phys.*, vol. 80, p. 1061, 2008.

[111] S. Morita and H. Nishimori, "Mathematical Foundation of Quantum Annealing," *J. Math. Phys.*, vol. 49, p. 125210, 2008.

[112] S. Mukherjee and B. K. Chakrabarti, "Multivariable optimization: Quantum annealing and computation," *Eur. Phys. J. Special Topics*, vol. 224, p. 17, 2015.

[113] D. R. Simon, "On the Power of Quantum Computation," *SIAM J. Comp.*, vol. 26, p. 116, 1994.

[114] M. W. Johnson, M. H. S. Amin, S. Gildert, T. Lanting, F. Hamze, N. Dickson, R. Harris, A. J. Berkley, J. Johansson, P. Bunyk, E. M. Chapple, C. Enderud, J. P. Hilton, K. Karimi, E. Ladizinsky, N. Ladizinsky, T. Oh, I. Perminov, C. Rich, M. C. Thom, E. Tolkacheva, C. J. S. Truncik, S. Uchaikin, J. Wang, B. Wilson, and G. Rose *Nature*, vol. 473, p. 194, 2011.

[115] A. Lucas, "Ising formulations of many NP problems," *Front. Physics*, vol. 12, p. 5, 2014.

[116] S. Boixo, T. F. Rønnow, S. V. Isakov, Z. Wang, D. Wecker, D. A. Lidar, J. M. Martinis, and M. Troyer, "Evidence for quantum annealing with more than one hundred qubits," *Nat. Phys,*, vol. 10, p. 218, 2014.

[117] L. Wang, T. F. Rønnow, S. Boixo, S. V. Isakov, Z. Wang, D. Wecker, D. A. Lidar, J. M. Martinis, and M. Troyer, "Comment on: "Classical signature of quantum annealing"." (arxiv:quant-phys/1305.5837), 2013.

[118] K. L. Pudenz, T. Albash, and D. A. Lidar, "Error-corrected quantum annealing with hundreds of qubits," *Nat Commun*, vol. 5, 2014.

[119] W. Vinci, T. Albash, A. Mishra, P. A. Warburton, and D. A. Lidar, "Distinguishing classical and quantum models for the D-Wave device." (arXiv:1403.4228), 2014.

[120] S. W. Shin, G. Smith, J. A. Smolin, and U. Vazirani, "How "Quantum" is the D-Wave Machine?." (arXiv:1401.7087), 2014.

[121] J. A. Smolin and G. Smith, "Classical signature of quantum annealing," *arXiv preprint arXiv:1305.4904*, 2013.

[122] G. Smith and J. Smolin, "Putting "Quantumness" to the Test," *Physics*, vol. 6, p. 105, 2013.

[123] D. Venturelli, S. Mandrà, S. Knysh, B. O'Gorman, R. Biswas, and V. Smelyanskiy, "Quantum Optimization of Fully-Connected Spin Glasses." (arXiv:cond-mat/1406.7553), 2014.

[124] T. Albash, T. F. Rønnow, M. Troyer, and D. A. Lidar, "Reexamining classical and quantum models for the D-Wave One processor." (arXiv:1409.3827), 2014.

[125] P. Bunyk, "Architectural Considerations in the Design of a Superconducting Quantum Annealing Processor," *IEEE Transactions on Applied Superconductivity*, vol. 24, p. 1, 2014.

[126] H. G. Katzgraber, F. Hamze, Z. Zhu, and A. J. Ochoa, "Seeking Quantum Speedup Through Spin Glasses: The Good, the Bad, and the Ugly." (arXiv:1505.01545), 2015.

[127] R. D. Somma, D. Nagaj, and M. Kieferová, "Quantum Speedup by Quantum Annealing," *Phys. Rev. Lett.*, vol. 109, p. 050501, 2012.

[128] I. Hen, J. Job, T. Albash, T. F. Rønnow, M. Troyer, and D. Lidar, "Probing for quantum speedup in spin glass problems with planted solutions." (arXiv:quant-phys/1502.01663), 2015.

[129] N. G. Dickson, M. W. Johnson, M. H. Amin, R. Harris, F. Altomare, A. J. Berkley, P. Bunyk, J. Cai, E. M. Chapple, P. Chavez, F. Cioata, T. Cirip, P. Debuen, M. Drew-Brook, C. Enderud, S. Gildert, F. Hamze, J. P. Hilton, E. Hoskinson, K. Karimi, E. Ladizinsky, N. Ladizinsky, T. Lanting, T. Mahon, R. Neufeld, T. Oh, I. Perminov, C. Petroff, A. Przybysz, C. Rich, P. Spear, A. Tcaciuc, M. C. Thom, E. Tolkacheva, S. Uchaikin, J. Wang, A. B. Wilson, Z. Merali, and G. Rose, "Thermally assisted quantum annealing of a 16-qubit problem," *Nat. Comm.*, vol. 4, p. 1903, 2013.

[130] T. Lanting, A. J. Przybysz, A. Y. Smirnov, F. M. Spedalieri, M. H. Amin, A. J. Berkley, R. Harris, F. Altomare, S. Boixo, P. Bunyk, N. Dickson, C. Enderud, J. P. Hilton, E. Hoskinson, M. W. Johnson, E. Ladizinsky, N. Ladizinsky, R. Neufeld, T. Oh, I. Perminov, C. Rich, M. C. Thom, E. Tolkacheva, S. Uchaikin, A. B. Wilson, and G. Rose, "Entanglement in a quantum annealing processor," *Phys. Rev. X*, vol. 4, p. 021041, 2014.

[131] K. L. Pudenz, T. Albash, and D. A. Lidar, "Quantum annealing correction for random Ising problems." arXiv:quant-phys/1408.4382, 2014.

[132] R. R. Correll, "An Efficient User-Side Nulling Calibration for Quantum Annealing Computers." (arXiv:1503.00700), 2015.

[133] S. R. McKay, A. N. Berker, and S. Kirkpatrick, "Spin-Glass Behavior in Frustrated Ising Models with Chaotic Renormalization-Group Trajectories," *Phys. Rev. Lett.*, vol. 48, p. 767, 1982.

[134] A. J. Bray and M. A. Moore, "Chaotic Nature of the Spin-Glass Phase," *Phys. Rev. Lett.*, vol. 58, p. 57, 1987.

[135] I. Kondor, "On chaos in spin glasses," *J. Phys. A*, vol. 22, p. L163, 1989.

[136] F. Ritort, "Static chaos and scaling behavior in the spin-glass phase," *Phys. Rev. B*, vol. 50, p. 6844, 1994.

[137] M. Ney-Nifle and A. P. Young, "Chaos in a two-dimensional Ising spin glass," *J. Phys. A*, vol. 30, p. 5311, 1997.

[138] M. Ney-Nifle, "Chaos and universality in a four-dimensional spin glass," *Phys. Rev. B*, vol. 57, p. 492, 1998.

[139] A. Billoire and E. Marinari, "Evidence against temperature chaos in mean-field and realistic spin glasses," *J. Phys. A*, vol. 33, p. L265, 2000.

[140] A. Billoire and E. Marinari, "Overlap among states at different temperatures in the SK model," *Europhys. Lett.*, vol. 60, p. 775, 2002.

[141] M. Sasaki, K. Hukushima, H. Yoshino, and H. Takayama, "Temperature Chaos and Bond Chaos in Edwards-Anderson Ising Spin Glasses: Domain-Wall Free-Energy Measurements," *Phys. Rev. Lett.*, vol. 95, p. 267203, 2005.

[142] H. G. Katzgraber and Krzakala, F., "Temperature and Disorder Chaos in Three-Dimensional Ising Spin Glasses," *Phys. Rev. Lett.*, vol. 98, p. 017201, 2007.

[143] D. L. Stein and C. M. Newman, *Spin Glasses and Complexity*. Primers in Complex Systems, Princeton University Press, 2013.

[144] B. Yucesoy, J. Machta, and H. G. Katzgraber, "Correlations between the dynamics of parallel tempering and the free-energy landscape in spin glasses," *Phys. Rev. E*, vol. 87, p. 012104, 2013.

[145] We chose $i_{\max} = 28$ empirically because it allowed us to encode very hard problems within many unique ground states.

[146] S. Sidon, "Ein Satz über trigonometrische Polynome und seine Anwendung in der Theorie der Fourier-Reihen," *Mathematische Annalen*, vol. 106, p. 536, 1932.

[147] Z. Zhu, A. J. Ochoa, and H. G. Katzgraber, "Efficient Cluster Algorithm for Spin Glasses in Any Space Dimension," *Phys. Rev. Lett*, 2015.

[148] One update corresponds to one Monte Carlo lattice sweep (N attempted spin updates), followed by one isoenergetic cluster move (for $T \lesssim 1$) and a parallel tempering update.

[149] Error bars are computed using a bootstrap analysis.

[150] A. Perdomo-Ortiz, B. O'Gorman, J. Fluegemann, R. Biswas, and V. N. Smelyanskiy, "Determination and correction of persistent biases in quantum annealers." (arXiv:quant-phys/1503.05679), 2015.

[151] P. Hohenberg and B. Halperin, "Theory of dynamic critical phenomena," *Rev. Mod. Phys.*, vol. 49, p. 435, 1977.

[152] L. Chayes, J. Machta, and O. Redner, "Graphical Representations for Ising Systems in External Fields," *J. Stat. Phys.*, vol. 93, p. 17, 1998.

[153] J. Machta, C. M. Newman, and D. L. Stein, "The Percolation Signature of the Spin Glass Transition," *J. Stat. Phys.*, vol. 130, p. 113, 2008.

[154] T. Jörg, "Cluster Monte Carlo algorithms for diluted spin glasses," *Prog. Theor. Phys. Suppl.*, vol. 157, p. 349, 2005.

[155] R. H. Swendsen and J.-S. Wang, "Replica Monte Carlo simulation of spin-glasses," *Phys. Rev. Lett.*, vol. 57, p. 2607, 1986.

[156] X. Feng, Y. Deng, and H. W. J. Blöte, "Percolation transitions in two dimensions," *Phys. Rev. E*, vol. 78, p. 031136, 2005.

[157] O. Melchert, "Percolation thresholds on planar Euclidean relative-neighborhood graphs," *Phys. Rev. E*, vol. 87, p. 042106, 2013.

[158] J. Wang, Z. Zhou, W. Zheng, T. Garoni, and Y. Deng, "Bond and site percolation in three dimensions," *Phys. Rev. E*, vol. 87, p. 052107, 2013.

[159] Jon Machta tells us the method might also work for ferromagnetic systems at low temperatures. Here, the step of flipping the whole spin configuration of one replica if the two replicas are in opposite pure states is crucial. In this case both replicas will be in the same pure state (all spins up or all spins down) and the clusters will be small in a ferromagnet as well.

[160] Skilled programmers will likely reduce the overhead by using more efficient programming techniques.

[161] Note that for the three-dimensional case, one may be tempted to think that clusters do not percolate because the spins are "frozen" below the critical temperature $T_c \sim 1$. However, this is not the case. In four space dimensions $T_c \sim 1.8$ [189] and $p_c = 0.197$ [190]. However, clusters still only stop percolating for $T \lesssim 1$.

[162] We note that our ICMs also slightly reduce autocorrelation times in addition to greatly improving thermalization times. However, note that the error due to configurational averages dominates in spin-glass simulations.

[163] F. Liers, M. Palassini, A. K. Hartmann, and M. Jünger, "Ground state of the Bethe lattice spin glass and running time of an exact optimization algorithm," *Phys. Rev. B*, vol. 68, p. 094406, 2003.

[164] P. Sutton, D.L. Hunter, and N. Jan, "The ground state energy of the $\pm j$ spin glass from the genetic algorithm," *J. Phys. I France*, vol. 4, pp. 1281–1285, 1994.

[165] F. Romá, S. Risau-Gusman, A. Ramirez-Pastor, F. Nieto, and E. Vogel, "The ground state energy of the edwards–anderson spin glass model with a parallel tempering monte carlo algorithm," *Physica A: Statistical Mechanics and its Applications*, vol. 388, pp. 2821–2838, 2009.

[166] Y. Matsuda, H. Nishimori, and H. G. Katzgraber, "Ground-state statistics from annealing algorithms: quantum versus classical approaches," *New J. Phys.*, vol. 11, p. 073021, 2009.

[167] H. Niggemann and J. Zittartz, "Optimum ground states for spin-3/2 chains," *Zeitschrift fr Physik B Condensed Matter*, vol. 101, pp. 289–297, 1996.

[168] M. Levin and C. P. Nave, "Tensor renormalization group approach to two-dimensional classical lattice models," *Phys. Rev. Lett.*, vol. 99, p. 120601, 2007.

[169] H. C. Jiang, Z. Y. Weng, and T. Xiang, "Accurate determination of tensor network state of quantum lattice models in two dimensions," *Phys. Rev. Lett.*, vol. 101, p. 090603, 2008.

[170] Z.-C. Gu, M. Levin, and X.-G. Wen, "Tensor-entanglement renormalization group approach as a unified method for symmetry breaking and topological phase transitions," *Phys. Rev. B*, vol. 78, p. 205116, 2008.

[171] M. Fannes, B. Nachtergaele, and R. Werner, "Finitely correlated states on quantum spin chains," *Communications in Mathematical Physics*, vol. 144, pp. 443–490, 1992.

[172] S. Östlund and S. Rommer, "Thermodynamic limit of density matrix renormalization," *Phys. Rev. Lett.*, vol. 75, pp. 3537–3540, 1995.

[173] S. R. White, "Density matrix formulation for quantum renormalization groups," *Phys. Rev. Lett.*, vol. 69, pp. 2863–2866, 1992.

[174] H. H. Zhao, Z. Y. Xie, Q. N. Chen, Z. C. Wei, J. W. Cai, and T. Xiang, "Renormalization of tensor-network states," *Phys. Rev. B*, vol. 81, p. 174411, 2010.

[175] Z. Y. Xie, J. Chen, M. P. Qin, J. W. Zhu, L. P. Yang, and T. Xiang, "Coarse-graining renormalization by higher-order singular value decomposition," *Phys. Rev. B*, vol. 86, p. 045139, 2012.

[176] L. D. Lathauwer, B. D. Moor, and J. Vandewalle, "A multilinear singular value decomposition," *SIAM Journal on Matrix Analysis and Applications*, vol. 21, pp. 1253–1278, 2000.

[177] C. Wang, S.-M. Qin, and H.-J. Zhou *Phys. Rev. B*, vol. 90, p. 174201, 2014.

[178] M. A. Moore, "The stability of the replica-symmetric state in finite-dimensional spin glasses," *J. Phys. A*, vol. 38, p. L783, 2005.

[179] H. G. Katzgraber, "Spin glasses and algorithm benchmarks: A one-dimensional view," *J. Phys.: Conf. Ser.*, vol. 95, p. 012004, 2008.

[180] M. Sasaki, K. Hukushima, H. Yoshino, and H. Takayama, "Absence of spin glass phase in the Edwards Anderson Ising spin glass in magnetic field," *J. Magn. Magn. Mater.*, vol. 310, p. 1514, 2007.

[181] T. G. et al., "GNU multiple precision arithmetic library 6.0.0," 2015. https://gmplib.org.

[182] J. M. Yeomans, *Statistical Mechanics of Phase Transitions*. Oxford: Oxford University Press, 1992.

[183] D. L. Turcotte, "Self-organized criticality," *Reports on Progress in Physics*, vol. 62, p. 1377, 1999.

[184] Z. Zhu, A. J. Ochoa, F. Hamze, S. Schnabel, and H. G. Katzgraber, "Best-case performance of quantum annealers on native spin-glass benchmarks: How chaos can affect success probabilities." arXiv:1505.02278, 2015.

[185] M. Palassini and A. P. Young, "Nature of the spin glass state," *Phys. Rev. Lett.*, vol. 85, p. 3017, 2000.

[186] S. Mukherjee and B. K. Chakrabarti, "Multivariable optimization: Quantum annealing & computation," 2014. (arXiv:1408.3262).

[187] C. K. Thomas and H. G. Katzgraber, "Optimizing glassy p-spin models," *Phys. Rev. E*, vol. 83, p. 046709, 2011.

[188] M. Troyer and U. Wiese, "Computational Complexity and Fundamental Limitations to Fermionic Quantum Monte Carlo Simulations," *Phys. Rev. Lett.*, vol. 94, p. 170201, 2005.

[189] T. Jörg and H. G. Katzgraber, "Universality and universal finite-size scaling functions in four-dimensional Ising spin glasses," *Phys. Rev. B*, vol. 77, p. 214426, 2008.

[190] G. Paul, R. Ziff, and H. Stanley, "Percolation threshold, Fisher exponent, and shortest path exponent for four and five dimensions," *Phys. Rev. E*, vol. 64, p. 026115, 2001.

[191] A. Sharma and A. P. Young, "de Almeida-Thouless line in vector spin glasses," *Phys. Rev. E*, vol. 81, p. 061115, 2010.

APPENDIX A

ANALYTICAL FORM OF THE DE ALMEIDA-THOULESS FOR $H_R \to 0$

In this appendix [31] we derive analytically the form of the AT line in the limit when $H_r \to 0$ for a type of scale-free network which is very convenient for analytical calculations, namely the static model used by Kim *et al.* [33], whose procedures and equations we shall closely follow. In this model the number of vertices N is fixed. Each vertex i ($i = 1, 2, \ldots, N$) is given a weight p_i, where

$$p_i = \frac{i^{-\mu}}{\zeta_N(\mu)}. \tag{A.1}$$

where μ is related to λ via $\lambda = 1 + 1/\mu$, and

$$\zeta_N(\mu) \equiv \sum_{j=1}^{N} j^{-\mu} \approx \frac{N^{1-\mu}}{1-\mu}. \tag{A.2}$$

Only μ in the range $[0, 1)$ (i.e., $\lambda > 2$) will be discussed. Two vertices i and j are selected with probabilities p_i and p_j and if $i \neq j$ they are connected with a single bond unless the pair are already connected. The process is repeated $NK/2$ times. Then in such a network, the probability that a given pair of vertices is not connected by an edge is $1 - f_{ij} = (1 - 2p_ip_j)^{NK/2} \approx \exp(-NKp_ip_j)$, and the probability that they are connected by an edge is $f_{ij} = NKp_ip_j$. This product form for f_{ij} enabled Kim *et al.* [33] to proceed analytically. Note that here K is the mean degree of the scale-free network generated by this procedure.

We shall work in the paramagnetic phase where the spin glass is replica symmet-

ric, i.e., where

$$q_{ab} = \sum_i p_i \langle s_i^a s_i^b \rangle = q, \tag{A.3}$$

independently of the replica labels $a = 1, 2, \ldots, n$, where n is set to zero at the end of the calculation. In q_{ab}, $a \neq b$, Kim *et al.* [33] showed then that the higher order parameters such as $q_{abcd} = \sum_i p_i \langle s_i^a s_i^b s_i^c s_i^d \rangle$ can be neglected when q is sufficiently small—that is, in the region near T_c studied in this appendix—and that a "truncation" approximation can be made for q

$$q = \int \mathcal{D}z \sum_{i=1}^{N} p_i \tanh^2 \left(z\sqrt{NK\mathbf{T}_2 p_i q + H_r^2/T^2} \right), \tag{A.4}$$

where

$$\int \mathcal{D}z \equiv \frac{1}{\sqrt{2\pi}} \int_{-\infty}^{\infty} dz e^{-z^2/2} \tag{A.5}$$

and

$$\mathbf{T}_2 = \langle \tanh^2(J_{ij}/T) \rangle. \tag{A.6}$$

Here the average is over the distribution of bonds, assumed symmetric, i.e., $P(J_{ij}) = P(-J_{ij})$. The random field of variance H_r^2 was not included in the Kim *et al.* [33] paper, but Eq. (A.4) is consistent with the equations for a spin glass in a random field studied in Ref. [191] (in the appropriate limit).

In the H_r–T phase diagram it is expected that the assumption of replica symmetry holds until the AT line is crossed. The equation of the line where the spin-glass susceptibility diverges follows from the expressions given in Ref. [33]:

$$(K\mathbf{T}_2)^{-1} = \int \mathcal{D}z \sum_{i=1}^{N} N p_i^2 \mathrm{sech}^4 \left(z\sqrt{NK\mathbf{T}_2 p_i q + H_r^2/T^2} \right). \tag{A.7}$$

The solution of Eqs. (A.4) and (A.7) together fix the equation of the AT line.

It is convenient to convert the sums over i to integrals. Let $x = i/N$. Then $\sum_{i=1}^{N} \to \int_0^1 N dx$, and in the large-$N$ limit Eq. (A.4) becomes

$$q = \int \mathcal{D}z \int_0^1 dx \frac{1-\mu}{x^\mu} \tanh^2 \left(z\sqrt{Q'/x^\mu + H_r^2/T^2} \right), \tag{A.8}$$

where $Q' = (1-\mu)K\mathbf{T}_2 q$. Equation (A.7) becomes on converting the sum to an integral

$$(K\mathbf{T}_2)^{-1} = \int \mathcal{D}z \int_0^1 dx \frac{(1-\mu)^2}{x^{2\mu}} \mathrm{sech}^4 \left(z\sqrt{Q'/x^\mu + H_r^2/T^2} \right). \tag{A.9}$$

We shall only study explicitly here the case where $3 < \lambda < 4$ ($1/3 < \mu < 1/2$). Similar procedures can be used to determine the AT line when $\lambda > 4$. We first rewrite Eq. (A.8) as

$$\begin{aligned} q &= \int \mathcal{D}z \int_0^1 dx \frac{1-\mu}{x^\mu} \Big\{ z^2 (Q'/x^\mu + H_r^2/T^2). \\ &\quad + \Big[\tanh^2 (z\sqrt{Q'/x^\mu + H_r^2/T^2}) - z^2 (Q'/x^\mu + H_r^2/T^2) \Big] \Big\}. \end{aligned} \tag{A.10}$$

The integral over z involving just the first line of Eq. (A.10) can be done to yield

$$q = (K/K_p)\mathbf{T}_2 q + H_r^2/T^2 + R(H_r, q), \tag{A.11}$$

where

$$K_p = \frac{1-2\mu}{(1-\mu)^2}, \tag{A.12}$$

and

$$R(H_r,q) = \int \mathcal{D}z \int_0^1 dx \frac{1-\mu}{x^\mu} \Big[\tanh^2\big(z\sqrt{Q'/x^\mu + H_r^2/T^2}\big) - z^2\big(Q'/x^\mu + H_r^2/T^2\big)\Big]. \quad \text{(A.13)}$$

One can show that $R(H_r,q) = R(0,q) + \mathcal{O}(Q'H_r^2/T^2)$. For small q, the term in addition to $R(0,q)$ is negligible in comparison to the term H_r^2/T^2 in Eq. (A.11) and can be dropped. We next re-write the integral for $R(0,q)$ as

$$R(0,q) = \int \mathcal{D}z \left(\int_0^\infty dx - \int_1^\infty dx \right) \frac{1-\mu}{x^\mu} \big[\tanh^2(z\sqrt{Q'/x^\mu}) - z^2 Q'/x^\mu \big]. \quad \text{(A.14)}$$

The integral from 1 to ∞ can be evaluated for small Q' by expanding the tanh in a power series in Q'. The integrals converge for $\lambda < 4$ and the leading contribution is

$$2{Q'}^2(1-\mu)\frac{\lambda-1}{4-\lambda} + \mathcal{O}({Q'}^3).$$

The integral from 0 to ∞ can by evaluated after a variable change $w = z\sqrt{Q'/x^\mu}$ when it gives a contribution $F(\lambda){Q'}^{\lambda-2}$, where

$$F(\lambda) = P(\lambda) \int_0^\infty dw\, w^{3-2\lambda} [\tanh^2 w - w^2]. \quad \text{(A.15)}$$

Here $P(\lambda) = (1-\mu)\Gamma(\lambda - 3/2)2^{\lambda-1}(\lambda-1)/\sqrt{\pi}$. Thus, for $3 < \lambda < 4$, the equation of state is

$$H_r^2/T^2 = q[1 - K\mathbf{T}_2/K_p] - F(\lambda){Q'}^{\lambda-2} - 2{Q'}^2(1-\mu)\frac{\lambda-1}{4-\lambda} + \mathcal{O}({Q'}^3), \quad \text{(A.16)}$$

which agrees with the expression given in Ref. [33] when $H_r = 0$.

When $4 < \lambda < 5$, one can proceed in a similar fashion. The equation of state is unchanged except $F(\lambda)$ becomes $\tilde{F}(\lambda)$ where

$$\tilde{F}(\lambda) = P(\lambda) \int_0^\infty dw\, w^{3-2\lambda} [\tanh^2 w - w^2 + 2w^4/3]. \tag{A.17}$$

For $\lambda > 5$ the term in ${Q'}^{\lambda-2}$ is subdominant to the term of order ${Q'}^3$ and can be ignored to leading order.

We next deduce some simple features which follow from the equations of state. In the high-temperature state $q \sim H_r^2/T^2$, and in the limit of $H_r/T \to 0$,

$$\chi_{SG} \to \frac{q}{(H_r^2/T^2)} = \frac{1}{1 - K\mathbf{T}_2/K_p}. \tag{A.18}$$

The zero-field spin-glass susceptibility χ diverges at the zero-field transition temperature T_c where $\mathbf{T}_2 = K_p/K$, and at lower temperatures q becomes nonzero. The divergence of this susceptibility as the transition is approached is of the same form for all $\lambda > 3$. This means for the critical exponent

$$\gamma = 1 \qquad\qquad (\lambda > 3) \tag{A.19}$$

However, the exponent β in $q \sim (1 - T/T_c)^\beta$ depends on λ. We obtain

$$\beta = \frac{1}{\lambda - 3} \qquad (3 < \lambda < 4) \tag{A.20}$$

$$\beta = 1 \qquad (\lambda > 4). \tag{A.21}$$

We can use Eq. (A.9) in conjunction with the equations of state to determine the form of the AT line as $H_r/T \to 0$. Once again, we shall start in the region $3 < \lambda < 4$

and write the term $\mathrm{sech}^4(z\sqrt{Q'/x^\mu + H_r^2/T^2})$ as $1 + [\mathrm{sech}^4(z\sqrt{Q'/x^\mu + H_r^2/T^2}) - 1]$. The term in unity in the integral evaluates to $1/K_p$, so

$$(K\mathbf{T}_2)^{-1} = 1/K_p + S(H_r, q), \tag{A.22}$$

where

$$S(H_r, q) = \int \mathcal{D}z \int_0^1 dx \frac{(1-\mu)^2}{x^{2\mu}} \left[\mathrm{sech}^4\left(z\sqrt{Q'/x^\mu + H_r^2/T^2}\right) - 1\right]. \tag{A.23}$$

Once again, it is sufficient to evaluate $S(H_r, q)$ at $H_r = 0$; the corrections of $\mathcal{O}(H_r^2/T^2)$ are negligible compared to the terms which we retain. Next we rewrite the integral as

$$S(0, q) = \int \mathcal{D}z \left(\int_0^\infty dx - \int_1^\infty dx\right) \frac{(1-\mu)^2}{x^{2\mu}} \left[\mathrm{sech}^4\left(z\sqrt{Q'/x^\mu}\right) - 1\right]. \tag{A.24}$$

The integral from 0 to ∞ can be evaluated after making the same variable change $w = z\sqrt{Q'/x^\mu}$, when it gives the contribution $G(\lambda){Q'}^{\lambda-3}$, where

$$G(\lambda) = 2^{\lambda-2}(1-\mu)^2(\lambda-1)\Gamma(\lambda - 5/2)/\sqrt{\pi} \times \int_0^\infty dw\, w^{5-2\lambda}[\mathrm{sech}^4 w - 1].$$

The integral from 1 to ∞ can be done in a power series in Q' and the leading term of this contribution to $S(0, q)$ is

$$-2(1-\mu)^2 Q'/(1-3\mu) + \mathcal{O}({Q'}^2).$$

We can now calculate the AT line: It is simplest to combine Eqs. (A.16) and (A.22)

to eliminate the term in $(1 - K\mathbf{T_2}/K_p)$ when one finds that

$$H_{\rm AT}^2/T^2 = C(\lambda) Q'^{\lambda-2} + \mathcal{O}(Q'^3), \tag{A.25}$$

where

$$\begin{aligned} C(\lambda) &= \frac{1}{\sqrt{\pi}} 2^{\lambda-2}(\lambda-2)\Gamma(\lambda-5/2)\int_0^\infty dw\, w^{5-2\lambda}\left\{\mathrm{sech}^4 w - 1\right. \\ &\quad \left. -2(\lambda-5/2)\left[\tanh^2 w/w^2 - 1\right]\right\}. \end{aligned} \tag{A.26}$$

The integral has to be done numerically but it stays finite as $\lambda \to 4$. For example, $C(3.75) \approx 0.530$. The terms of $\mathcal{O}(Q'^2)$ cancel from Eq. (A.25). Thus, in the range $3 < \lambda < 4$, the equation of the AT line in terms of the temperature rather than Q' is just

$$H_{\rm AT}^2/T^2 \sim (1 - T/T_c)^{\frac{\lambda-2}{\lambda-3}} \qquad (3 < \lambda < 4). \tag{A.27}$$

Note that this is in agreement with the scaling form

$$H_{\rm AT}^2/T^2 \sim (1 - T/T_c)^{\beta+\gamma}, \tag{A.28}$$

on inserting the vales for $\beta = 1/(\lambda - 3)$ and $\gamma = 1$ for $3 < \lambda < 4$.

In the range $4 < \lambda < 5$, a similar expression holds for $H_{\rm AT}^2/T^2$ as in Eq. (A.25), but $C(\lambda)$ becomes $\tilde{C}(\lambda)$ where

$$\begin{aligned} \tilde{C}(\lambda) &= \frac{1}{\sqrt{\pi}} 2^{\lambda-2}(\lambda-2)\Gamma(\lambda-5/2)\int_0^\infty dw\, w^{5-2\lambda}\left\{\mathrm{sech}^4 w - 1 + 2w^2 - \right. \\ &\quad \left. 2(\lambda-5/2)\left[\tanh^2 w/w^2 - 1 + 2w^2/3\right]\right\}. \end{aligned} \tag{A.29}$$

Because in this range the exponent $Q' \sim (1 - T/T_c)$, the form of the AT line is

$$H_{\rm AT}^2/T^2 \sim (1 - T/T_c)^{\lambda-2} \qquad (4 < \lambda < 5). \tag{A.30}$$

Finally, in the range $\lambda > 5$, the term in ${Q'}^{\lambda-2}$ is subdominant compared with the term in ${Q'}^3$ and

$$H_{\rm AT}^2/T^2 \sim (1 - T/T_c)^3 \qquad (\lambda > 5), \tag{A.31}$$

which is the familiar form of the AT line in the SK model.

One can also use the static model to investigate the behavior when $\lambda < 3$. The spin-glass phase with broken replica symmetry exists in zero field up to infinite temperature, i.e., T_c is infinite when $\lambda < 3$ [33]. However, in the interval $5/2 < \lambda < 3$ the application of a large enough random field H_r can restore replica symmetry. By solving Eqs. (A.8) and (A.9) it can be shown that this happens at a field $H_{\rm AT}$, where, as before, $\beta^2 H_{\rm AT}^2 \sim {Q'}^{\lambda-2}$ where

$$H_{\rm AT} \sim T^{\frac{5-2\lambda}{3-\lambda}} \qquad (2.5 < \lambda < 3). \tag{A.32}$$

for the limit when $T \to \infty$. This phase boundary is, as usual, for the thermodynamic limit when $N \to \infty$. The behavior which would be seen in simulations at finite system size N will be complicated by an unfamiliar finite-size behavior because, for this λ range, T_c at zero field is infinite. When $\lambda < 5/2$ we believe that for all H_r and T the spin-glass phase has broken replica symmetry and so as a consequence, there will then be no AT line.